Beam diagnostic Laser-Wire and Fast Luminosity Spectrum Measurement at the International Linear Collider

Freddy Poirier

Beam Diagnostic Laser-wire and Fast Luminosity Spectrum Measurement at the International Linear Collider

by
Freddy Poirier

Department of Physics
Royal Holloway
University of London

A thesis submitted to the University of London
for the degree of Doctor of Philosophy
July, 2005

Abstract

The International Linear Collider (ILC), a high precision electron-positron machine with centre of mass energy extending up to the TeV scale, is curently being proposed and designed. With unprecedented small beam size and high intensity the ILC aims at luminosities of the order of 10^{34} cm^{-2}s^{-1}. Careful monitoring of the beam parameters that affect the luminosity will be mandatory if these ambitious goals are to be achieved.

One of the key parameters is beam emittance, the optimisation of which requires beam size monitors with micron resolution. With this aim, a non-invasive laser-wire monitor prototype was designed, installed and run at the PETRA ring. Prior to its installation, background simulations and measurements were performed to verify that they would be low enough to allow the laser-wire programme to proceed. A lead-tungstate crystal calorimeter for the laser-wire was commissioned, including a study of temperature dependance, geometrical acceptance and energy response. The first laser-wire measurements of the PETRA positron beam size were then performed. The system, calibration and results are reported here.

At the ILC, beam energy spread and beamstrahlung effects modify the luminosity spectrum. Determination of these effects is crucial in order to extract precision physics from threshold scans. In order to provide a run-time diagnostic scheme to address this, a fast luminosity spectrum measurement technique employing forward calorimetry and statistical unfolding was devised, using the Bhabha process at low angles. The scheme is described and first results are presented.

Acknowledgements

I'm grateful to the following people for their support and help with my PhD studies. I would like to thank Mike Green and Grahame Blair for their very early discussion which ended up in giving me the opportunity to work in the high energy physics group of Royal Holloway.

My most grateful thanks to Grahame Blair, my supervisor, not only for his guiding help and proof-reading of this report but also for all the valuable discussions on physics during my PhD. He has been a source of inspiration, energy and has provided precious knowledge with his exceptional expertise and insight of the field.

I would like to thank both Thorsten Kamps and Siegfried Schreiber for their help, discussions on the laser-wire and enthusiasm. I am thankful to all the people who have been involved in the detector studies: Kay Wittenburg and Norbert Meyners especially, who provided, in addition to the devices and facilities used for my studies, a lot of help.

Rolf Heuer has been very helpful and supportive for my stay at DESY and I am very grateful for this, and to Ties Behnke for all his support while I was based in the FLC group.

I would like in addition to send my acknowledgment to Glen Cowan for the discussions on statistics and the unfolding methods as well as Stewart Boogert.

I acknowledge the financial support from the DAAD for my stay at DESY, INTAS for the funding at several conferences, and the physics departement of RHUL.

Thanks to each member of the RHUL and FLC-DESY groups that unfortunately I can not cite here. I would like to send a big cheers to the 2002 hand-ball Ruislip team, winner of the British cup, and to the Norderstedt hand-ball team with whom I've played and enjoyed new aspects of this sport, and a second big cheers to the DPC group, Bob, Simon, Patrick, Ricardo and Nabil who were

pulling me out of the office and with whom I had very interesting discussion about fish.

Finally, my biggest warmth goes to my familly “Albert, Danny, Cathy et Sylvie” who over the long distance sent me their affection, sms and good food.

Egham, July 2005

This thesis is dedicated to

"Isabella e Federico"

who remain close to my heart.

Contents

Chapter 1

Introduction

The International Linear Collider (ILC) will be a TeV-scale electron-positron collider with high luminosity of the order of 10^{34} $\mathrm{cm}^{-2}\mathrm{s}^{-1}$. It will provide a tool for scientists to address many of the most compelling questions of the 21st century - questions about dark matter, extra dimensions and the fundamental nature of matter, energy, space and time.

The standard model (SM) used to described the elementary particles has several weaknesses. The ILC, due to its high precision and TeV-scale centre of mass energy, will address some of these weaknesses. In particular it will allow a profound study of the electroweak symmetry breaking mechanism and probe the characteristics of the Higgs boson, if it exists. Alternative mechanisms will also be tested to high precision. Chap. 2 describes the SM and some of the theories beyond it. The potential physics studies of the ILC are emphasised and how the Large Hadron collider (LHC) and the ILC programmes can benefit from each other is presented.

The ILC will be based on superconducting Niobium cavities as recommended by the International Technology Recommendation Panel (ITRP) in 2004. TESLA, at the time of writing, is the only full accelerator design based on this technology and thus is described in Chap. 3. The full detector is depicted in this chapter with special emphasis on forward calorimetry, which is needed for the luminosity spectrum analysis presented in Chap. 6.

At high energies, physics cross-sections in general scale as $1/(\text{energy})^2$ and so higher luminosity is required to counter this. Low emittance is essential for high luminosity and to achieve it many diagnostic systems are needed. The laser-wire, a non-invasive laser based transverse beam size monitor, is one such system and is being tested at the PETRA ring in view to using it for the ILC. It operates by focusing laser light down to a small spot size that can be scanned across the positron beam producing Compton scattered photons, detected downstream. Background processes at two locations in PETRA were measured and are presented in Chap. 4. The background level was shown to be low enough to proceed with the installation of the laser-wire system.

To collect the Compton signal, a compact, radiation hard calorimeter based on lead-tungstate crystals was built and commissioned. Beam tests were performed to characterise its temperature dependence, geometrical acceptance and energy response. After this calibration, the calorimeter was then used to measure the total energy deposit from laser-wire events. Analysis of the resulting spectra was performed to produce the first laser-wire measurements of the PETRA positron beam size, which are presented in Chap. 5.

The variable centre of mass energy of the ILC will allow energy scans over particle production thresholds and so enable the characteristics of the particles such as their mass to be accurately determined. The ability to do this is limited by the accuracy to which the shape of the luminosity spectrum can be measured. This shape is determined primarily by initial state radiation, beamstrahlung and beam energy spread parameters.

As a beam diagnostic tool, a fast luminosity spectrum technique employing forward calorimetry and statistical unfolding methods was devised, using the Bhabha process at low angle. Chap. 6 presents this technique and shows that a resolution of less than 1% level is obtained within 2 hours of machine running. The technique provides a potentialy important tool to track the luminosity spectrum as it evolves over many hours and thus open the possibility of making corrections in real time to tune the machine.

Chapter 2

An Overview of Particle Physics in the Standard Model and Beyond

2.1 Introduction

The Standard Model (SM) of elementary particle physics provides an extremely successful description of all particle physics phenomena accessible to present day accelerators. Within the SM, matter is divided into two types of elementary particles, leptons and quarks, and the interactions between the particles occurs via messengers (gauge bosons) which characterise the forces. Despite all its success, numerous puzzles are still remaining. One puzzle is the mechanism of Electroweak Symmetry Breaking (EWSB), which tackles the question of the particle masses via the Higgs Boson, another puzzle is the so-called hierarchy problem, which deals with the wide separation between the electroweak and the Planck scales. Theories, such as supersymmetry, arose which could provide, if discovered, some answers to these outstanding questions but this will require probing more profoundly the related phenomenology with high precision. A lepton linear collider whose energy is beyond the current reach of accelerators would provide the appropriate tool to unravel many of the possible extensions to the SM. In this

LEPTONS			
	Flavour	*Charge* ($\times e$)	*Mass (MeV)*
first	e	-1	$0.51099892 \pm 4\ 10^{-8}$
generation	ν_e	0	$< 0.3 \times 10^{-6}$
second	μ	-1	$105.658364 \pm 9\ 10^{-5}$
generation	ν_μ	0	< 0.19
third	τ	-1	$1777.05\ ^{+0.19}_{-0.26}$
generation	ν_τ	0	< 18.2

Table 2.1: The three generations of Leptons, their charge and mass [8].

chapter, the SM will be described briefly in order to give a broad overview of the classification it offers and possible extension to the SM will also be discussed.

2.2 The Standard Model

The Standard Model assumes that all matter particles (or fermions) are made out of two classes of structureless point-like particles, the quarks and the leptons. It could be possible that these point-like particles are actually composite and therefore not the basic irreducible building blocks we seek. However experiment has not found any underlying structure to date.

2.2.1 Quarks and Leptons

Tab.2.1 shows the three generations of leptons and some of their properties. Each generation of leptons has its own lepton number, which is conserved to a first approximation. Neutrino oscillations, recently observed [2, 3, 4], show this conservation is violated and also that neutrinos have masses.

Leptons have charge e while quarks are spin-1/2 fermions with either $+\frac{2}{3}e$ or $-\frac{1}{3}e$ electric charge. There are six flavours (or types) that exist in nature. The six flavours are named: down, up, strange, charm, bottom and top. These also fall

QUARKS			
	Flavour	*Charge ($\times e$)*	*Approximate Mass(GeV)*
first	d (down)	$-\frac{1}{3}$	0.004 to 0.008
generation	u (up)	$+\frac{2}{3}$	0.0015 to 0.004
second	s (strange)	$-\frac{1}{3}$	0.08 to 0.130
generation	c (charm)	$+\frac{2}{3}$	1.1 to 1.4
third	b (bottom)	$-\frac{1}{3}$	4.1 to 4.4
generation	t (top)	$+\frac{2}{3}$	173.8 $\pm$5.1

Table 2.2: The three generations of Quarks [8], their charge and approximate mass.

into three generations. Some of their properties are listed in Tab.2.2 [8]. This table illustrates the wide range of particle masses.

Quarks combine to form composite particles; they are unable to exist on their own with no other quarks, an effect called quark confinement [5, 6]. The particles they form fall into two classes:

- "mesons" which consist of a quark and an antiquark ($q\bar{q}\prime$)
- and "baryons" which consist of three quarks ($qq\prime q\prime\prime$).

Here q denotes a quark of any flavour and q$\prime$ and q$\prime\prime$ quarks with possibly any other flavour.

2.2.2 Interactions and Gauge Bosons

In quantum theory the gauge bosons are particles exchanged between fermions and give rise to the four forces. These are shown in Tab.2.3. The gravitational interaction is negligible in particle physics phenomena, hence attention is confined to the other three only i.e. the electromagnetic, weak and strong interactions.

INTERACTIONS AND GAUGE BOSONS			
Forces	*Mediators*	*Electric Charge* ($\times e$)	*Mass*(GeV/c^2)
electromagnetic	photon	0	0
Weak	$W^{\pm}$, Z^0	± 1, 0	$\approx 80.425 \pm 0.038$, $\approx 91.197 \pm 0.002$
strong	gluon	0	0
gravity	graviton	0	0

Table 2.3: The interactions and gauge boson properties [8].

2.2.2.1 Weak and Electromagnetic Interaction

The electromagnetic interaction is classically well understood via Maxwell's equations. It is now described quantum mechanically by the theory called quantum electrodynamics (QED).

The weak interaction is mediated by three massive gauge bosons, the W^+, W^- and the Z^0. The $W^{\pm}$ couples only to left-handed particles or right-handed anti-particles.

The weak interaction has been unified with the electromagnetic interaction into one electroweak theory, $SU(2)_L \times U(1)_Y$,[1] introduced by Glashow, Weinberg and Salam [1]. According to this theory the weak and the electromagnetic interactions have similar coupling strengths, i.e.

$$\alpha_W = \alpha / \sin^2 \theta_W \tag{2.1}$$

where $\sin^2 \theta_W$ represents the mixing between the two gauge groups with θ_W the Weinberg angle and $\alpha \approx \frac{1}{128}$ the electroweak structure constant at the Z pole.

2.2.2.2 Strong interaction

The strong interaction is responsible for the binding of quarks into hadrons. It is mediated by gluons. Whilst the quarks all possess a colour charge, so do the gluons, in contrast to the electromagnetic interaction where the photon carries

[1] L stands for left and Y is hypercharge

no electric charge.

The strong interaction does not act over large distances despite its massless gauge bosons as all particles carrying colour are confined. The theory to describe the strong interaction is called quantum chromodynamics (QCD) and is based on the gauge symmetry $SU(3)_{colour}$.

2.2.3 Higgs boson

By applying the exact symmetry $SU(2)_L \times U(1)_Y$ and unifying the weak and electromagnetic forces, no mass term appears. Elementary particles have mass and to account for it, a massive particle which couples to every other particle is introduced. This massive particle is called the Higgs boson and its coupling strength g_{Hff} to fermions is related to the fermion mass m_f as

$$g_{Hf\overline{f}} = \frac{m_f}{\upsilon} \tag{2.2}$$

where υ is the electroweak scale ($= (G_F/\sqrt{2})^{-1/2}$=246 GeV). The theoretical Higgs boson mass is $M_H^2 = 2\lambda\upsilon^2$ where λ is the self coupling strength of the Higgs. λ is not known and thus the exact value of the mass of the Higgs is not determined.

Nonetheless, a quite restrictive bound on the value of the Standard Model Higgs mass follows from hypothetical assumptions on the energy scale Λ up to which the SM can be extended before new physical phenomena may emerge. The upper bound on the Higgs is thus:

$$M_H^2 \leq \frac{4\pi^2\upsilon^2}{3\ln(\Lambda^2/\upsilon^2)} \tag{2.3}$$

In addition it is assumed that λ has a positive value which induces a minimum bound on the Higgs mass. This value depends strongly on the cut-off Λ and the top mass [12] as

$$M_H^2 > \frac{3G_F\sqrt{2}}{8\pi^2}(2M_W^4 + M_Z^4 - 4m_t^4)\ln\left(\frac{\Lambda^2}{\upsilon^2}\right) \tag{2.4}$$

The upper and lower bounds limit are shown in Fig. 2.1 [8]. Within the Standard

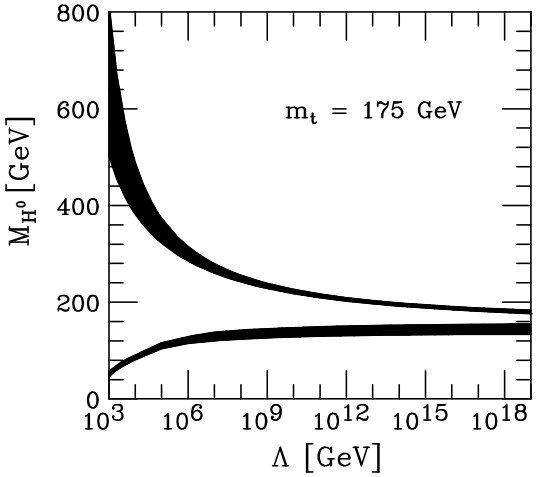

Figure 2.1: Bounds on the Higgs boson mass based on arguments of self-consistency of the SM.

Model the mass of the Higgs is less than ∼1 TeV [11]. Higgs bosons have escaped detection so far although, from combined LEP data, a lower bound of 114.4 GeV was established, at the 95% confidence level, on the mass of the standard model Higgs boson.[13]. The probing in future colliders of the properties of this elusive particle will be essential in order to decide what type of theory lies beyond the SM.

2.2.4 Weakness of the Standard Model

One of the main weaknesses of the SM is the fact that it contains a large number of parameters not determined by theory. At least 19 arbitrary parameters are contained in the SM. In addition several problems lie within this model:

- Naturalness problem: Radiative corrections to the Higgs boson mass occur in the diagrams with a fermion loop, as shown in Fig. 2.2. The most important contribution comes from heavy quarks, and particularly from the top quark. These fermion corrections are proportional to Λ^2/m_f^2 where Λ is associated with the Planck scale $m_{pl} = 10^{19}$ GeV where gravitational effects are relevant. The radiative corrections to the Higgs mass diverge quadratically with respect to Λ. In order to keep the Higgs boson mass light a counter term of the same order of Λ has to be introduced. The mass of the

Higgs would come from the difference of these two large terms, which must be as small as the order of the Higgs mass. This required "fine tuning" is said to be unnatural.

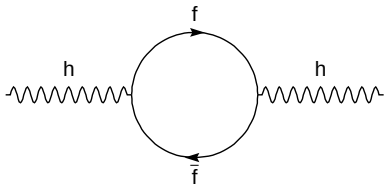

Figure 2.2: Fermion loop contributions to the Higgs boson mass.

- In addition, the SM does not provide unification of the three forces discussed earlier and the coupling constants do not converge toward the same point at high energies.
- A third problem poses the question of the unification of the SM with gravitation. Does there exist a quantum gravity theory and, if yes, can it be unified with the three other fundamental interactions? Would this theory need a space-time with more than 4 dimensions?

In the following section theories which might answer these questions are briefly described.

2.3 Beyond the Standard Model

2.3.1 Supersymmetry

Theories have been constructed in which there exist particles with exactly the same properties as the SM particles, except for different spins and these theories can solve the naturalness problem mentioned in the last section. An elegant extension to the SM which deals with this hypothesis is a theory called Supersymmetry [10]. Supersymmetry (SUSY) postulates that there is a symmetry between

SM and SUSY PARTICLES	
Standard Model particles	*Supersymmetric particles*
Quarks (spin $\frac{1}{2}$)	Squarks (spin 0)
$\begin{pmatrix} u \\ d \end{pmatrix}_L$ u_R d_R	$\begin{pmatrix} \tilde{u} \\ \tilde{d} \end{pmatrix}_L$ $\tilde{u}_R$ $\tilde{d}_R$
$\begin{pmatrix} c \\ s \end{pmatrix}_L$ c_R s_R	$\begin{pmatrix} \tilde{c} \\ \tilde{s} \end{pmatrix}_L$ $\tilde{c}_R$ $\tilde{s}_R$
$\begin{pmatrix} t \\ b \end{pmatrix}_L$ t_R b_R	$\begin{pmatrix} \tilde{t} \\ \tilde{b} \end{pmatrix}_L$ $\tilde{t}_R$ $\tilde{b}_R$ $\rightarrow \tilde{t}_{1,2}, \tilde{b}_{1,2}$
Leptons (spin $\frac{1}{2}$)	Sleptons (spin 0)
$\begin{pmatrix} e \\ \nu_e \end{pmatrix}_L$ e_R	$\begin{pmatrix} \tilde{e} \\ \tilde{\nu}_e \end{pmatrix}_L$ $\tilde{e}_R$
$\begin{pmatrix} \mu \\ \nu_\mu \end{pmatrix}_L$ μ_R	$\begin{pmatrix} \tilde{\mu} \\ \tilde{\nu}_\mu \end{pmatrix}_L$ $\tilde{\mu}_R$
$\begin{pmatrix} \tau \\ \nu_\tau \end{pmatrix}_L$ τ_R	$\begin{pmatrix} \tilde{\tau} \\ \tilde{\nu}_\tau \end{pmatrix}_L$ $\tilde{\tau}_R$ $\rightarrow \tilde{\tau}_{1,2}$
Gauge bosons (spin 1)	Gauginos (spin $\frac{1}{2}$)
g	$\tilde{g}$
γ	$\tilde{\gamma}$ $\tilde{\gamma}$,$\tilde{Z}$,$\tilde{H}^0_{1,2}$
Z	$\tilde{Z}$ $\hookrightarrow \tilde{\chi}^0_{1,2,3,4}$
$W^\pm$	$\tilde{W}^\pm$ (Neutralinos)
Higgs bosons (spin 0)	MSSM Higgs
H	h, A
	$H^\pm$
	Higgsinos (spin $\frac{1}{2}$)
	$\tilde{H}^0_{1,2}$ $\tilde{W}^+, \tilde{H}^+ \rightarrow \tilde{\chi}^+_{1,2}$
	$\tilde{H}^\pm$ $\tilde{W}^-, \tilde{H}^- \rightarrow \tilde{\chi}^-_{1,2}$ (Charginos)

Table 2.4: The fundamental particles of the Standard Model are listed on the left and their predicted supersymmetric partners on the right. The arrows indicate fields that mix and the corresponding physical fields that result. The Minimal Supersymmetric Standard Model (MSSM) requires 4 Higgs in addition to the standard model one.

bosons and fermions. This implies that every particle has a partner with exactly the same couplings but differs in spin by one half an integer as shown in Tab.2.4.

Within this theory, the diagram in Figure 2.2, where $\tilde{f}$ is the supersymmetric partner of f, is included with the diagram in Figure 2.3. These diagrams have the same vertices and coupling constants, and hence at high energy, the same magnitude for the amplitude. But since the particle spins are different, the amplitude has opposite sign. So when calculating a cross-section, the amplitudes cancel yielding a finite interaction probability.

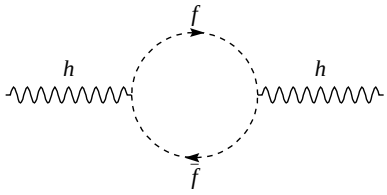

Figure 2.3: Higgs boson dissociating into a virtual sfermion-antisfermion pair; at high energy this diagram cancels the equivalent one in Figure 2.2.

Some models of SUSY retain a small Higgs mass in a natural way and it provides a base towards unification of the electroweak and strong interaction. In addition SUSY theories give a consistent prediction of the size of the electroweak mixing parameter $\sin^2\theta_w$. Furthermore SUSY, in the framework of R-parity[2] conservation, can provide a stable neutral supersymmetric particles, which can fulfil the dark matter requirements needed in astrophysics and cosmology.

2.3.2 Alternative Physics

A certain number of alternative models enclose the idea of a Higgs field and generate Electroweak Symmetry Breaking. Two important alternative scenarios to the SM are extra-dimensional theories and new types of strong interactions. These are discussed in more detail, together with other scenarios in [15] within the framework of e^+e^- colliders:

[2]R parity relates SM particles with positive R-parity to their superpartners with negative R-parity .

- Extra-dimensions at a semi-macroscopic scale. This approach addresses the gauge hierarchy problem and gives concrete and distinctive phenomenology. For example, in such scenarios resonances would appear for the cross-section $e^+e^- \to \mu^+\mu^-$ as shown in Fig. 2.4

- One can imagine that no Higgs boson exists. In that case, the electroweak symmetry should be broken by some other interactions, and gauge boson scattering should become strong at a scale of order 1 TeV. Such theories are often referred to as strongly coupled theories. Potential signatures within this model are expected to come mostly from anomalous W^+W^- coupling [19].

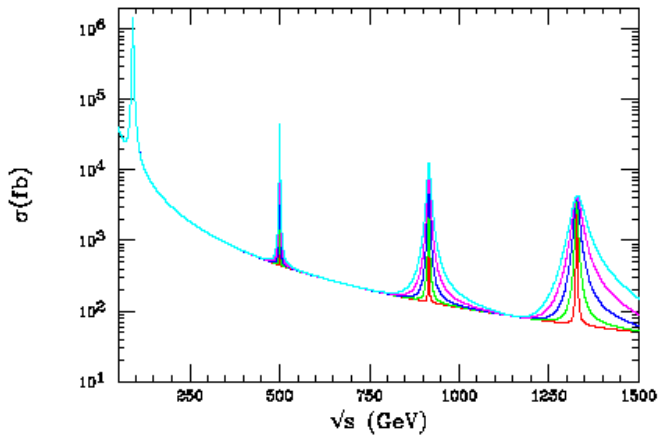

Figure 2.4: Cross-section for $e^+e^- \to \mu^+\mu^-$ as a function of $\sqrt{s}$ showing several resonances for large extra-dimension scenarios [15].

2.4 Potential Physics Studies at the International Linear Collider

The International Linear Collider (ILC), described in Chap. 3, is foreseen to reach a centre of mass energy (cms) of up to 500 GeV with an upgrade to the TeV scale. Within its energy range, several processes will switch on as shown in Fig.2.5. The ILC is referred to as a high precision machine as it is designed to provide

	now	LHC	LC
δM_W [MeV]	33	15	10
δm_t [GeV]	5.1	1.0	0.2-0.1
δm_h [MeV]	-	100	50

Table 2.5: Current and anticipated future experimental uncertainties for the W boson mass, M_W, the top quark mass, m_t. The indirect determination Higgs boson mass, m_h is also given [16].

high accuracy measurements mainly due a clean experimental environment. As an example, Tab.2.5 illustrates the current and anticipated future experimental uncertainties for the mass measurements of the W, the top and the indirect precision on the Higgs boson mass. If a Higgs boson exists within the TeV

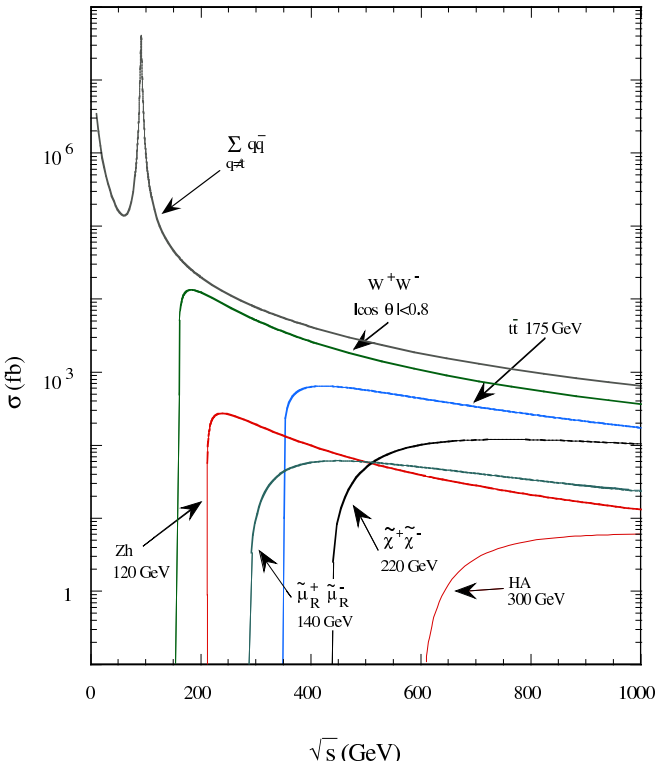

Figure 2.5: Cross-sections for some interesting processes at the ILC [22].

range, the ILC will be able to measure the full set of its properties with high precision. The observables on the Higgs, i.e. its mass, spin, and lifetime, its production cross-section, and branching ratios will decide if it has the profile of

the one predicted by the SM. Further studies to refine the existing precision can then constrain the model or reveal its origin from a supersymmetric world or other scenarios.

2.4.1 Threshold Scans

A linear collider, operating near the $t\bar{t}$ production threshold and at higher energies, can carry out a comprehensive programme of top quark physics. The cross-section for $e^+e^- \rightarrow t\bar{t}$ presents a sharp increase around the centre of mass energy of 350 GeV. The shape of its threshold production cross-section depends on its mass, its width, the strong coupling α_s and the top quark Yukawa coupling. The dependance of the cross-section on the centre of mass energy is shown in Fig.2.6. The effect of a shift of 10% of the top quark width is also shown to illustrate the variation of the cross-section as was done in [17]. This shows that a measurement of the width is most sensitive in the peak of the thresshold scan. A careful study of this $t\bar{t}$ threshold structure allows for accurate measurements of each parameter of the top quark. In addition this study contributes radically to the accuracy of Higgs predictions. Precise determination of the parameters that form the shape of the luminosity spectrum is crucial because the measured threshold scan depends strongly on it. The measurement of this luminosity spectrum forms a major part of this thesis. Fig.2.7 shows the modification of the threshold scan as several additional blurring effects are switched on.

If SUSY is realised in nature, several schemes would give rise to a rich spectrum of particles (Fig. 2.8). Because the ILC can scan its well-defined centre of mass energy across thresholds for new physics production it will be able to identify them one by one and to measure supersymmetric particle masses with very high precision. If alternative physics is the way that nature expresses itself, several processes which are present within the SM such as $e^+e^- \rightarrow \mu^+\mu^-$ will display variation compared to the SM prediction at high energy. In addition careful extrapolation beyond the ILC's energy reach will benefit the physics at very large energy scale.

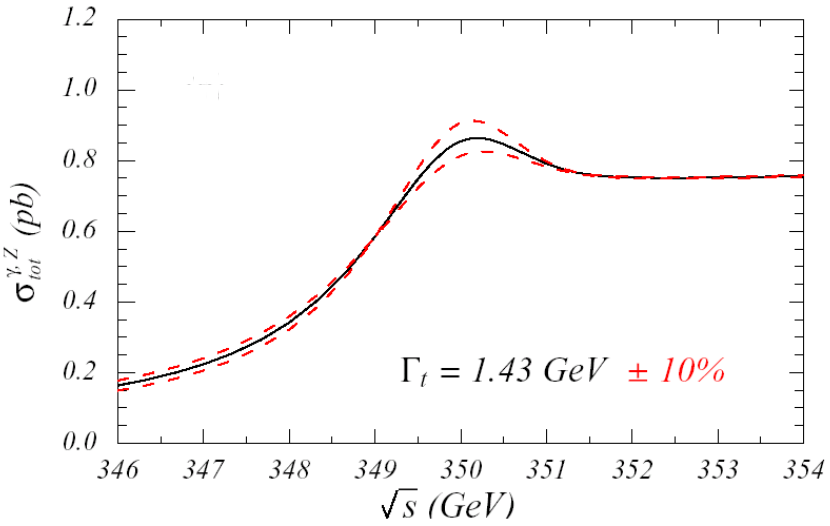

Figure 2.6: Cross-section near the threshold for a top width $\Gamma_t = 1.43$ GeV. The dotted lines corresponds to a shift of 10% of the top width [17].

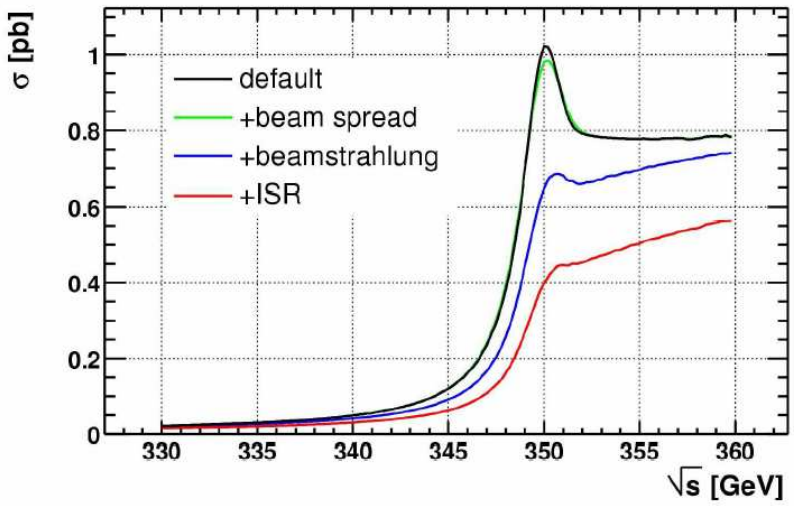

Figure 2.7: Cross-section at the top threshold including several effects such as beam energy spread, beamstrahlung and initial state radiation [18].

2.5 On the complementarity with LHC

The interplay between the Large Hadron Collider (LHC), being built at CERN and the ILC is detailed in the report in Ref. [19]. Most of the studies assume that the ILC comes into operation while the LHC is still running. During simultaneous running, analyses carried out at one machine could be adapted according to the results obtained at the other machine. The ILC results could also serve as an

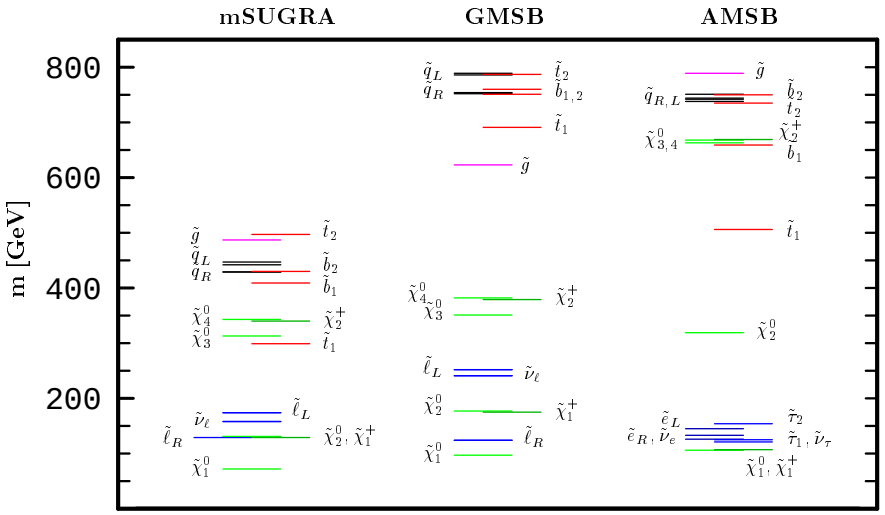

Figure 2.8: Example of mass spectrum for various SUSY model: minimal supergravity (mSUGRA), Gauge mediated symmetry breaking (GMSB) and anomaly mediated symmetry breaking (AMSB) [22].

	LHC	LHC+LC
$\delta\tilde{\chi}_1^0$ [GeV]	4.8	0.05
$\delta\tilde{\chi}_2^0$ [GeV]	4.7	0.08

Table 2.6: The neutralino RMS values of the mass distribution for LHC alone and combined with measures from the LC [19].

input for a second phase of LHC running, influencing possible upgrade options. It is foreseen that the ILC precision allows typical improvements by a factor 2 to 10 for standard model processes and a factor 2 to 3 for minimal supersymmetric standard model processes. As an example, within SUSY, the accuracy of the determination of the mass of the lightest supersymmetric particle neutralino and of the next-to-lightest one at the LHC would lead to a drastic improvement of accuracy with ILC input as shown in Tab.2.6.

Bibliography

[1] S. L. Glashow, Nucl. Phys. **22** (1961) 579. S. Weinberg, Phys. Rev. Lett. **19** (1967) 1264. A. Salam and J. C. Ward, Phys. Lett. **13** (1964) 168.

[2] B. T. Cleveland *et al.*, "Measurement of the solar electron neutrino flux with the Homestake chlorine detector," Astrophys. J. **496** (1998) 505.

[3] S. Fukuda *et al.* [Super-Kamiokande Collaboration], "Solar B-8 and he p neutrino measurements from 1258 days of Super-Kamiokande data," Phys. Rev. Lett. **86** (2001) 5651 [arXiv:hep-ex/0103032].

[4] Q. R. Ahmad *et al.* [SNO Collaboration], "Direct evidence for neutrino flavor transformation from neutral-current interactions in the Sudbury Neutrino Observatory," Phys. Rev. Lett. **89** (2002) 011301 [arXiv:nucl-ex/0204008].

[5] H. D. Politzer, "Asymptotic Freedom: An Approach To Strong Interactions," Phys. Rept. **14** (1974) 129.

[6] D. J. Gross and F. Wilczek, "Asymptotically Free Gauge Theories. 2," Phys. Rev. D **9** (1974) 980.

[7] P. W. Higgs, Phys. Lett. **12** (1964) 132. P. W. Higgs, Phys. Rev. **145** (1966) 1156. F. Englert and R. Brout, Phys. Rev. Lett. **13** (1964) 321. G. S. Guralnik, C. R. Hagen and T. W. B. Kibble, Phys. Rev. Lett. **13** (1964) 585.

[8] Particle Data Group, "Review of Particle Properties", *European Phys. J.* **C3**, 2004.

[9] S. Stepanyan *et al.* [CLAS Collaboration], Phys. Rev. Lett. **91** (2003) 252001 [arXiv:hep-ex/0307018]. J. Barth *et al.* [SAPHIR Collaboration], arXiv:hep-ex/0307083.

[10] H.E. Haber and G.L Kane, Phys. Reports **117**, 1985.

[11] M. Lindner, "Implications Of Triviality For The Standard Model," Z. Phys. Rev. **31**, 295 (1986).

[12] C. Quigg, "The Standard model (Electroweak theory)," FERMILAB-FN-0731

[13] R. Barate *et al.* [ALEPH Collaboration,DELPHI Collaboration and L3 Collaboration and OPAL Collaboration], "Search for the standard model Higgs boson at LEP," Phys. Lett. B **565** (2003) 61 [arXiv:hep-ex/0306033].

[14] J. A. Aguilar-Saavedra *et al.* [ECFA/DESY LC Physics Working Group Collaboration], "TESLA Technical Design Report Part III: Physics at an e+e- Linear Collider," arXiv:hep-ph/0106315.

[15] T. Abe *et al.* [American Linear Collider Working Group Collaboration], "Linear collider physics resource book for Snowmass 2001. 3: Studies of exotic and standard model physics," in *Proc. of the APS/DPF/DPB Summer Study on the Future of Particle Physics (Snowmass 2001)* ed. N. Graf, arXiv:hep-ex/0106057.

[16] U. Baur, R. Clare, J. Erler, S. Heinemeyer, D. Wackeroth, G. Weiglein and D. R. Wood, "Theoretical and experimental status of the indirect Higgs boson mass determination in the standard model," in *Proc. of the APS/DPF/DPB Summer Study on the Future of Particle Physics (Snowmass 2001)* ed. N. Graf, eConf **C010630** (2001) P122 [arXiv:hep-ph/0111314].

[17] A. H. Hoang, A. V. Manohar, I. W. Stewart and T. Teubner, "The threshold t anti-t cross section at NNLL order," Phys. Rev. D **65** (2002) 014014 [arXiv:hep-ph/0107144].

[18] S. Boogert, "Luminosity spectrum impact on the top mass", ECFA meeting Durham http://www.hep.ucl.ac.uk/~sboogert/content/topquark/ecfa-08-2004.pdf

[19] G. Weiglein *et al.* [LHC/LC Study Group], "Physics interplay of the LHC and the ILC," arXiv:hep-ph/0410364.

Chapter 3

The Linear Collider and the TESLA Detector

Considerable physics potential will be opened up at the ILC. New processes will emerge as the centre of mass energy increases while, concurrently, their cross-section generally decreases. High luminosity is therefore required to provide high enough statistics. In the following chapter we will discuss the machine to provide the high energy and high luminosity as well as the detector, which is used to unravel physics processes. Particular attention is given to the forward calorimetry which is used in Chap. 6 in simulations of the luminosity spectrum measurements.

3.1 The Linear Collider

In addition to achieving high luminosity, the choice of a linear collider is mainly driven by the amount of energy that can be brought together at the interaction point keeping as low as possible any losses within the collider. In a usual circular electron ring, the electrons lose some of their energy via synchrotron radiation. In such a machine, the energy loss for a particle deflected by a magnetic field is proportional to the fourth power of the beam energy and the inverse of the average ring radius. LEP (Large Electron Positron collider) was experiencing 1.5 GeV of loss per turn for a centre of mass energy of 180 GeV. As a comparison LEP

running at 500 GeV would lose approximately 90 GeV per turn and achieving a machine reaching 500 GeV with relatively low loss would require a ring with a circumference of 200 km. Therefore circular rings in this respect can not be used to attain very high energy. The solution lies in accelerating the particles in a straight line i.e. adopting a linear collider. Until recently, several projects were under study to provide such collider. Although their physics programme was similar and they all had the goals to achieve higher energy and luminosity than previous machines, the proposed technologies were different. The machine designs were denoted as:

- **NLC** - the Next Linear Collider, project driven mainly by SLAC, US;
- **TESLA** - The Tera electron volt Energy Superconducting Linear Accelerator conducted by DESY, Germany;
- **GLC** - the Global Linear Collider brought forward by KEK, Japan.

In 2004, the International Technology Recommendation Panel (ITRP), charged to make a choice of the technology for a proposed future international particle accelerator, recommended superconducting technology. Being at the time of writing the only "cold" technology particle accelerator, TESLA is discussed in more detail in the following sections. The parameters of the International Linear Collider (ILC) are being revisited and might undergo modifications such as the crossing angle and bunch spacing. In addition to the ILC, the European Centre of Nuclear Research (CERN) conducts a project called the Compact Linear Collider (CLIC) aiming a multi-TeV machine with high accelerating gradient (150 MV/m), based on normal conducting technology.

3.1.1 TESLA Accelerator

3.1.1.1 General Layout

The overall length of the TESLA linear collider is foreseen to be 33 km. It is made up of two linear accelerators, electron and positron, pointing at each other.

Each linear accelerator is constructed with ten thousand 1-m long superconducting niobium cavities (Fig. 3.1), each consisting of 9 cells and cooled by superfluid Helium to $T = 2^oK$. The technology of the machine is thus referred to as cold technology. The power dissipation in the cavity walls is small, allowing a high

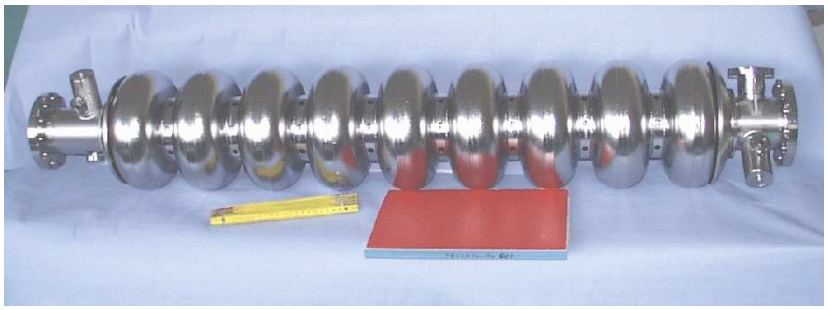

Figure 3.1: The 9-cell niobium cavity for TESLA.

beam power with low electrical power consumption. Thus, the choice of superconducting RF offers the possibility to use a long RF-pulse (1 ms). It also allows a relatively large bunch spacing (337ns at E_{cms}=500 GeV) with lower wakefield effects than with a machine with shorter bunch spacing.

3.1.1.2 Parameters

The machine parameters of TESLA are presented in Tab. 3.1. The pulse length is often referred to train length as it is consists of a series of consecutive shortly interspaced bunches and a long waiting time (approximately 199 ms for TESLA) before the next train. Within one second nearly 14100 bunch crossings occur at TESLA-500. The repetition rate (f_{rep} = 5 Hz) drives the time interval between the start of each train. The low RF-frequency (f_{RF}=1.3 GHz) is suitable for a high peak power system that converts AC-power to RF-power used to accelerate the bunches. One of the most noticeable features of the beam is its flatness as at the interaction point the beam size is designed to be $553(x) \times 5(y)$ nm for the 500 GeV centre of mass energy machine. A flat beam limits the beamstrahlung as described in Sec. 6.2.2.

		TESLA-500	**TESLA-800**
Accelerating gradient	E_{acc} [MV/m]	23.4	35
RF-frequency	f_{RF} [GHz]	1.3	
Linac Repetition rate	f_{rep} [Hz]	5	4
Total site length	L_{tot} [km]	33	33
Active length	[km]	21.8	
No. of accelerator structures		21024	
Beam pulse length	T_P [μs]	950	860
No. of bunches per pulse	n_b	2820	4886
Bunch spacing	Δt_b [ns]	337	176
Charge per bunch	N_e [10^{10}]	2	1.4
Emittance at IP	$\gamma\epsilon_{x,y}$ [$10^{-6}m$]	10, 0.03	8, 0.015
Beta at IP	$\beta^*_{x,y}$ [mm]	15, 0.4	15, 0.4
Beam size at IP	$\sigma^*_{x,y}$ [nm]	553, 5	391, 2.8
Bunch length at IP	σ_z [nm]	300	300
Beamstrahlung	δ_E [%]	3.2	4.3
Luminosity	$L_{e^+e^-}$ [$10^{34}\mathrm{cm}^{-2}\mathrm{s}^{-1}$]	3.4	5.8
Power per beam	$P_b/2$ [MW]	11.3	17.5

Table 3.1: LC parameters for the baseline design of TESLA [17].

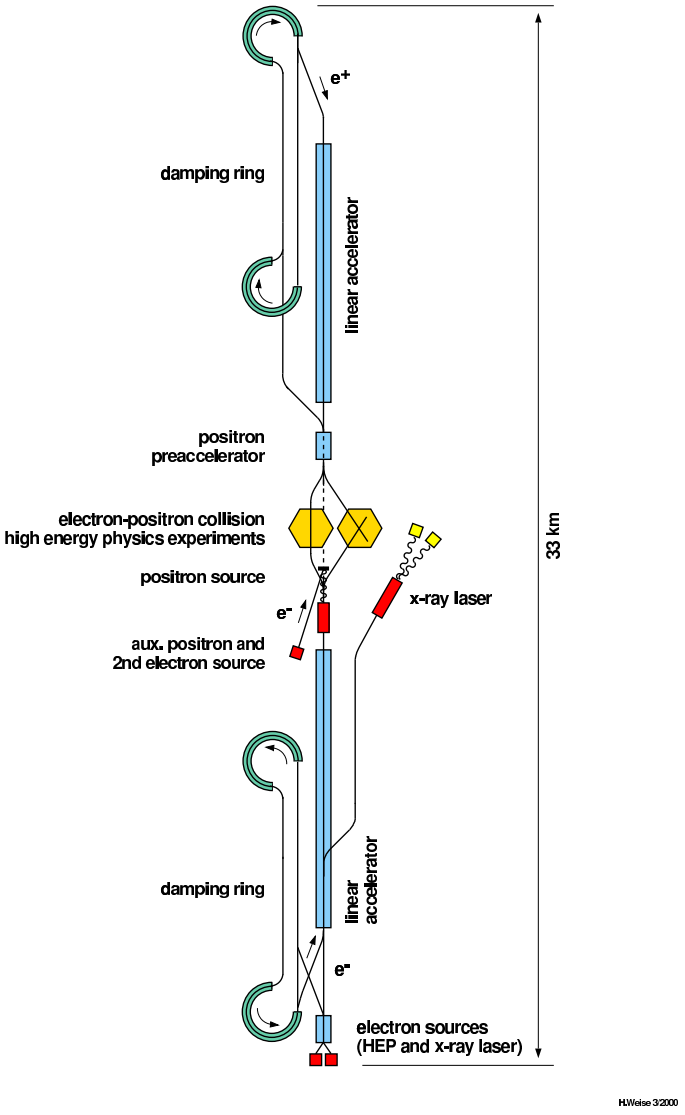

Figure 3.2: Sketch of the overall TESLA layout with the optional second interaction point [17]. The X-ray laser facility is now being built separately.

3.1.1.3 The Linear Collider

A linear collider is built up with various sections, which all provide a specific and different task. A brief overview is given in the following section. The low energy beam from the injector is accelerated before being injected into a damping ring to reduce its emittance. The bunches are then sent to a bunch compressor and finally into the main linac (linear accelerator) before reaching the beam delivery system and the interaction region.

Injector The injection systems provide the electrons and positrons for each beam with the required time structure and charge per bunch. Its design is, for TESLA, based on the existing TTF (TESLA Test Facility) accelerator. The electron beam is generated in a laser-driven gun via the photoelectric effect: a laser is directed to a Cs_2Te photocathode which generates photoelectrons. These are then accelerated by DC voltage. The positrons are created via e^+e^- pair production by directing high energy photons on a target. For the current designs two approaches are foreseen: the first approach, said to be conventional, makes use of high energy electrons which strike a thick target. The primary electrons generate high energy photons via bremsstrahlung, and these are converted within the same target into the electron positron pairs. In the second approach, photons are primarily generated in an undulator, where high energy electrons ($\geq$150 GeV) are passed through to produce high energy photons. The undulator consists of a series of dipole magnets. The alternating field, set up by the alternating dipole arrangement within the undulator, causes the beam to oscillate in its trajectory and photons are then emitted. The second approach has the advantage of having much less power deposition in the target and the emittance can be constrained. TESLA foresees the use of the second approach and its design integrates an undulator at the end of the electron acceleration, upstream of the interaction region. Both beams, electron and positron, are then accelerated by superconducting structures up to the energy required for the damping ring. (5 GeV for TESLA).

Damping Ring In order to produce a minimum spot size at the interaction point, it is necessary to minimise the transverse emittance of the beam. The damping rings are used to reduce the transverse beam emittance, by the use of synchrotron energy radiation losses. The beams are injected into the damping ring and circulate many times: When the particles pass around the arcs in the damping ring, their curved trajectories cause synchrotron radiation (SR) to be emitted, reducing the energy of the particles. The particle is then accelerated. This narrows the angle of the electrons within the beam and reduce the emittance.

In addition wigglers, similar technology to undulators, are also used in one of the straight sections of the damping ring to further increase the damping rate per revolution.

A "chicane" is introduced after the damping ring and before the main linac to compress the beam longitudinally. The relative path length differences for low and high energy parts of the bunch cause the bunch to compress longitudinally. The bunches can then be sent to the main accelerator.

Main Linac The core of the TESLA project is the accelerator called the main linac. The electron and positron beams are accelerated from 5 to 250 GeV at a gradient of E_{acc}=23.4 MV/m for the 500 GeV case. The electron and positron linacs have a total length of 14.4 km each. The 10296 9-cell cavities per linac are contained in cryomodules which also house focusing quadrupoles, steering magnets and beam position monitors (BPM).

Beam Delivery System The Beam Delivery System (BDS) transports the beams from the exit of the linacs to the interaction point, where they are brought into collision. It serves several functions, such as producing the strong demagnification to obtain the small beam size at the IP, chromatic corrections, collimation, maintaining the beam in collision with the help of a feedback system and providing diagnostics for the emittance measurements.

3.2 TESLA Detector

The physics programme discussed in Chap. 1 is translated into detection requirements. From a general point of view, the detector has to provide good tracking and energy resolution. In addition, high hermeticity is needed in order to let as few particles as possible escape undetected.

3.2.1 Overview

The overall detector is foreseen to be 14.8 m in length and 14.9 m in diameter. It consists of vertexing detectors, tracking devices and electromagnetic and hadronic calorimeters. A superconducting coil provides a large magnetic field of 4 T throughout the central detector.

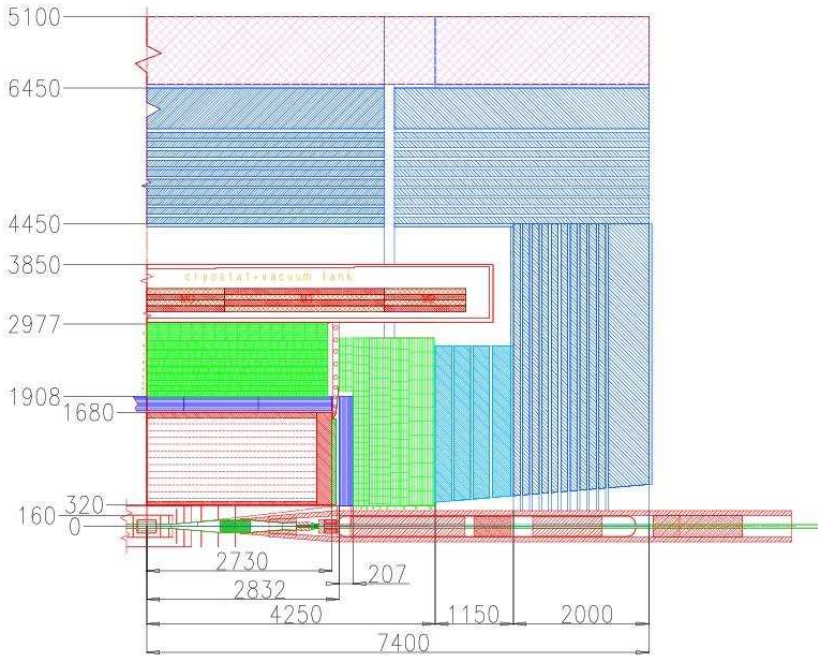

Figure 3.3: Quadrant view of the TESLA detector [22].

3.2.2 Tracking System

The tracking system surrounds the IP and measures particle tracks before they enter the calorimeter. Its components are, from the inner-most to the outer most, a vertex detector (VTX), silicon tracking detectors in the barrel (SIT) and in the forward region(FTD), a Time Projection Chamber (TPC) and a forward chamber (FCH) behind the TPC.

- As close as possible to the IP lies the multi-layered pixel micro-vertex detector with an inner radius of 1.5 cm and an outer radius of 6 cm. It

is primarily optimised to reconstruct secondary vertices in b and c-quark decays;

- The main role of the silicon tracking detectors is to improve the momentum resolution by the addition of a few very precisely spaced points at comparatively large distances from the IP. The SIT consists of two cylinders of double sided silicon strip detectors. The required resolution in $r\phi$ is 10 μm. The z measurement of the SIT is mainly needed to improve the track finding efficiency. For this purpose a resolution of 50 μm is considered sufficient;

- the FTD consists of pixel detectors in the first three layers and strip detectors in the last four. The resolution requirement is 25 μm;

- The large Time Projection Chamber (TPC) will play a central role in both finding and measuring the charged particles. To ensure good solid angle coverage, good track resolution, and simultaneously good determination of the specific energy loss (dE/dx) of particles, many points need to be measured along each track; 200 such points are foreseen for the TPC. This dictates that the chamber should be rather large, both radially and longitudinally, limiting as well the possible total amount of energy loss of the incoming particles. The TPC with an outer radius of 170 cm and an overall length of 556 cm consists of two gas-filled chambers separated by a cathodic membrane. The radiation length from the inner side of the TPC to the outer side is 0.03 X_o. The actual preferred readout technologies are the Gas Electron Multipliers (GEM) type consisting of a thin polymer foil perforated by a high density of small holes or Micromegas type build up with thin metallic meshes;

- The forward Chambers (FCH) extend radially from the inner radius of the TPC to just below the outer radius of the TPC field cage and each is approximately 6 cm thick.

The tracking follows the path that the charged particles make in a magnetic field and thus allows their momentum to be measured. For the overall tracking, the

goal of the momentum resolution is $\delta(\frac{1}{p_t}) \leq 5 \times 10^{-5}(GeV/c)^{-1}$.

3.2.3 Calorimetry

3.2.3.1 Overview

A calorimeter is a block of matter that is of sufficient thickness to cause the primary particle to interact and deposit all of its energy in a subsequent "shower" of increasingly lower energy particles. Calorimeters can measure the energy of photons, electrons, positrons and hadrons, but not neutrinos, which interact via the weak force only, or muons, which are too heavy to lose sufficiently rapidly energy by radiation.

After interaction with an incoming particle, the internal structure of the calorimeter is in an excited state. The return to the fundamental state occurs through the emission of an electrical, optical or thermal signal which is proportional to the incoming particle energy. Getting the signal with the appropriate calibration leads to the determination of its energy.

3.2.3.2 Electromagnetic and Hadronic Calorimeters

The main components of the calorimetry in the TESLA detector are the electromagnetic calorimeter (ECAL) and the hadronic calorimeter (HCAL). Both calorimeters are anticipated to be dense and hermetic sampling detectors with high granularity in order to separate the contribution of different particles and measure their four momenta.

3.2.3.3 Forward Calorimetry

The forward calorimeters extend the hermeticity of the overall detector, as required by many possible new physics signatures. In addition the instrumentation of the forward region plays a crucial role in the measurement of the luminosity and its spectrum.

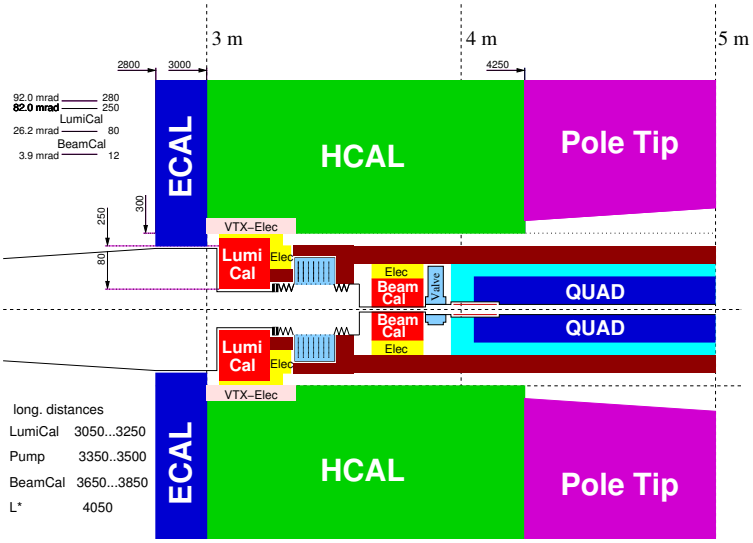

Figure 3.4: Design of the forward calorimetry with focal length l*=4.05 m.

The maximum distance of the forward calorimeters to the interaction region is mainly determined by the focal length l* of the final focus system. The present layout of the calorimeters corresponds to l*=4.05 m as shown in Fig. 3.4. The calorimetric coverage of the solid angle is completed by two devices in the very forward region on both sides of the interaction point, the low angle calorimeter (BeamCal) and the luminosity calorimeter (LumiCal). The LumiCal will be used primarily to provide good calorimetric coverage in the region between 82 and 26 mrad. The BeamCal covers the regime down to very small angles approximately 4 mrad.

The BeamCal: This extends the hermeticity of the overall detector down to the beampipe. Its purpose is to make measurements of the spatial and spectral distribution of the beamstrahlung. In addition it can measure or provide a veto for high energy electrons from two-photon processes to angles as close as possible to the beam pipe. These have particular importance for physics processes with missing energy and momentum [7]. The calorimeter is also a shield for the central part of the detector against backscattered particles, induced by beamstrahlung remnants downstream in the beamline, and synchrotron radiation. One option for the BeamCal is a tungsten sampling calorimeter. The proposed detector consists of aproximately 63 planes of tungsten and silicon or diamond for the interspaced

active sensors. The performance study of the BeamCal has been detailed in [2, 8].

The Luminosity calorimeter: The LumiCal is planned to be located at a distance of 300 cm approximately on both sides of the interaction point, covering an annular surface between radii of 8.0 cm and 25.0 cm from the beam line and polar angle[1] θ between 26 and 82 mrad. The calorimeter is expected to be a silicon tungsten sandwich detector with a similar structure to the calorimeter shown in Fig.3.5 [8]. It is subdivided radially in cylinders, azimuthally in sectors

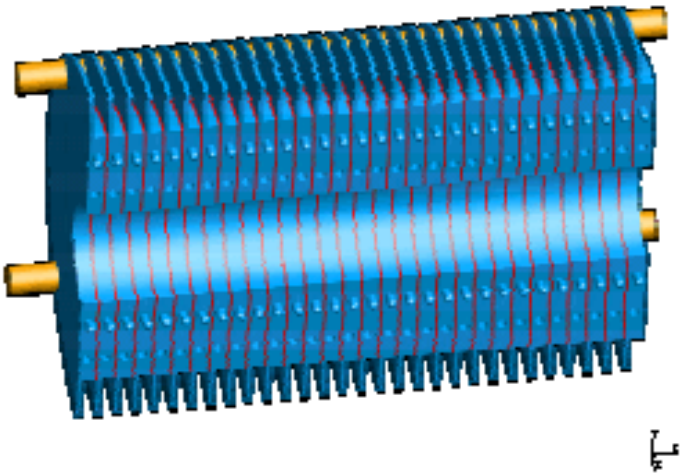

Figure 3.5: The structure of the half barrel of the luminosity calorimeter. The sensors are interspersed between the tungsten disks.

and longitudinally in rings. Each ring consists of tungsten and a sensor plane. The thickness of a tungsten disk is one radiation length i.e. 3.5 mm.

An energy resolution of $25\% \times \sqrt{E[GeV]}$ has been assumed [8] although the luminosity calorimeter geometry is, at the time of writing, under modification and the resulting resolution is under study.

3.2.4 Muon System

The basic task of the muon system is to provide muon identification and serve as a flag or a tail catcher for hadronic showers. The muon detector is located behind

[1] the polar angle θ and the azimuthal angle ϕ are defined w.r.t. z and x, respectively.

the calorimeters and the coil. The iron of the flux return for the 4T magnetic field of TESLA is used as an absorber with a thickness of 1.6m. The overall longitudinal size of the muon identifier is foreseen to be 14.4m and to extend radially from 3.80 to 5.80 m for the barrel.

Bibliography

[1] R. Brinkmann, K. Flottmann, J. Rossbach, P. Schmuser, N. Walker and H. Weise, "TESLA: The superconducting electron positron linear collider with an integrated X-ray laser laboratory. Technical design report. Pt. 2: The accelerator," DESY-01-011 [2]

[2] T. Behnke, S. Bertolucci, R. D. Heuer and R. Settles, "TESLA: The superconducting electron positron linear collider with an integrated X-ray laser laboratory. Technical design report. Pt. 4: A detector for TESLA," DESY-01-011

[3] B. Rossi, "High Energy Particles", Prentice-Hall, Inc., Englewood Cliffs, NJ, 1952.

[4] M.J. Berger and S.M. Seltzer, Tables of Energy Losses and Ranges of Electrons and Positrons, National Aeronautics and Space Administration Report NASA-SP-3012, Washington DC 1964.

[5] W. H. Tait, "Radiation Detection," London, UK: Butterworth (1980) 406p

[6] J. Hauschildt, "Studies on a silicon intermediate tracker for the TESLA detector," LC-DET-2001-036

[7] P. Bambade, M. Berggren, F. Richard and Z. Zhang, "Experimental implications for a linear collider of the SUSY dark matter scenario," arXiv:hep-ph/0406010.

[8] H. Abramowicz et al., "Instrumentation of the very forward region of a linear collider detector", to apear in IEEE transactions of Nuclear Science, Oct. 2004

[9] C. J. S. Damerell [LCFI collaboration], LC-DET-2001-023

Chapter 4

The Laser Wire Project

4.1 From Emittance to Luminosity

The evolution of a beam of particles through a beam transport system can be characterised by the evolution of its transverse phase space. A graphical representation of the phase space gives the angle of motion and position of every particle in the beam. It is customary to define an ellipse in phase space containing a certain percentage, traditionally 95%, of the beam particles, called the phase ellipse as shown in Fig. 4.1. The area enclosed by the ellipse is called the beam emittance ϵ defined, for example in the x-plane, by

$$\int_{ellipse} dx dx' = \pi\epsilon \tag{4.1}$$

where $x' = \frac{dx}{dz}$ is the angle of the individual particles with respect to the nominal beam direction. The emittance is a measure of the beam quality. Two different emittances are defined in the transverse plane: the horizontal emittance ϵ_x, and the vertical emittance ϵ_y. A property of the phase space is that its area is invariant if only focusing and bending forces are applied to the beam. This conservation law is called the Liouville theorem. Thus the emittance is an invariant in a beam delivery system of a linear collider where the particle energy is constant. To account for changes in the particle momentum and deal with a conserved emittance, a "normalised emittance" ϵ_n is defined which is proportional to the

relativity parameters $\beta\gamma$[1] as

$$\epsilon_n = (\beta\gamma)\epsilon \tag{4.2}$$

The trajectory of a particle through an arbitrary beam transport system can be

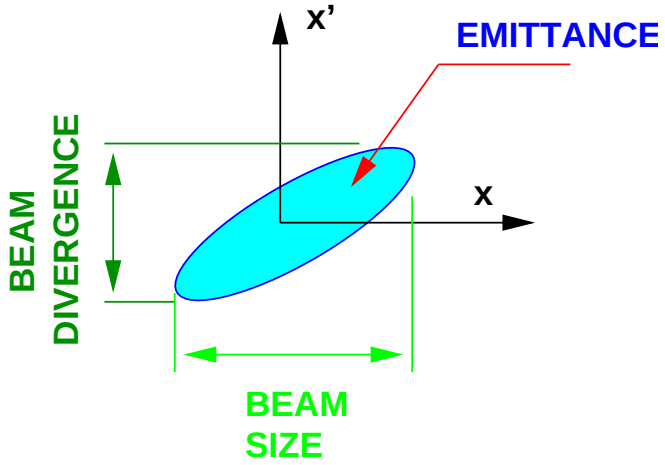

Figure 4.1: Phase space diagram in one dimension.

determined by its betatron function. It is a characteristic of the focusing forces applied to the beam and is highly dependent on the particular arrangement of quadrupole magnets. It is also called amplitude function as it defines the aspect ratio of the ellipse semi-axes in the x direction over the one in x' direction.

Both the betatron function and the beam emittance determine the luminosity of the colliding beams at the interaction point [1],

$$\mathcal{L} = f_c \frac{N_b^2 H_D}{4\pi \sqrt{\epsilon_x^* \beta_x^*} \sqrt{\epsilon_y^* \beta_y^*}} \tag{4.3}$$

where $\mathcal{L}$ is the luminosity for the head-on symmetric gaussian beam collision, N_b is the number of particle in each bunch (considered equal), f_c is the repetition rate times the number of bunches per bunch train, H_D is the enhancement factor due to pinch and hourglass effects, β_i^* is the betatron function for the transverse i-dimension ($i = x, y$) at the interaction point, ϵ_i^* is the emittance and the relation $\sigma_i^* = \sqrt{\epsilon_i^* \beta_i^*}$ was used. For maximum luminosity, as indicated in Eq. 4.3, a value of ϵ_i as small as possible is desirable. The beam delivery system plays an important role for the luminosity performance as it prepares the beam for the interaction as discussed in Sec. 3.1.1.3. It is important that the emittance does

[1] $\beta = \frac{v}{c}$, with c the velocity of light, and $\gamma = \frac{1}{\sqrt{1-\beta^2}}$

not increase significantly in the BDS and therefore a careful monitoring of its value is essential.

4.2 Measuring the Emittance

Since the beam emittance is a measure of both the beam size and the beam divergence, its value can not be measured directly. In drift space, without any optics, the emittance naturally rotates as shown in Fig. 4.2. Thus if the beam size is measured at different locations, different parts of the ellipse can be probed by a beam size monitor and the beam emittance can be determined. Typical

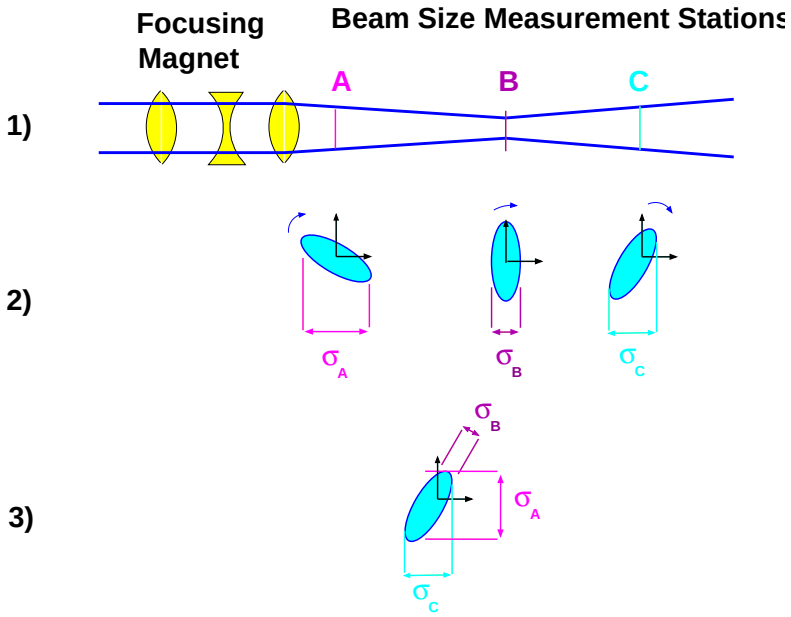

Figure 4.2: The emittance measurements: the beam envelope propagates in drift space (1). Snapshots of the phase space at several measurement stations is performed (2). The projection is then used to determine the ellipse of the emittance.

BDS beam sizes for TESLA, CLIC and NLC/GLC are listed in Tab. 4.1. The electron bunch transverse profile has been measured in the past by intersecting the electron beam with a solid wire and by counting the subsequent background rate as a function of the relative position of wire and bunch. Using this technique, resolutions of typically a few μm can be obtained, at the expense of some significant disruption to the beam. This technique cannot be used universally at

		CLIC	NLC/GLC	TESLA
BDS	σ_x [μm]	3.4 to 15	7 to 15	20 to 150
	σ_y [μm]	0.35 to 2.6	1 to 5	1 to 25

Table 4.1: Beam spot sizes for various Linear Collider designs. Quoted numbers for CLIC [5], NLC/GLC [6] and TESLA [7].

the ILC, however, because the beam spot sizes can be much smaller, the need for continuous measurement precludes an invasive technique and the intensities are so great that the wires would be quickly damaged, even if swept rapidly through the beam. For these reasons, it is necessary to develop a novel technique that can run continuously and reliably during machine operation, that does not get destroyed by the beam and that can be sufficiently fast so as to be sensitive to individual electron bunches within bunch train. A laser based profile monitor is non-invasive and disturbs very little the observed beam [3]. It has as well the advantage of having a minimum measurement size substantially smaller than the fibres used for the solid wire technique. The laser-wire, described in detail in the following sections, provides such a tool to monitor the beam size. At least five stations will be required for each lepton beam, possibly fired by a single laser system. Each station will need to provide a profile along two directions.

4.3 Principle of the Laser-Wire

The laser wire measures the transverse electron beam size by scanning a narrow laser beam transversely over an electron beam as shown in the layout of Fig. 4.3. A high power laser beam is divided into two different optical paths for scanning the horizontal and vertical beam size. The strongly focused laser beams interact with the electron bunch creating Compton scattered photons. The electron beam is then bent away while the Compton scattered photons travel along a straight line, where they are detected with a calorimeter. Scattered electrons are bent more strongly than particles with the nominal energy, enabling detection at a

location after the bending magnet. The proof of principle of this technique was

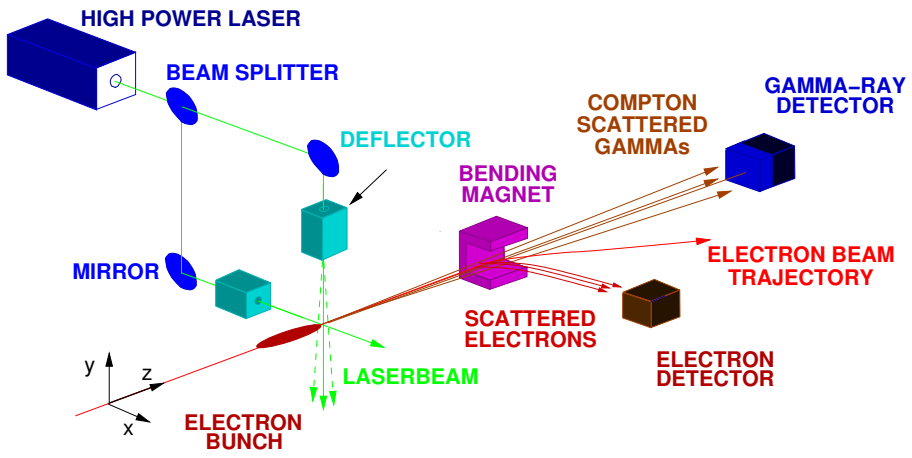

Figure 4.3: Layout of the laser-wire.

first demonstrated at the Stanford Linear Collider (SLC) [4] and a different design is presently being tested at the Accelerator Test Facility (ATF) at KEK [8, 9, 10]. The SLC design used a high power pulsed laser beam, transported over 17 m to the IP within the Stanford Linear Detector (SLD) experiment. The very tight space and accessibility of this location led to a highly engineered design, with the laser position fixed in space. The operation of the device then required the electron beam to be scanned across the laser beam and, in this sense, this laser wire was still an invasive device. The ATF design uses a continuous wave laser and the entire optical system is moved relative to the electron beam using stepping motors. The aim of the Laser Based Beam Diagnostic (LBBD) [11] collaboration is to elevate these design to a compact, non-invasive device where a high power pulsed laser is scanned across the electron beam using either piezo-driven mirrors, acousto-optic devices or electro-optic techniques.

4.4 Gaussian Beam Signal

The laser beam is focused to a small gaussian spot with sigma σ_0. Considering a diffraction limited, finely focused beam waist, the minimal achievable spot radius is given by $\sigma_0 = \lambda/(2\pi\theta)$, where λ denotes the laser wavelength and θ the half

opening angle of the laser beam at the waist as shown in Fig. 4.4. The distance over which the laser beam diverges by $\sqrt{2}$ of its minimum size is called the Rayleigh range x_r and defines the usable length of the laser at the interaction point.

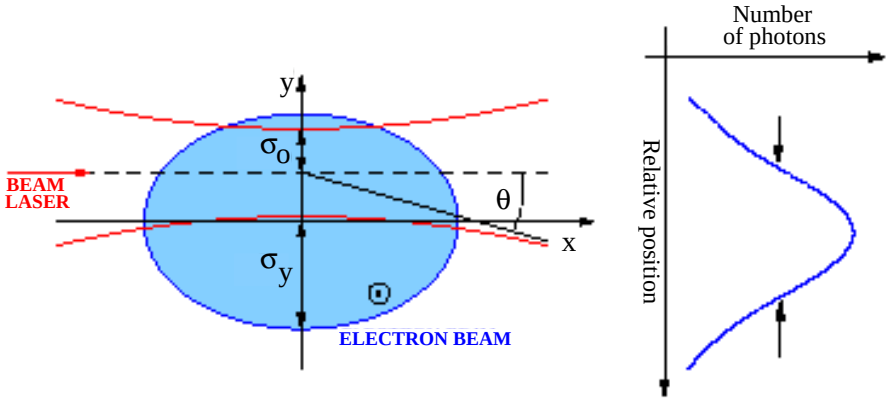

Figure 4.4: Scheme of a gaussian laser beam focused to its diffraction limit scanned over an electron beam.

Given that the electron bunch is shorter than the laser pulse [2], the number of Compton photons per electron bunch/laser pulse crossing is given by [2]

$$N_\gamma = N_b \frac{P_L \sigma_c \lambda}{c^2 h} \frac{1}{\sqrt{2\pi}\sigma_s} \exp \frac{-y^2}{2\sigma_s^2} \int_{-\infty}^{+\infty} dz \exp \frac{-z^2}{2\sigma_z^2} \tag{4.4}$$

where P_L is the instantaneous laser power, N_b is the number of electrons per bunch, $\sigma_s^2 = \sigma_y^2 + \sigma_0^2$ the overlap region corresponding to the quadratic sum of the laser and electron beam sizes and y is the transverse position of the laser spot with respect to the electron bunch centroid. The integral is performed over the length of the laser pulse in z. The number of photons versus the relative position of both beams follows a gaussian distribution as shown in Fig. 4.4 where the peak number of Compton photons per bunch, N_C^{bunch}, occurs when the offset $y = 0$:

$$N_C^{bunch} = N_b \frac{P_L \sigma_c \lambda}{c^2 h} \frac{1}{\sqrt{2\pi}\sigma_s} \tag{4.5}$$

The peak number of Compton photons per bunch is given in Fig. 4.5 as a function of the laser transverse beam size σ_0 for several electron beam sizes σ_y and for a

[2] The electron bunch length at PETRA is 100 ps and the laser bunch length is 12.5 ns as discussed in Sec. 5.5.2

beam energy of 4.5 GeV and a laser power of 2 MW. N_C^{bunch} is approximately 1533 photons with σ_0=1 μm and σ_y=20 μm.

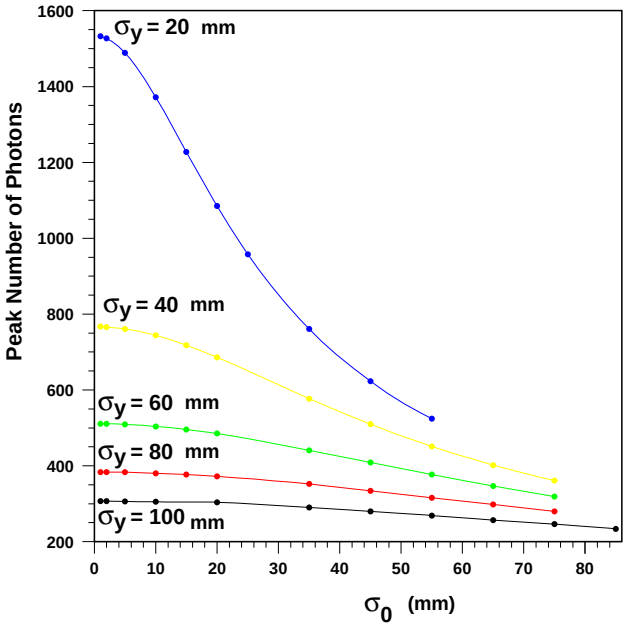

Figure 4.5: Peak number of Compton photons per bunch N_C^{bunch} as a function of the laser transverse beam size σ_0 for several electron beam sizes σ_y. The beam energy is 4.5 GeV, the laser power is 2 MW and the number of electron per bunch is 7 10^{10}, a typical value for the accelerator used later on i.e. PETRA.

4.5 Compton Scattering

The physical process of relevance to the laser-wire is Compton scattering $e^{\pm}+\gamma \rightarrow e^{\pm}+\gamma$, where an unpolarised photon interacts with a relativistic electron (or positron) to give an energy degraded electron and a boosted photon. The cross-section for the Compton scattering electron, is given by [13]

$$\sigma_c = \sigma_o \frac{3}{4}[\frac{1+\epsilon}{\epsilon^2}(\frac{2\epsilon(1+\epsilon)}{1+2\epsilon} - \log(1+2\epsilon)) + \frac{1}{2\epsilon}\log(1+2\epsilon) - \frac{1+3\epsilon}{(1+2\epsilon)^2}] \qquad (4.6)$$

The energy spectrum of the resulting gamma-rays, shown in Fig. 4.6 is given

by [13]:

$$\frac{d\sigma_c}{d\omega} = \frac{3\sigma_o}{8}\left\{\frac{1}{1-\omega} + 1 - \omega + \left[\frac{\omega}{\epsilon(1-\omega)}\right]^2 - \frac{2\omega}{\epsilon(1-\omega)}\right\} \tag{4.7}$$

where $\omega = \frac{\nu_\gamma}{E_{beam}}$ is the gamma-ray energy normalised to the electron beam energy E_{beam}, $\sigma_o = 6.65 \times 10^{-25}$ cm^2 is the Thomson scattering cross-section and $\epsilon = \gamma\frac{\nu_o}{m_e}$ is the photon energy in units of m_e in the electron rest frame. ν_o and ν_γ refer to the incoming and outgoing photon energy respectively [3]. The maximum energy for the scattered photon is $E_{max} = \frac{2E_{beam}\epsilon}{1+2\epsilon}$. The Compton scattered photons' angular distribution is sharply peaked in the initial positron beam direction and the photons are thus confined within a cone of angle $\gamma_c = \frac{1+2\epsilon}{\gamma}$ as seen in Fig. 4.7.

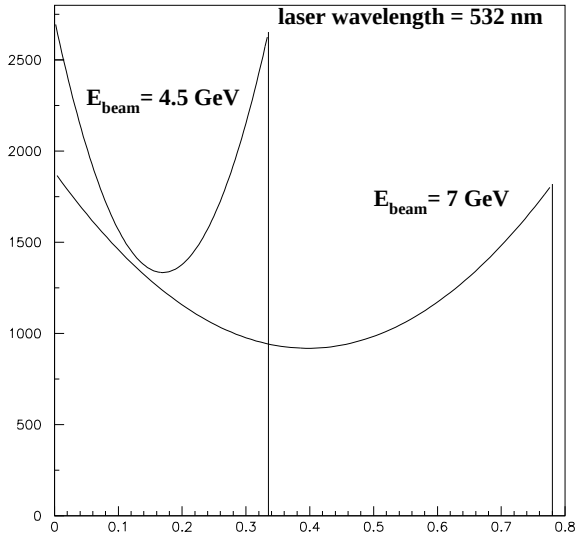

Figure 4.6: Differential cross-section in arbitrary unit of the Compton photon energy ν_γ for an electron beam energy of 4.5 and 7 GeV and a laser wavelength of 532 nm.

In order to measure the total amount of energy coming from the burst of the scattered photons at each interaction a dedicated calorimeter was built, which is detailed in the next chapter. Nonetheless, the first task for the experiment is to define an appropriate location at an accelerator. Prior to this, possible backgrounds for the signal described above are now investigated.

[3] For a laser with wavelength 532 nm, ν_o=2.33 10^{-9} GeV.

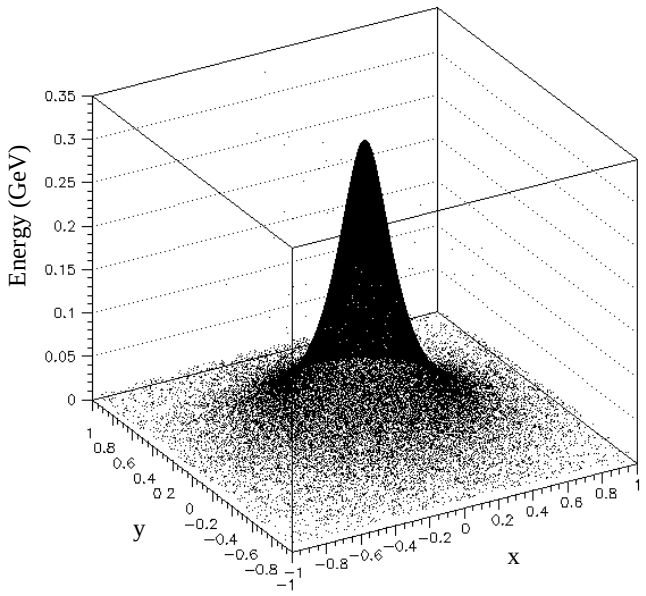

Figure 4.7: Compton energy distribution of individual photons on a vertical plane 14.83 m away for $E_{beam} = 4.5$ GeV. x and y are in cm. This distribution includes showering effects from an aluminium wall of thickness 145 mm.

4.6 Background Processes

Backgrounds are all processes which lead to an additional energy deposit in the detector and hence underly the Compton signal. These backgrounds must be reduced to the extent that the signal / background ratio can be optimised. This background study is of particular importance as it can lead to specific experimental strategies e.g. to build background shields. Preliminary results from simulation and measurements were presented at the Particle Accelerator Conference (PAC) 2001 [15, 16]. In the following section these results are discussed.

Specifically synchrotron radiation, beam gas bremsstrahlung and thermal photon signals are studied. These three processes are the main backgrounds that produce photons in PETRA.

4.6.1 Synchrotron Radiation

Synchrotron Radiation (SR) occurs when a high energy charged particle enters a magnetic field and its trajectory is bent. A subsequent loss of energy is observed as an emission of photons.

The critical photon energy is often used to define SR as it marks the spectral point for which one-half of the total power is irradiated at lower photon energies, and one-half at higher [14]. It is calculated, given the bending magnet at PETRA of $\theta_{dipole} = 28.05$ mrad, using [19]:

$$E_{crit} = \frac{3\hbar}{2} \frac{c\gamma^3 \theta_{dipole}}{L_{dipole}} \tag{4.8}$$

with L_{dipole} the length of the dipole and $\gamma = \frac{E_{beam}}{m_e}$ the Lorentz factor.

SR spectrum generation, specified by E_{crit}, is performed with a Monte Carlo algorithm described in [17]. Fig. 4.8 shows the normalised probability density function (pdf) of the photon energy for such a process.

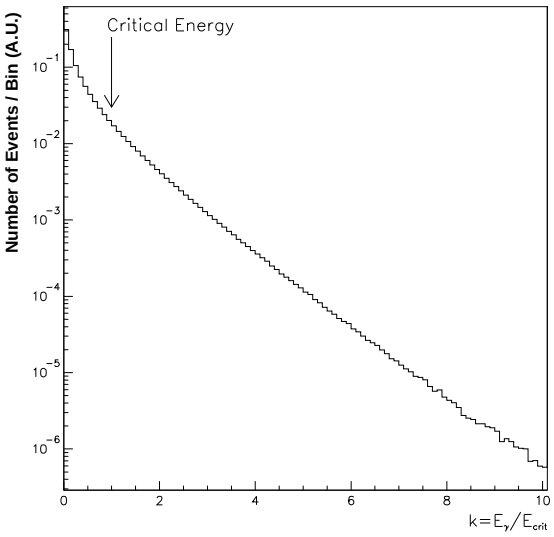

Figure 4.8: Synchrotron radiation probability density function of the photon energy (1 bin = $\frac{1}{10} E_\gamma / E_{crit}$).

The number of SR photons $N_{\gamma_{SR}}$ which are on average emitted per positron in a bunch - seen by a detector of width a at a distance L from the area where

the detector points to, as illustrated in Fig. 4.9 - can be computed using:

$$N_{\gamma_{SR}} = \frac{5\alpha}{2\sqrt{3}}\gamma\frac{dl}{R} \tag{4.9}$$

with $R = \frac{L_{dipole}}{\theta_{dipole}} = 189$ m the bending radius of the magnet, $dl = R\frac{a}{L} = 0.47$m the beam length over which photons emitted tangentially to the beam will enter the detector, and $\alpha = \frac{1}{137}$ the fine structure constant.

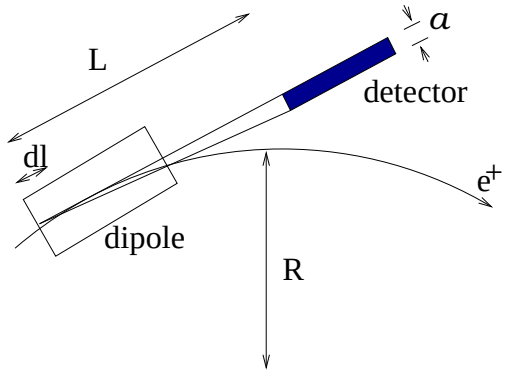

Figure 4.9: Drawing showing the definition of the parameters for the calculation of the number of SR photons.

4.6.2 Bremsstrahlung

Besides SR the beam can lose particles via various interactions eg intrabeam scattering and beam gas scattering. The main background process which can lead to a production of photons, and hence is added to the Compton signal is Bremsstrahlung scattering and is studied below. It occurs when an electron (or positron) is deflected by the nucleus or the electrons within a residual gas atom. The resulting gamma-rays produce a continuous spectrum from zero to the energy E_{beam} of the incoming positron as plotted in Fig. 4.10.

4.6.3 Thermal Photons

A third background component is produced by interaction with thermal photons. Thermal photons originate from the blackbody radiation of the beampipe gas. The radiated photons interact with the positron beam via the Compton process and then give rise to scattered photons.

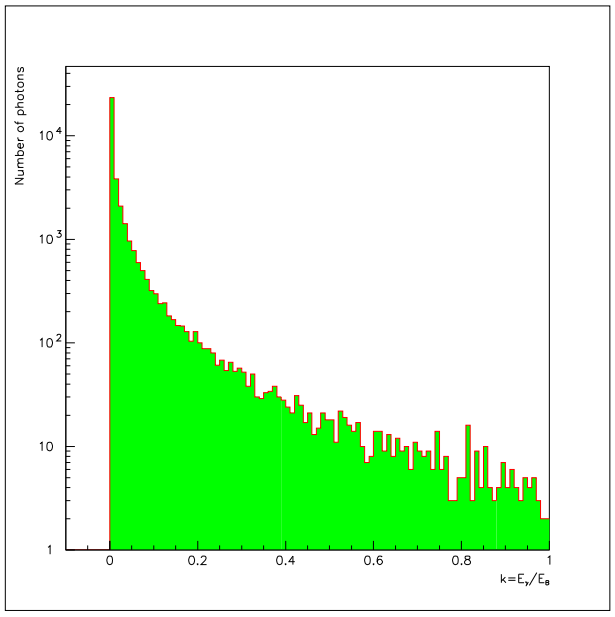

Figure 4.10: Simulation of the bremsstrahlung photon spectrum before passing through any subsequent material.

The density $p_{\gamma_{th}}$ expressed in number of photons per m^3 within a volume, here the beampipe, can be calculated by [18]:

$$p_{\gamma_{th}} = \int_0^{+\infty} \frac{x^2}{e^x - 1}\, dx \frac{(k_B T)^3}{\pi^2 (c\hbar)^3} = \frac{2\zeta(3)(k_B T)^3}{\pi^2 (c\hbar)^3} = \frac{2.4(k_B T)^3}{\pi^2 (c\hbar)^3} \approx 20.2 \cdot T^3 \quad (4.10)$$

where k_B is the Boltzmann constant ($k_B = 8.617 \cdot 10^{-5} eV/k^{-1}$), T is the absolute temperature of the blackbody in Kelvin and $p_{\gamma_{th}} = 5.33 \cdot 10^{14}$ m^{-3} at room temperature ($T \approx 300$ K).

The rate of such collisions per bunch can then be calculated using:

$$N_{\gamma_{th}} = p_{\gamma_{th}} L_{bmp} N_e \sigma_0 \quad (4.11)$$

with N_e the number of electrons (positrons) per bunch, L_{bmp} the length of the beampipe and σ_0 the Thomson cross-section [4]. The values are given below in Sec. 4.7.2.3. The total energy of photons per unit volume is [18]:

$$U(T) = \frac{\pi^2 (k_B T)^4}{15 (c\hbar)^3} \quad (4.12)$$

The average energy of the thermal photons $E_{\gamma_{th}}$ can be derived:

$$E_{\gamma_{th}} = \frac{U(T)}{p_{\gamma_{th}}} = \frac{\pi^4}{15 \times 2.4} k_B T \approx 2.7 k_B T \approx 2.3 \cdot 10^{-4} [T] eV \quad (4.13)$$

[4] Thomson scattering is the scattering of electromagnetic radiation by a charged particle and $\sigma_0 = 6.65 \times 10^{-25}$ cm^2

At room temperature the average photon energy is approximately 0.07 eV.

4.7 PETRA Tests

4.7.1 PETRA Rings

PETRA (Positron Electron Tandem Ring Accelerator) is now a pre-accelerator of positrons and protons for the HERA collider and is as well used as a synchrotron source for the HASYLAB test experiments. The PETRA ring offers positron (or electron) beams with energies typically of 4.5, 7 and 12 GeV with a beam lifetime of 10 hours. It is therefore a very stable machine. It has a circumference of 2304 m and can circulate 40 bunches at the same time, with a minimum inter-bunch distance of 192 ns and a bunch charge of the order of 10^{10} positrons, parameters similar to those foreseen for TESLA. The positron bunch length is typically 100 ps and its beam energy spread is approximately 0.075%.

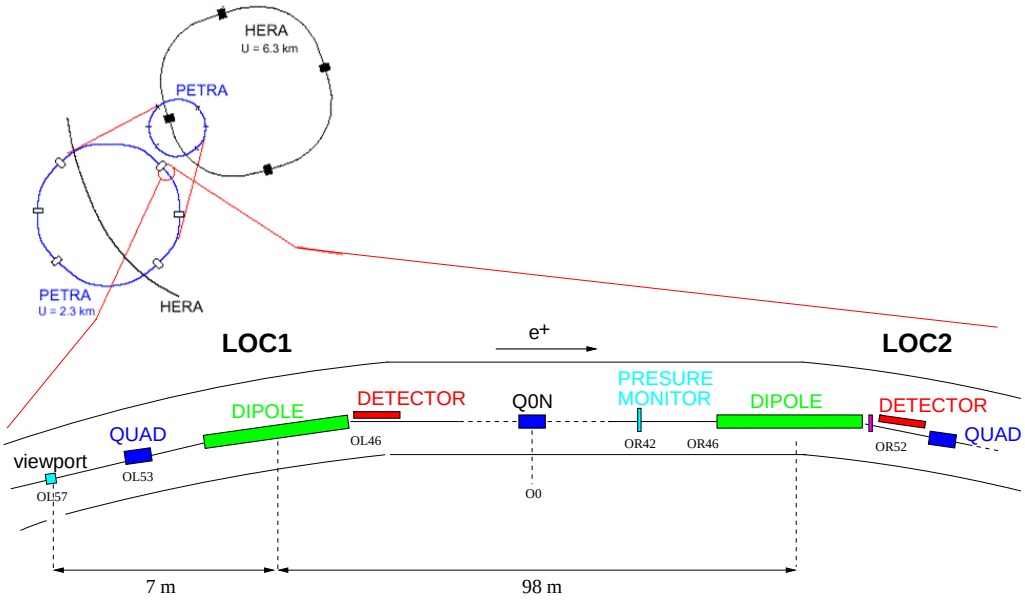

Figure 4.11: Schematics of the PETRA accelerator within the DESY complex and a zoom into the straight section with the two detector locations.

Preliminary background measurements for the same bunch were performed at PETRA at 4.5 GeV and 7 GeV in two different locations (Fig. 4.11) which

were the possible positions for the detector of the laser-wire experiment. The various relevant beam parameters are gathered in Tab. 4.2. Location 1 (LOC1)

Beam energy	4.5 and 7	GeV
Beam current	1.55 to 1.77	mA
Particles per bunch	7.5 to 8.5	10^{10}
Average vacuum pressure	1 to 2	10^{-12}bar
Beam lifetime	10	hours

Table 4.2: PETRA Beam Parameters relevant for background measurements.

is based at the beginning of a straight section behind a dipole whereas location 2 (LOC2) is situated approximately 98m away at the end of the straight section. The detector in location 2 is positioned behind a dipole and placed between a short vertical magnet and a quadrupole. The pressure inside the beampipe is measured using 7 pressure monitors lying along the straight section.

4.7.2 First Background Simulations

A close-up of the experimental setup is displayed in Fig. 4.12. The Compton photons enter the aluminium wall of the beampipe and are then detected. The simulation includes a vacuum beampipe, a dipole, an aluminium beampipe wall and a detector as shown in Fig. 4.13.

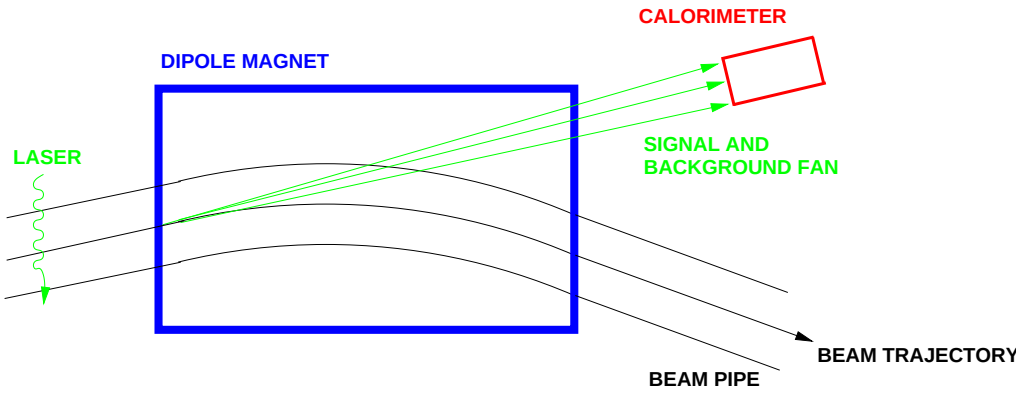

Figure 4.12: Close-up of the experimental setup.

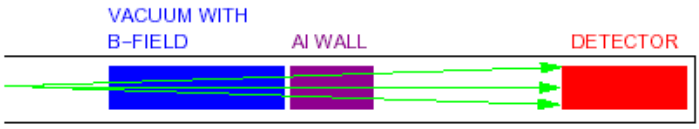

Figure 4.13: Setup of the simulation.

4.7.2.1 Synchrotron Radiation

Synchrotron Radiation backgrounds were simulated using the methods described in Sec. 4.6.1 for two PETRA electron beam energies. The critical photon energies are approximately 1 keV for 4.5 GeV and 4 keV for 7 GeV and the number of emitted photons per positron is 0.231 and 0.360 for 4.5 and 7 GeV respectively. The contribution of SR photons to the overall background spectrum is shown in Fig. 4.14.

4.7.2.2 Bremsstrahlung

Background measurements on the same bunch are presented in Sec.4.7.3.2 with PETRA running at 130 kHz. Thus simulation over 130000 bunches, corresponding to 1 sec. measurement time, was performed with GEANT3 including a straight section of 10 m length for location 1 and 98 m for location 2. Respectively, approximately 0.29 and 2.85 photons are emitted per bunch. The vacuum pressure inside the beampipe was set to $1.5 \cdot 10^{-9}$ mbar.

4.7.2.3 Thermal Photons

The subsequent Compton photon energy distribution is similar to that displayed in Fig. 4.6 but with a maximum energy of approximately 10.8 MeV and 26.2 MeV for positron beams of 4.5 GeV and 7 GeV respectively. The number of radiated photons $N_{\gamma_{th}}$ per bunch is 0.026 for location 1 and 0.26 for location 2.

4.7.2.4 Simulation Conclusions

The backgrounds are added together. Results of the various background simulations are depicted in Fig. 4.14 for an energy range between 0 and 600 keV. The

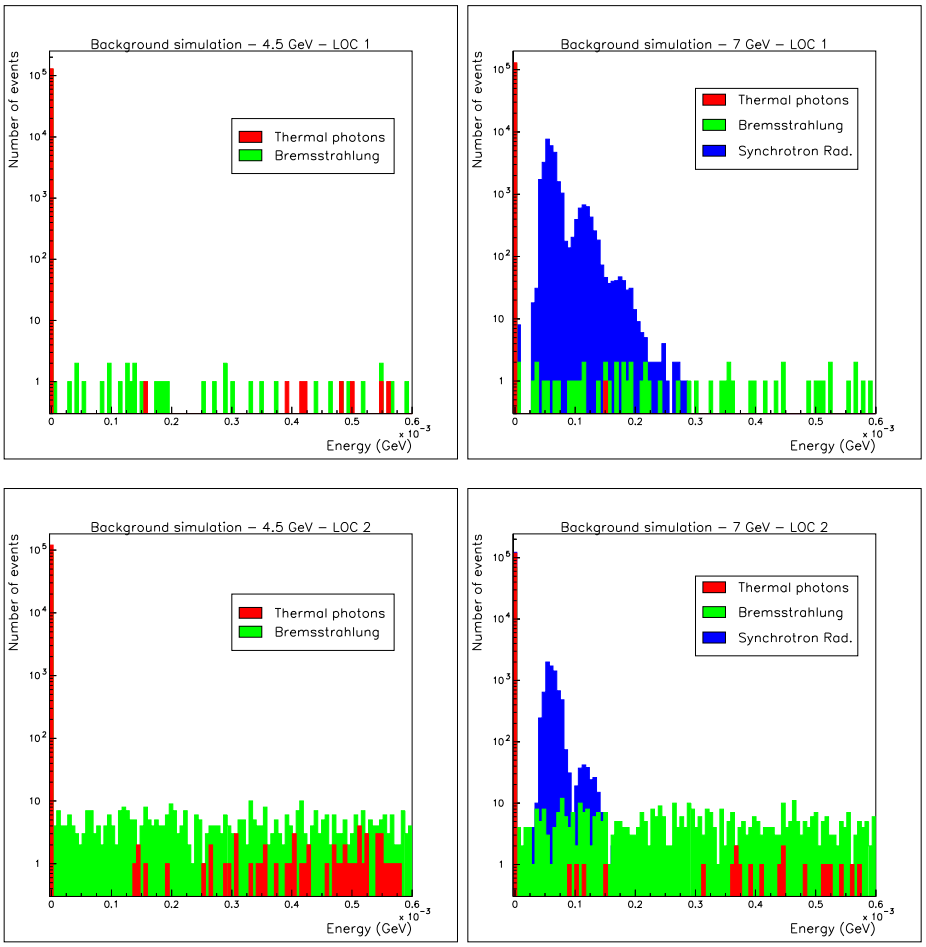

Figure 4.14: Simulation results at two locations for a positron beam energy of 4.5 and 7 GeV over 130000 bunches. No energy resolution from a detector is applied.

results demonstrate that the expected number of events detected, μ, follows a Poisson distribution because of the low number of photons reaching the detector. Thus, for each SR background process the probability P_n for n photons detected after a single bunch is given by:

$$P_n = \frac{\mu^n}{n} e^{-\mu} \tag{4.14}$$

Results from SR simulation have shown that a negligible number of photons go through the beampipe material at 4.5 GeV (upper limit $\approx 1 \cdot 10^{-15}$ photons

per bunch) but at a beam energy of 7 GeV peaks are observed as depicted in Fig. 4.14. Due to Poisson statistics a high peak is obtained when no photons are observed, and following peaks, apart by 60 keV, arise for cases when one, two or more photons reach the detector. Beam gas bremsstrahlung results, presented in Fig. 4.14, show that the bremsstrahlung photon spectrum covers a much wider range of energies than presented in the plots.

4.7.3 First Background Measurements

4.7.3.1 Detector Setup and Calibration

Background measurements were carried out using a CsI(TI) crystal of size 15 × 15 × 100 mm^3 glued to a photomultiplier Hammatsu R268. The light-tight box including the crystal and the photomultiplier was positioned tangentially to the beampipe and 30 cm away from the dipole magnets to avoid any electromagnetic effects on the detector. The signal from the photomultiplier is sent via a charge sensitive pre-amplifier to a shaping circuit. The bipolar output of the shaping circuit is used to generate a clock signal via a discriminator and a gate/delay unit while the unipolar output is connected to an analogue/digital (A/D) board. The calibration was achieved with the 660 keV peak of a ^{137}Cs radioactive source. An attenuator connected between the test pulse and the pre-amplifier was used to obtain the pedestal and hence check that the pedestal corresponds to an energy of zero keV in the final A/D board. Analysis of the calibration data reveals an energy resolution of approximately 4%.

4.7.3.2 Measurements Results

Results of the measurements at both locations with two beam energies are plotted in Fig. 4.15. SR and residual gas bremsstrahlung, described in Sec. 4.7.2, are the two dominant background sources. At 4.5 GeV in both locations the energy of the photons covers the whole measurement spectrum; only photons from gas residual bremsstrahlung reach the detector. In location 2 more photons are de-

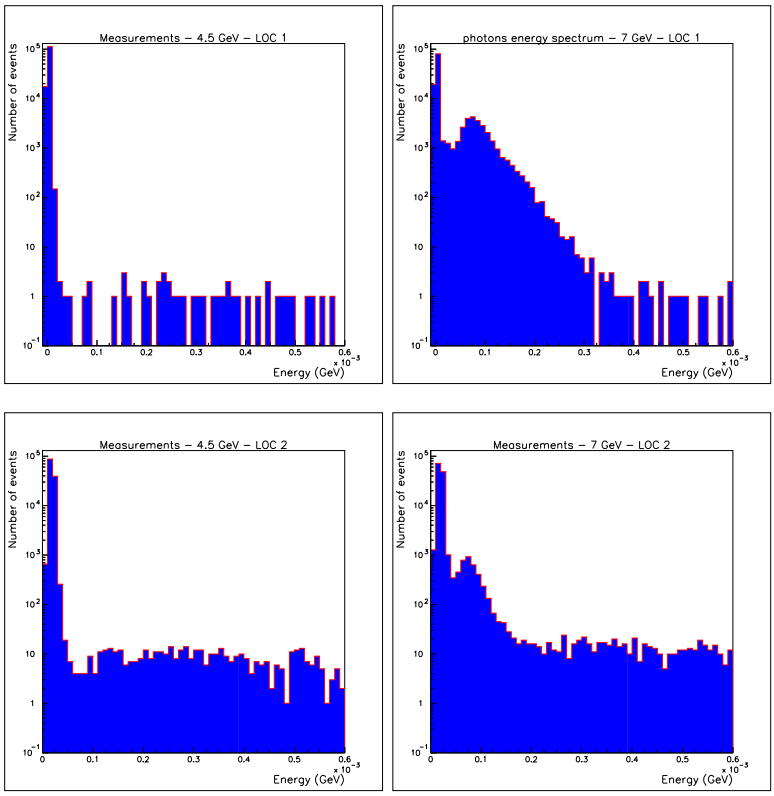

Figure 4.15: Background measurements at two locations for a positron beam energy of 4.5 and 7 GeV. Data is taken over 130000 bunches.

tected. At 7 GeV in both locations peaks are observed at $n \times 60$ keV for integer n, which is the signature of SR as shown in the simulation section. However, in location 1 more photons from this process are observed. A high peak is also found at zero keV in the various figures which corresponds to the case where no photons are detected as expected according to Poisson statistics.

4.8 Conclusion

Measurements and simulations of the background for the PETRA laser-wire experiment were performed at 2 locations and 2 positron beam energies. These indicated a high rate of photons coming from synchrotron radiation but with low energies and a low rate of bremsstrahlung photons with energies possibly as high as the beam energy. The simulations were carried out with 145 mm of aluminium thickness. In fact an effective length of more than 1 m of Aluminium is located in

front of the present calorimeter position due to the shallow angle of the photons in the beampipe. However the conclusion of this study was that backgrounds were not a problem for the PETRA laser-wire (unlike the case at ATF [10]) and so enabled the laser-wire collaboration to proceed with installation of a vacuum vessel at the IP. The laser-wire experiment has since installed a vacuum window that allows effectively all the signal to pass through, while the backgrounds are still under control.

Bibliography

[1] A. W. Chao and M. Tigner, "Handbook of accelerator physics and engineering", Singapore, Singapore, World Scientific (2002) 654 p.

[2] P. Tenenbaum and T. Shintake, "Measurement of small electron-beam spots", Ann. Rev. Nucl. Part. Sci. **49** (1999) 125.

[3] V. I. Telnov, "Is a laser wire a non-invasive method?", Nucl. Instrum. Meth. A **513** (2003) 647

[4] R. Alley *et al.*, "A Laser-Based Beam Profile Monitor For The SLC/SLD Interaction Region", Nucl. Instrum. Meth. A **379** (1996) 363.

[5] R. Assmann *et al.*, "Design status of the CLIC 3-TeV beam delivery system and damping rings", CERN-SL-2000-058-AP

[6] P. Tenenbaum, L. Eriksson, T. Markiewicz, T. O. Raubenheimer and A. Ringwall, "New developments in the Next Linear Collider beam delivery system design", SLAC-PUB-8135

[7] R. Brinkmann, N. Walker, O. Napoly and J. Payet, "A new beam delivery system (BDS) for the TESLA linear collider", DAPNIA-SEA-00-04

[8] Y. Sakamura *et al.*, "Development of a laser wire beam profile monitor. I", arXiv:hep-ex/9907054.

[9] H. Sakai *et al.*, "Development Of A Laser Wire Beam Profile Monitor. II", Nucl. Instrum. Meth. A **455** (2000) 113.

[10] H. Sakai *et al.*, "Measurement Of An Electron Beam Size With A Laser Wire Beam Profile Monitor", Phys. Rev. ST Accel. Beams **4** (2001) 022801.

[11] Laser Based Beam Diagnostic Collaboration, `http://www.pp.rhul.ac.uk/~kamps/lbbd/`

[12] T. Shintake, "Proposal of Nanometer beam size monitor for e+ e- linear colliders", Nucl. Instrum. Meth. A **311** (1992) 453.

[13] I. F. Ginzburg, G. L. Kotkin, V. G. Serbo and V. I. Telnov, "Colliding Gamma e And Gamma Gamma Beams On The Basis Of Single Collision Electron Positron Accelerators", Nucl. Instrum. Meth. A **219** (1984) 5.

[14] G. Margaritondo, "Introduction To Synchrotron Radiation", *New York, USA: Oxford Univ. Pr. (1988) 280p.*

[15] G. A. Blair, J. Frisch, K. Honkavaara, T.Kamps, F. Poirier, I. N. Ross, M. Ross, H. Schlarb, P. Schmuser, S. Screiber, D. Sertore, N. Walker, M. Wendt, K. Wittenburg, "Proposing a Laser Based Beam Size Monitor for the Future Linear Collider", PAC2001, Chicago, TPHA051.

[16] K.Balewski, G. A. Blair, T.Kamps, F. Poirier, D. Sertore, K. Wittenburg, "Simulation Studies and Background Measurements for a Laser Based Beam Size Monitor for Future Linear Collider", PAC2001, Chicago, TPAH052.

[17] H. Burkhardt, "Monte Carlo Generator For Synchrotron Radiation", CERN-LEP-NOTE-632.

[18] B.H. Bransden and C.J. Joachain, "Quantum Mechanics", Prentice Hall, New York 2000.

[19] J. D. Jackson, "Classical Electromagnetics", 2^{nd} edition John Wiley & Sons, New York 1975.

Chapter 5

The Laser- ire Calorimeter and Results at PETRA

The laser-wire uses a finely focused laser beam to measure the transverse profile of positron bunches by detecting the Compton scattered photons. As described in Sec. 4.4, the total energy of the bunch of scattered photons emitted during the interaction of the laser and the positron beam is dependent on their relative positions. A calorimeter is needed to detect the scattered Compton photons. It has to be located close to the beampipe and so be radiation hard. In addition, the calorimeter has to be fast enough to avoid pile-up from successive bunches. Lead-tungstate crystals were chosen to satisfy the above requirements, as described below, and used successfully for the first transverse beam-size measurements with a laser-wire at PETRA.

5.1 Scintillation

Scintillation is the physics process by which absorbed energy in a medium is transformed into photons that can be detected. In an inorganic substance it is essentially a crystal property of insulators and semi-conductors, where the energy between the valence band and the conduction band is of order an electronvolt. Under external radiation, the electron of the valence band can "jump" to the

conduction band (ionisation phenomenon), or, if the energy is not sufficient for the electron to reach the conduction band, it remains bound to a positive hole, creating an electron-hole combination in an excited state, called an exciton. Luminescence then appears with the subsequent recombination as shown in Fig. 5.1. This description can only be applied to perfect (or intrinsic) crystal lattices. In

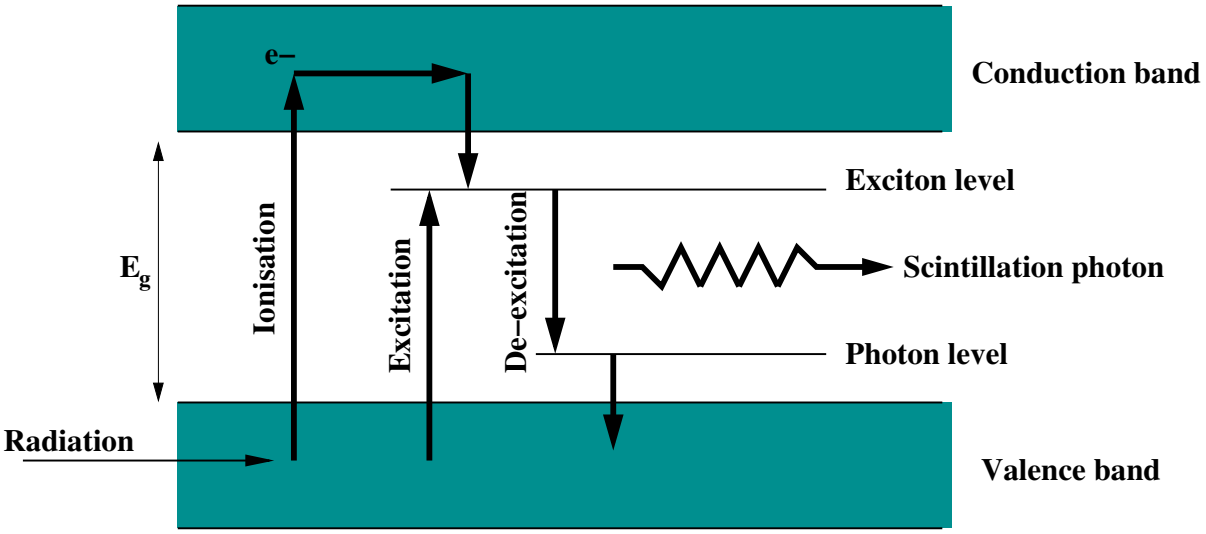

Figure 5.1: Scintillation process in intrinsic inorganic crystals [5].

most cases, luminescence is due to an emission centre consisting of impurities introduced with a controlled quantity. These impurities are energetically localised between the valence and conduction band thereby creating additional energy levels. The capture of an electron from the conduction band, by the centre leads to an excited state. Return to the fundamental state occurs through various ways [1]: if it is a luminescent centre, the transition is radiative and if it is a "quenching" centre, the transition is non radiative and the excitation energy of the centre is thermally dissipated.

$PbWO_4$ scintillation - Lead tungstate scintillation mechanisms are not all known, and research on this subject is difficult because each crystal, which can not be built rigorously under exactly the same conditions has different properties. Nonetheless there are two distinguishable emission lines, one blue line at 420 nm and a green line at 500 nm.

Lead tungstate consists of Pb^{2+} ions bound to the so called centres $W0_4^{2-}$ and

Density	8.28 g/cm^3
Radiation length	0.89 cm
Molière radius R_M	2.19 cm
Emission peak	420-440 nm
Decreasing time	15 ns (60%)
	100 ns(1%)
Refractive index	2.3

Table 5.1: $PbWO_4$ crystal characteristics.

(WO_3 + F) within the matrix forming the crystal, with F being an impurity in the crystal. Each scintillation line is due to the activation of the lead ions associated with each centre. Thus the blue line corresponds to the exciton of the lead, bound to the $(WO_4)^{2-}$ group. This constitutes the characteristic luminescence centre of tungstates. The peak of the emission spectrum for the lead tungstate crystal is typically around 420 nm for photoluminescence and 440 nm for radioluminescence [3]. A subsequent light collection system has to be carefully chosen in accordance with these peak emissions.

5.2 Lead Tungstate Crystals

Lead tungstate crystals were chosen for their compactness, their fast response and their radiation hardness; Tab. 5.1 lists their main characteristics. The CMS electromagnetic calorimeter [6] R&D programme of the last few years has led to a better understanding of the radiation damage mechanism. The main conclusion is that radiation affects neither the scintillation mechanism nor the uniformity of the light yield along the crystal. It only affects the transparency of the crystals through the formation of color centres and the transport of light is changed by self-absorption of the crystals [2]. Most of the light is collected within 100 ns which makes $PbWO_4$ a very fast scintillator.

The main problem with the crystals is the high sensitivity of their light yield

to temperature variation. Previous studies by the CMS group has indicated a temperature dependence of -1.98%/K in the temperature region of 250-300 K. A more detailed study on the dependence of the calorimeter output with temperature variation is presented later on.

5.3 Detector Geometry

5.3.1 Individual Crystal Description

Lead tungstate has a radiation length and Molière radius of 0.89 and 2.19 cm respectively, which makes electro-magnetic showers compact compared to other scintillation materials. Simulation performed with GEANT4 [4] and taking into account various $PbWO_4$ crystal sizes, indicates that a length of 150 mm and an overall front face of 54 mm is enough to contain 91% of the electromagnetic shower from an incoming 300 MeV photon as displayed in Fig. 5.3. In addition in order to optimise the collection of light inside the crystal and minimise the loss, the crystals are polished as shown in the Fig. 5.2. They are also non tapered in order to fit easily together.

Figure 5.2: Single 150 mm long lead tungstate crystal picture as used for the laser-wire calorimeter.

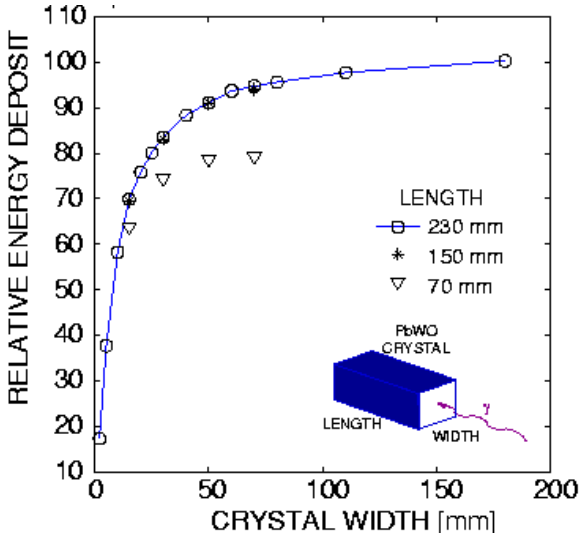

Figure 5.3: Relative energy deposit for 300 MeV photons inside the crystal as obtained from the simulation with Geant4.

5.3.1.1 Crystal Matrix

The final choice of the overall size of the active volume of the calorimeter was mainly driven by the available photomultiplier size and the standard size of crystals that could be delivered rapidly at relatively low cost. The crystals are grown in standard sizes of 18, 20 and 22 mm width thus, in order to account for a bigger overall size, it was decided to stack together 9 crystals to form the required width. The 3×3 matrix consists of $18 \times 18 \times 150$ mm $PbWO_4$ crystals wrapped in a highly glossy white film. It is held together by an aluminium structure. The matrix and the PMT are mounted in a light tight aluminium box. A dedicated study was performed at a testbeam and is described below in Sec. 5.4.

5.3.2 Photomultiplier

To collect the photons from the showers developing in the crystals, a single photomultiplier (PMT) Hamamatsu R6091 is connected to one end of the matrix with optical grease BICRON BC-630.

Cathode Luminous Sensitivity (S_k)	91.9 $\mu A/lm$
Anode Luminous Sensitivity (S_a)	708.0 A/lm
Cathode Blue Sensitivity Index (S_{kf})	10.30
Transit time	48 ns
Sensitive surface	65 mm

Table 5.2: R6091 Photomultiplier tube characteristics.

5.3.2.1 Characteristics

The relevant PMT characteristics are provided in Tab. 5.2 and are described further in the sections below.

- Radiation hardness: no data on the radiation hardness of the PMT were available prior to its use for the laser-wire experiment. To account for possible radiation damage, which would lower the signal, two calibrations at test beams were performed and are described later on.

- Photocathode sensitivity: the photocathode material defines the spectral sensitivity of the PMT. The photocathode for the PMT used is a dedicated bialkali material whose spectral sensitivity characteristics are displayed in Fig. 5.4. The cathode radiant sensitivity, shown in Fig. 5.4, is defined as the ratio of the cathode current to an incident flux in W but it is more customarily specified in terms of photometric units and is thus called the cathode luminous sensitivity s_k, with an incoming flux in lumens as given in Tab. 5.2. The maximum of the spectral response is at 420 nm approximately, which makes the PMT appropriate for $PbWO_4$ light emission as seen in the previous section.

- Gain: the gain of a photomultiplier is the ratio I_a/I_k, where I_a is the anode current due to a cathode photocurrent I_k [5]:

$$G = \frac{I_a}{I_k} = \frac{S_a}{S_k} \tag{5.1}$$

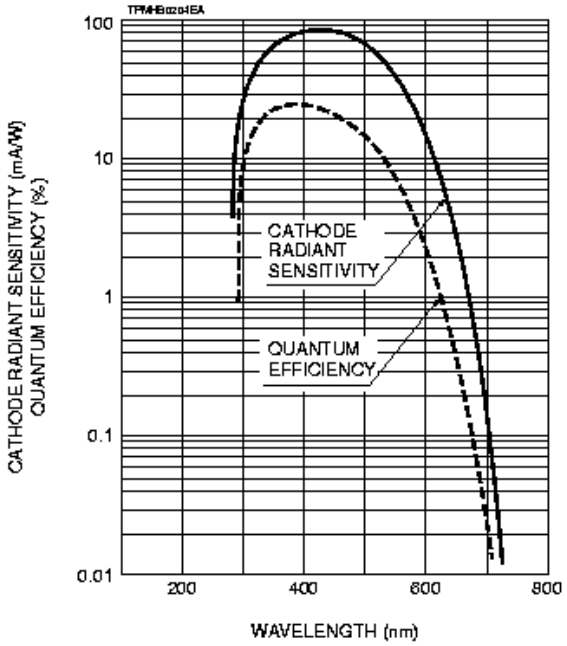

Figure 5.4: Spectral response of the photomultiplier tube R6091. Courtesy of Hamamatsu.

where S_a, the anode luminous sensitivity, is the measured anode intensity for a given luminous flux ϕ_v, thus $S_a = I_a/\phi_v$, and S_k is the cathode luminous sensitivity for a cathode intensity of the same luminous flux; $S_k = I_k/\phi_v$. The gain G_b of a PMT tube for a specific wave-length is given by

$$G_b = \frac{S_a}{S_k \times S_{kf}} \tag{5.2}$$

with S_a, S_k and S_{kf}, the cathode blue sensitivity index, as shown in Tab. 5.2. The gain at room temperature (25^oC) for a wave-length of 430 nm (blue) is 7.48×10^5 for a power supply of 2000 V. The gain increases rapidly as a function of the applied voltage as illustrated in Fig. 5.5 and varies with temperature, wave-length, and mean anode current.

- Transit time: this is interval between the arrival of a light pulse at the cathode of the PMT and that of the corresponding current pulse at the anode. It is equal to 48 ns for the PMT used here.

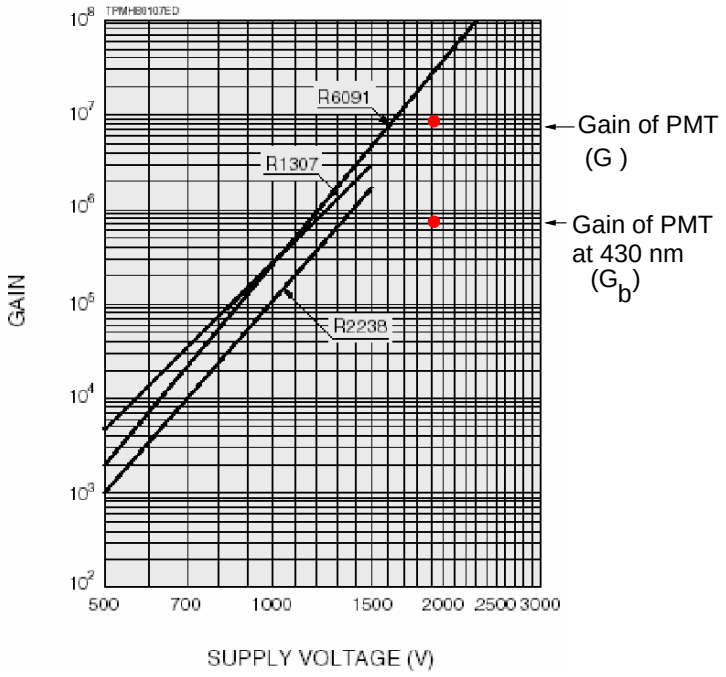

Figure 5.5: Standard R6091 Photomultiplier tube gain as a function of the power supply. Courtesy of Hamamatsu.

5.3.3 Fluctuations of the Signal

In this section we discuss the factors which contribute to and limit the energy resolution of the calorimeter. The precision with which the energy of showering particles can be measured is limited by:

1. fluctuations in the cascade processes through which the energy is degraded,

2. the technique chosen to measure the final products of the cascade processes. It corresponds here to the limit of resolution of the PMT.

Traditionally the energy resolution $\frac{\sigma_E}{E}$ of calorimeters is parameterised with the following relation:

$$\frac{\sigma_E}{E} = \frac{a}{\sqrt{E}} \oplus b \oplus \frac{c}{E} \tag{5.3}$$

where the stochastic term a corresponds to statistical fluctuations of the showers, the constant term b depends on the quality of the detector (calibration and uniformity), the term c is the noise from the electronics.

5.3.3.1 Stochastic Term

A particle depositing an energy E in a crystal creates by scintillation from an electromagnetic shower many photons, from which $N \pm \sqrt{N}$ reach the PMT at the end of the crystal.

We obtain:

$$\frac{\sigma_E}{E} = \frac{1}{\sqrt{N}} \tag{5.4}$$

if $\epsilon = \frac{E}{N}$ is the mean energy necessary to create a scintillation photon then:

$$\frac{\sigma_E}{E} = \sqrt{\frac{\epsilon}{E}} = \frac{a}{\sqrt{E}} \tag{5.5}$$

5.3.3.2 Constant Term

The uniformity of the response (longitudinal and lateral) of the crystals and the calibration precision are transcribed by the constant term b. It includes as well the leakage.

If for an energy E, we obtain the signal s, then $s = zE$ where z is the calibration constant. For uncorrelated variables z and E, the resolution on the signal $\left(\frac{\sigma_s}{s}\right)$ is given by error propagation

$$\left(\frac{\sigma_s}{s}\right)^2 = \left(\frac{\sigma_E}{E}\right)^2 + \left(\frac{\sigma_z}{z}\right)^2 \tag{5.6}$$

and using eq.5.5, the signal resolution becomes

$$\frac{\sigma_s}{s} = \frac{a}{\sqrt{E}} \oplus b \tag{5.7}$$

where the stochastic term a appears again as well as a constant term b depending on the resolution of the calibration constant. This term sets the limit on the performance at very high energies.

5.3.3.3 Electronic Noise

Even in the absence of a showering particle, electronics generate (gaussian) noise. This noise has a direct effect on the charge collection at the end of the electronics. Since the calorimeter measures the energy of showering particles in the same units, this noise term is equivalent to a certain amount of calorimetric energy. Thus its contribution to the overall resolution scales like E^{-1}. This component limits the low energy performance of the calorimeter.

5.3.3.4 Instrumental Effect

The statistical fluctuation of the charge multiplication within the PMT to the total stochastic term can be written:

$$a = a_1 \oplus a_2 \tag{5.8}$$

where a_1 is the term coming from photostatistics in the crystal and a_2 from the PMT fluctuations. Generally, a_2 is dominant with respect to a_1. The PMT fluctuations are mainly due to radiation, temperature and gain instabilities. The PETRA laser-wire collaboration uses a dedicated high voltage supply Fluke 415B with an output stability of +/-0.0020%. The overall resolution of the detector, including crystals and the PMT, is summarised in the next section.

5.4 Performance of the Calorimeter

The performance of the calorimeter was checked in a test beam before and after its use for the laser-wire experiments at PETRA. In the following section the various tests are described.

5.4.1 Testbeam at DESY II

The detector studies were undertaken at the DESY II test beam facility. The DESY II synchrotron is the positron injector for the DORIS and PETRA machines and provides three parasitic electron test beams numbered 21, 22 and 24

[9]. The studies undertaken on the detector took place using beam 24 for most of the preliminary studies and then beam 22 for all the following experiments. The energy range of the beam is from 0.45 to 6 GeV with a maximum rate for electrons of 1 kHz at 3 GeV. As shown on the layout in Fig. 5.6 the beam test 22 is made up of several components. A carbon fibre target of 6-10 μm in diameter positioned in DESY II; a converter target; a bending magnet and two collimators. The carbon fibre target is placed in the circulating beam of DESY II which produces a bremsstrahlung photon beam tangential to the initial electron beam. The photons are then converted to electron-positron pairs by a copper converter target. The magnet is set to allow only electrons with the desired energy through two collimators and thus into the experimental area. The first collimator has an adjustable window width and the second is a block of lead with a hole of 1cm in diameter.

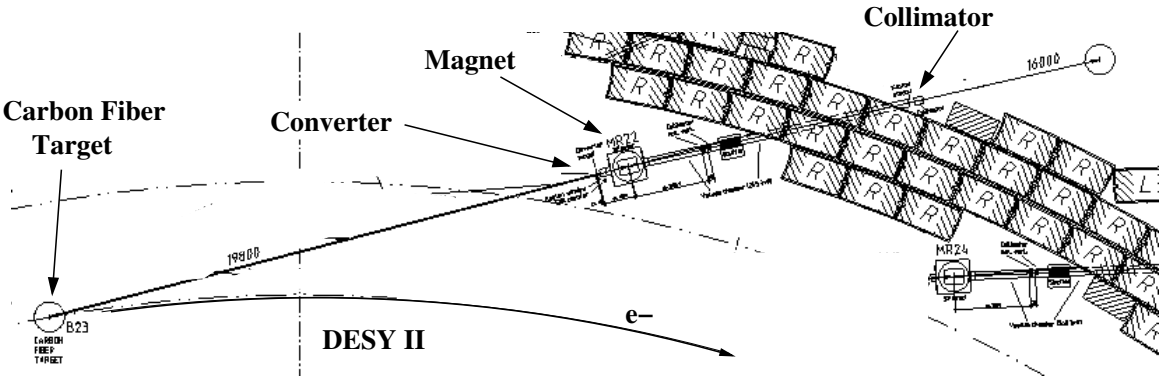

Figure 5.6: Layout of the beamtest 22 at DESY II. The electrons created after conversion of gammas into pairs are deflected by a magnet before going through the collimator.

5.4.2 Installation at DESY II

The detector box was installed on a movable table in the beam axis as shown in Fig. 5.7. Three plastic scintillators, used as triggers, were interspaced between the collimator and the matrix. Two of the scintillators were crossed and positioned 0.8 m from the collimator entrance and defined an active region of angle 3.57 mrad. The third trigger, located 136 mm from the $PbWO_4$ crystals and used for the geometrical studies detailed later on, reduced the sensitive area to

the electron beam at the matrix surface to 0.08 cm^2. Every time an electron goes through two (or three) scintillators it triggers the data acquisition.

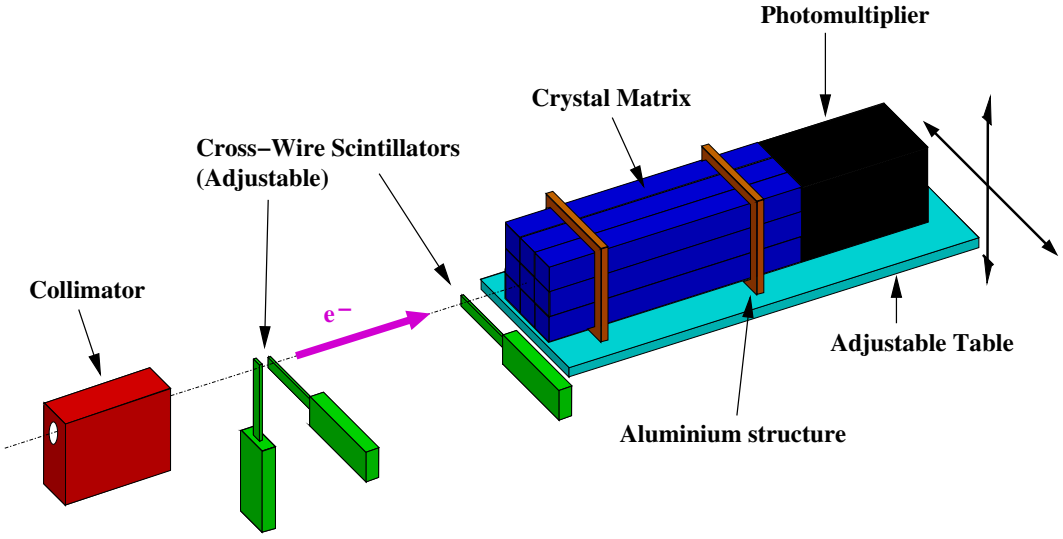

Figure 5.7: 3−Dimensional view of the experiment at the test beam.

The analog signal from the detector is sent to a 12 bit resolution fast PCI-ADC card with maximum input voltage of $\pm 1\ V$ which is externally clocked by the coincidence signal of the scintillators. The card is based on a memory-board with a CMOS-static ram of 10 mega-Bytes and a 10 mega-samples per second ADC-board. The overall electronics layout is shown in Fig. 5.8. The signal was amplified, broadened by a 96 ns shaper and delayed to produce a pulse with low varying amplitude to be easily synchronised with the trigger pulse. An additional delay of 9 ns was applied to the signal to compensate the internal delay of the card. Fig. 5.9 displays the mean output obtained from the card for a fixed signal originating from the detector.

The pulses from the scintillators were amplified and sent to discriminators with threshold set to 50 mV to produce 80 ns logical signals and their coincidence used to provide a TTL clock signal for the PCI-ADC card.

Two identical PCI-ADC cards were used. The digital response of the cards with respect to known voltages was investigated as shown in Fig. 5.10 for the second card and is given in terms of ADC counts/mV in the Tab. 5.3. It shows that cards number one and two have a respective digital resolution of 2.048 and 1.39

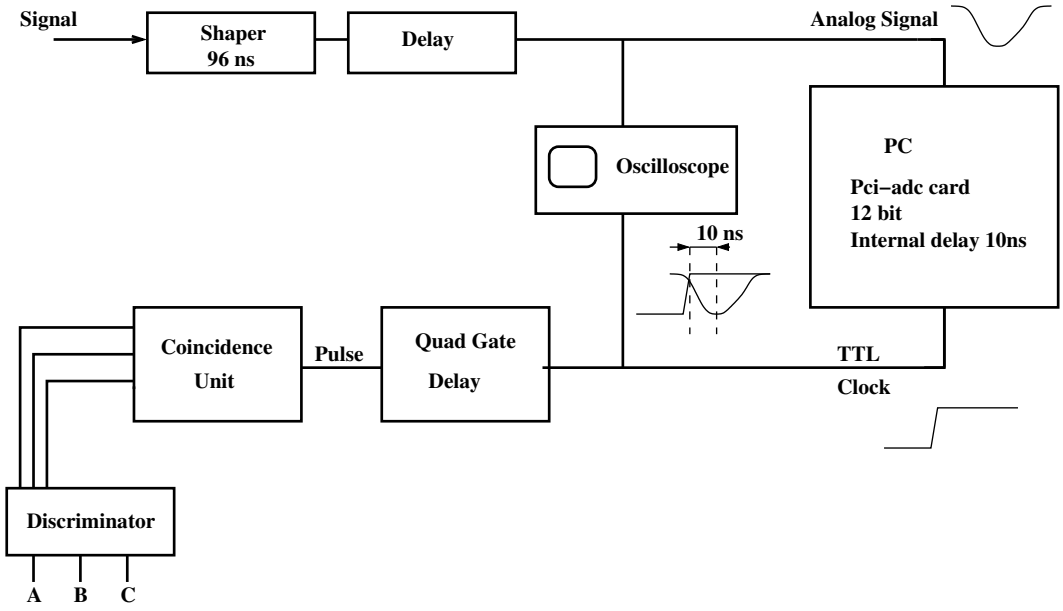

Figure 5.8: Electronic layout.

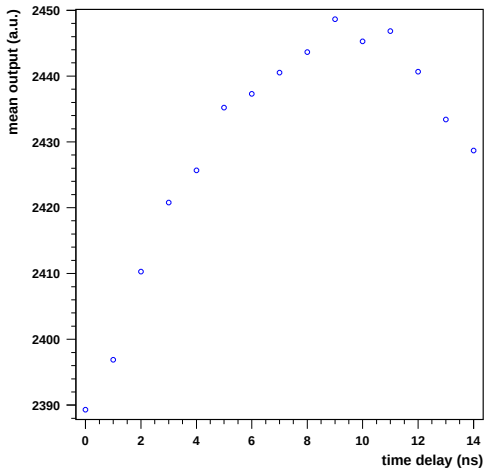

Figure 5.9: Mean output in arbitrary units (a.u.) versus the delay applied to a signal originating from the detector.

ADC counts/mV. The first card was destroyed during background tests at PETRA and only the second card was in use for the consecutive laser scan measurements. This later card had an inner pedestal due to miscalibration adjustement which prevented a sensitivity of 2.048 ADC counts/mV.

Card Number	Digital Response [ADC counts/mV]
1	2.048
2	1.39

Table 5.3: Digital response of the two PCI-ADC cards used for the PETRA laser-wire.

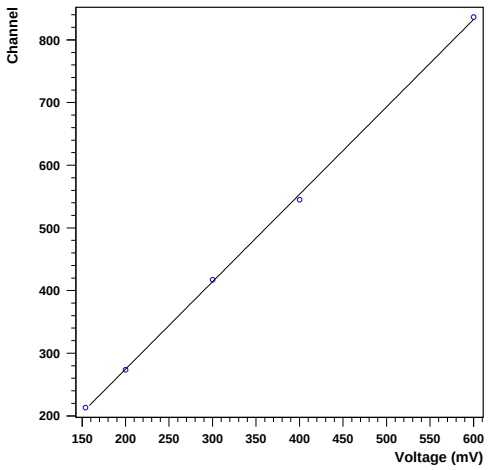

Figure 5.10: Digital response versus the input voltage of the PCI-ADC card used for the second calibration. The slope of the digital response function of the second card was found to be 1.39 ADC counts/mV.

5.4.3 Preliminary Studies

Prior to investigating the energy resolution of the final detector used at the laser-wire experiment, a number of preliminary studies described below were performed.

- Individual Crystals

  Ten crystals were individually tested with a 3 GeV electron beam in order to check their energy response and select appropriately the 9 crystals to be used in the final matrix. Each crystal was connected to a Hamamatsu R560 PMT. The measured voltage spectrum from the energy deposit of an incoming electron, as shown in Fig. 5.11 for crystal number 2, was fitted to a double gaussian to obtain the width of the peak and its mean. Fig. 5.12

displays the result of the peak width versus the peak mean voltage for each crystal. The results did not fail any crystal: all gave a similar energy response, with not more than 4% of difference for any crystal. A more detailed study is available in [7].

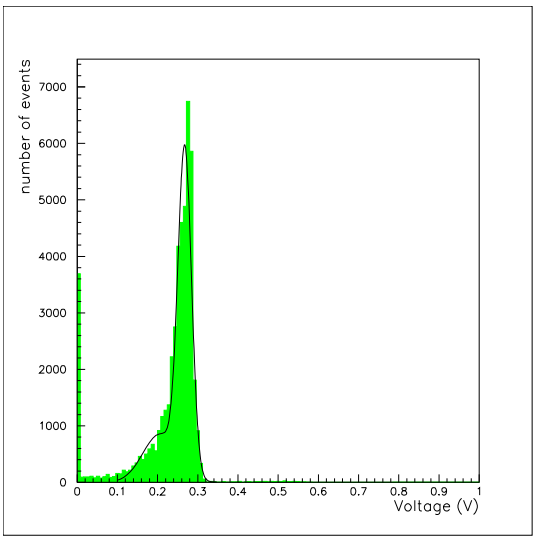

Figure 5.11: Voltage distribution for crystal number 2 and its double gaussian fit.

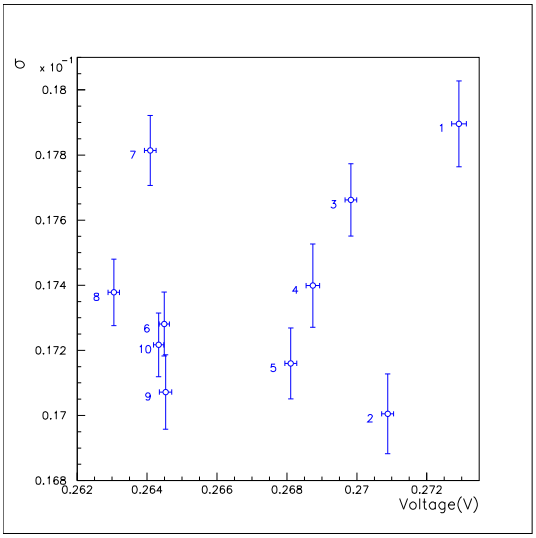

Figure 5.12: The peak width σ in volt versus the peak mean voltage for each crystal.

- Temperature studies

  $PbWO_4$ scintillators have a relatively high temperature dependence of light yield due mainly to strong thermal quenching [1]. The crystals' output variations with temperature were studied and their response to a fixed 2 GeV

electron beam was checked. Temperature measurements were performed with a linear PT100 sensor attached to the surface of the crystals. The box containing the crystals was first heated and maintained at a temperature of 24 ± 0.1^oC and then brought to the cooler test beam area, where the temperature was measured to be 18 ± 0.1^oC. The crystals and PMT were enclosed in protective foam within the light tight box which ensured a slow decrease of temperature and so maintained homogeneity of temperature throughout the detector. The detector response to temperature change is displayed in Fig. 5.13. The response data are well fitted by a quadratic function. The temperature coefficient defined as $\alpha[\%/^oC] = d_o/dT$ is calculated to be $-2.7\%/^o$C at 20^oC and decreases to $-1\%/^o$C at 22^oC. d_o corresponds to the difference in output for the temperature range dT. Thus, the higher temperature of the detector, the lower the temperature fluctuations affect the response. This effect has also been observed within the CMS lead tungstate study group where it was shown that, for the light yield, the absolute value of the temperature coefficient keeps decreasing up to 51^oC [6]. For the present calorimeter, it is assumed that the variation coefficient is below $1\%/^o$C for temperatures higher than 24^oC, which is roughly the temperature in the PETRA tunnel as discussed in Sec. 5.5.5. The results show as well that to gain in sensitivity (+10%) a cooling system would be necessary. However the detector response is already good enough for the purpose of the laser-wire experiment.

5.4.4 Performance

Tests were performed on the calorimeter prior to and after its use at PETRA. Both performances obtained at DESY II are presented below. The first tests were done before any installation at the PETRA beamline and were performed at 1145 V. The second detector tests were done after its use for the first laser scan with the same experimental conditions as used at PETRA i.e. with a calorimeter power supply of 2115 V. It was expected that a voltage supply of 1145 V would

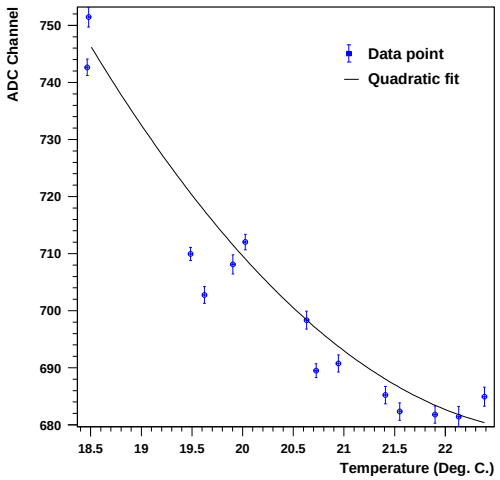

Figure 5.13: Response of the detector for temperature range from 24 to 18^{o}C.

be sufficient for the scan measurements at PETRA, thus the pre-installation test were performed at this voltage. However the amount of material in front of the detector and the degradation of its photocathode necessitated 2145 V of power supply to collect an adequate output signal. The amplitude of the analog signal was recorded at each bunch crossing to form a spectrum as shown in Fig. 5.14(a), together with its gaussian fit. Fig. 5.14(b) shows the results of the mean value as a function of the beam energy. The test points out that the energy leakage, if there is any, does not increase within the energy range studied and that the calorimeter is not saturating at 1145 V. However, the second test indicates at 2115 V that the signal versus the incoming energy is not any more linear for energies higher than 3 GeV. A linear fit according to $V[\text{Volt}] = a_v E[\text{GeV}] + b_v$ below 3 GeV for the second calibration and on the full range for the first calibration gives the results displayed in Tab. 5.4. The fit results suggest that the signal at 2115 V is ten times the signal at 1145 V, whereas from the standard gain curve (Fig. 5.5) it is expected to be approximately 160. In addition the second calibration illustrates that photons of energy at least 4.4 MeV are necessary to obtain a positive output voltage at the PMT. These results indicated a degradation of the calorimeter. The dismantling of the detector revealed a darkened photocathode window due to radiation damage.

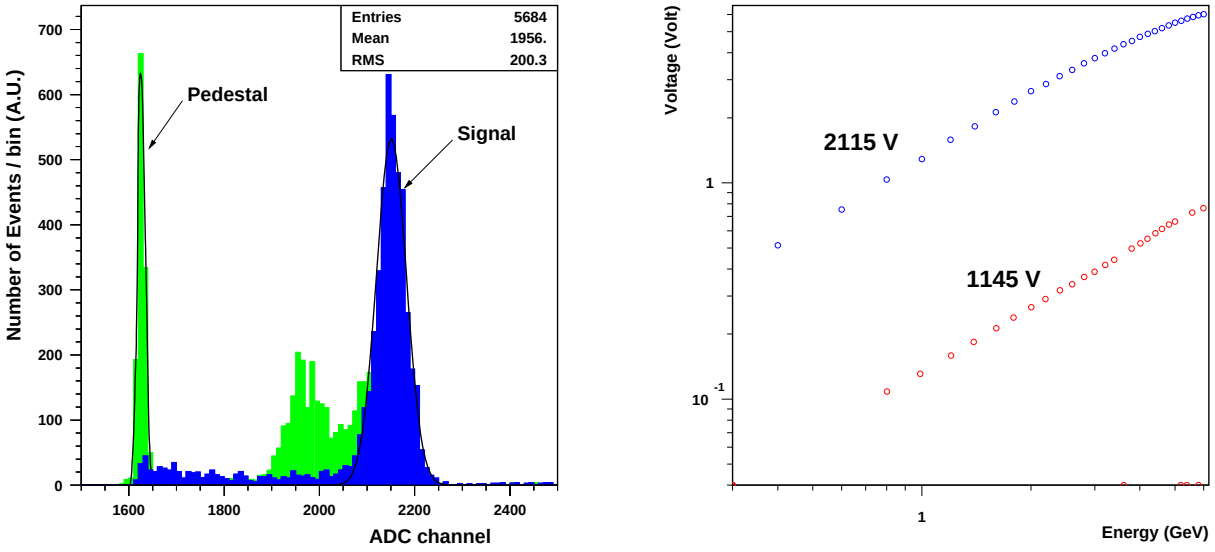

(a) Spectrum at 3 GeV with a gaussian fit.

(b) Voltage versus beam energy.

Figure 5.14: Typical signal and pedestal ADC spectrum at the beam test and calibration plot of voltage versus energy. The signal measurement is triggered by the scintillators coincidence and the pedestal measurement by random noise.

Test number	a_v	b_v $[10^{-3}]$
1	0.130 ± 0.01	0.0322 ± 0.003
2	1.324 ± 0.014	-5.59 ± 0.02

Table 5.4: Results of the linear fit of the Voltage [V] versus the beam Energy [GeV].

The experimental energy resolution of the matrix was measured and fit according to

$$\frac{\sigma_E}{E} = \sqrt{(\frac{c}{E})^2 + (\frac{a}{\sqrt{E}})^2 + b^2} \tag{5.9}$$

The resulting parameters are given in Tab. 5.5 and Fig. 5.15 shows the fit with c the instrumental error (noise and pedestal width), a the resolution due to statistical fluctuation in the PMT and crystals, and b the calibration and non-uniformities error. At 6 GeV, the energy resolution of the detector is approximately 5.4 % and at 0.8 GeV it is 14.5 % for PMT power supply of 1145 V. However at 2115 V, the electronics noise is increased and the resolution is 23 %

Power Supply [V]	1145		2115	
parameter	mean value	error	mean value	error
c (electronic)	0.102	0.006	0.177	0.003
a (stochastic)	0.067	0.003	0.0094	0.0002
b (uniformity)	0.034	0.002	0.0014	0.0003

Table 5.5: Fitting parameters for the energy resolution.

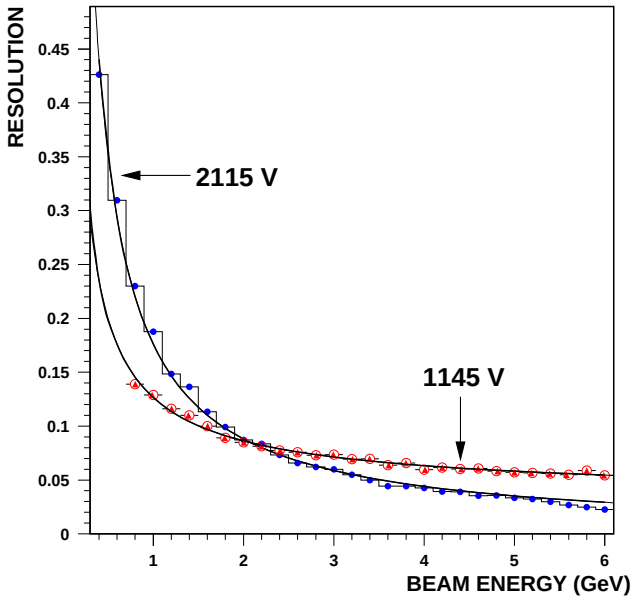

Figure 5.15: Energy resolution of a 3 by 3 matrix made of $18 \times 18 \times 150$ mm $PbWO_4$ crystals for PMT power supply of 1145 V and 2115 V.

at 0.8 GeV.

5.4.5 Geometrical Response of the Detector

The response of the detector to the relative position of the incoming electron beam was determined using a fixed beam energy of 3 GeV, the energy at which the flux of electrons from DESY II is a maximum. The table supporting the box was moved vertically. Between each set of measurements, the pedestal was measured. It was then subtracted from the signal. The pedestal varies by about

8 % over a few hours. One scan, at the horizontal centre of the matrix, is shown in Fig. 5.16 with the signal only. The horizontal lines are the boundaries of the crystals. It indicates a plateau for the middle crystal and shows as well the non uniform behaviour of the matrix response (combination of PMT, optical grease and crystal efficiency).

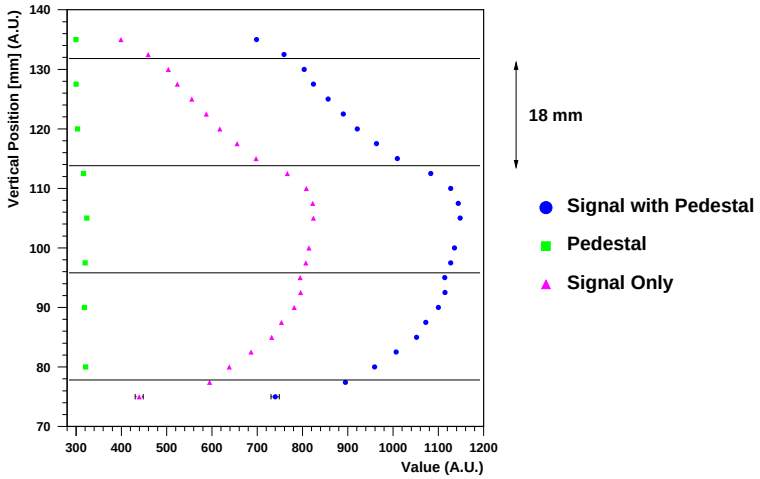

Figure 5.16: Signal and pedestal as a function of the vertical position of the matrix with respect to the beam axis. Horizontal lines correspond to the edges of the crystals.

The Compton signal in PETRA has a fan of $\frac{1}{\gamma_e}$ approximately [1] where γ_e stands for the Lorentz factor of the electron beam, neglecting the bunch angular phase space, so the region illuminated is approximately 0.025 mm^2 for an electron beam of 4.5 GeV. Taking into account 145 mm of aluminium thickness in front of the detector increases this region to 1 cm^2 15 m downstream. Measurements were thus concentrated in the region of the central crystal and a scan in $x - y$ was performed every 2. mm in contrast to the previous study where x was fixed and y was moved accross the whole matrix. The results are shown in Fig. 5.17. The crossing of a vertical and horizontal line correspond to a data point. The contours show the same level of detector response, interpolated from the data points.

A plateau is observed around a central area of 10 mm of diameter with the

[1] ϵ=0.04 is neglected in this approximation of the fan equation of Sec. 4.5.

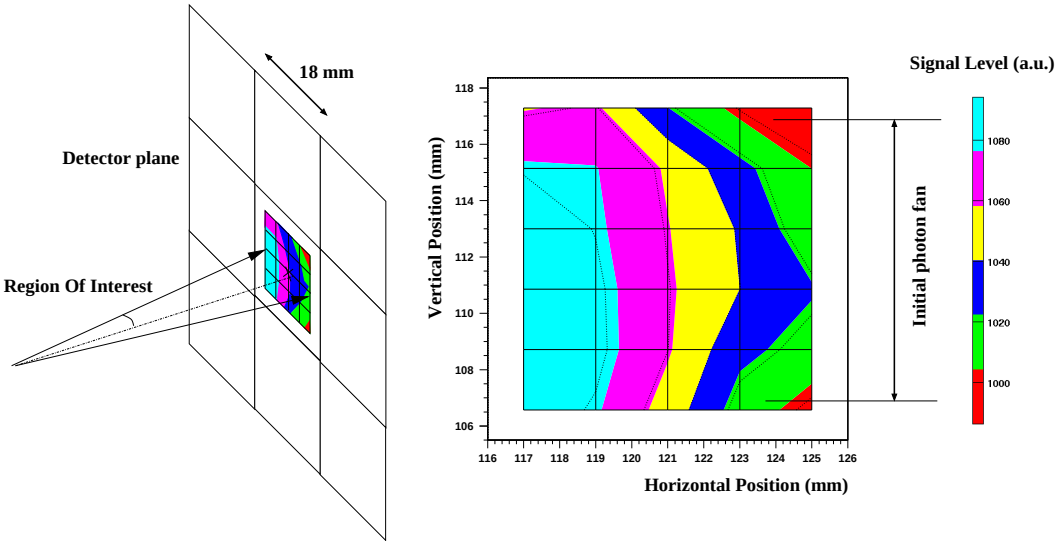

Figure 5.17: Mapping of the calorimeter in its central region.

signal varying not more than 10 %. The plot shows as well that the maximum response of the detector is slightly off centered by a few mm compared with the geometrical centre of the matrix.

5.5 Installation at PETRA

5.5.1 Overview

As described in Chap. 4.7, location 1 was chosen for the installation of the experiment. Thus the laser is installed approximately 15 m away in a laser hut outside the PETRA tunnel as displayed in Fig. 5.18. An access pipe connects the tunnel of PETRA and the laser hut where the laser system is based.

5.5.2 Laser

The laser used for the laser-wire experiment is a Quantel YG580 model Q-switched system, which provides short, high-energy pulses rather than continuous wave operation. The system is based on an Yttrium-Aluminum-Garnet crystal doped with Neodymium (Nd:YAG) amplifier originally used at CERN for the polarimeter at the LEP machine. It provides a green laser with wave-length 532

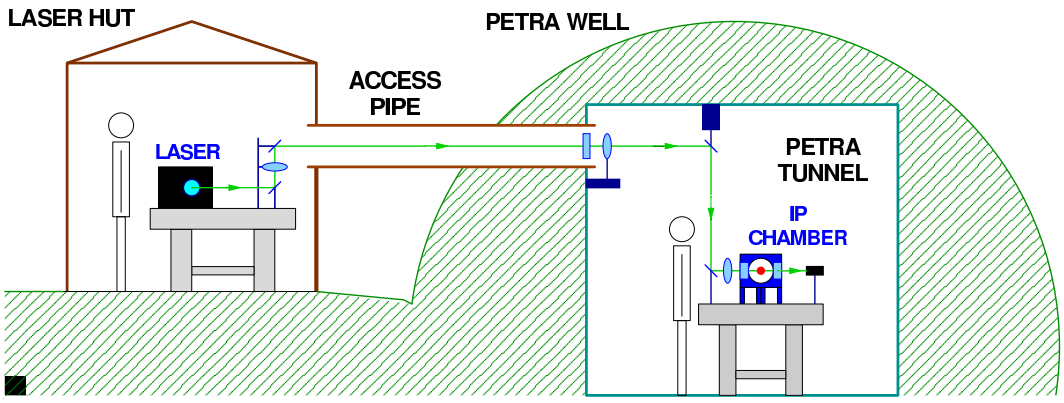

Figure 5.18: Schematic view of the beam laser path from the laser hut to the PETRA tunnel.

nm. Green light is chosen for this experiment because its shorter wave-length enables smaller spot sizes to be achieved, and it is easer to set up and manage than infra-red.

5.5.2.1 Laser Transport

The laser light is transported from the laser hut to the IP at PETRA through various optics as shown in Fig. 5.19. To reduce the systematics from the uncertainties in the laser beam spot size, the laser beam transverse size at the IP has to be reasonable (about a third) compared to the positron beam size it scans; the final spot size is determined by the focal length of the last lens, over the input beam radius. To provide the input beam with a known size at the last lens, a telescope made of two focusing lenses, 10 m apart, is used. Between the telescope and the last lens right in front of the viewport a mirror attached to a piezo electric tilting actuator is used to modify the direction of the photon beam and so adjust the relative position of the laser beam with respect to the positron beam. Its scan range is 0-2 mrad, and the actuator is at one end of its range when no voltage is applied. Fig. 5.20 shows the laser path in the hut and Fig. 5.21 displays the optics in the tunnel before the light reaches the IP chamber. On the other side of the viewport a Charged Coupled Device (CCD) camera is installed which is used to measure the photon beam size and position of the laser spot.

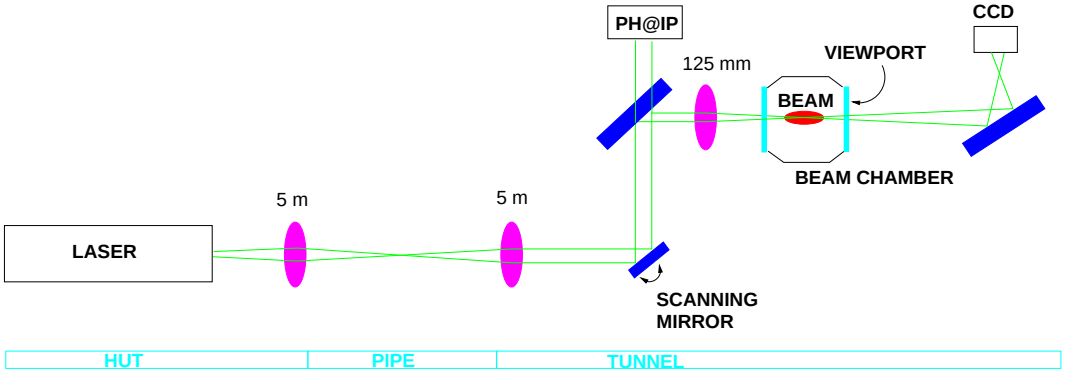

Figure 5.19: Layout of the optical path from the laser hut to the PETRA tunnel.

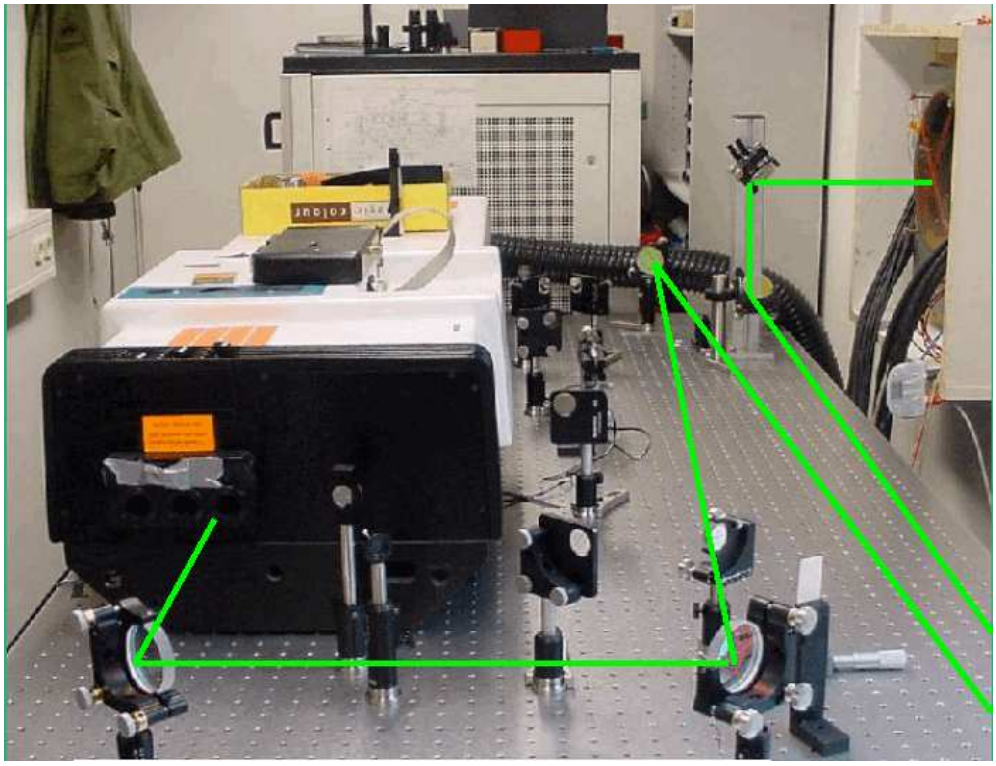

Figure 5.20: The light path in the hut transported from the laser to the access pipe of PETRA.

5.5.2.2 Parameters of the Laser

The longitudunal profile of the laser is measured using a streak camera with 5 ps time resolution. The data revealed a pulse length of Δt=12.5 ns full width at half maximum with a sub-structure of 70 ps peak to peak, shown in Fig. 5.22. This sub-structure is due to mode-beating of different longitudinal modes. It causes the Compton signal amplitude to vary between zero and full signal for

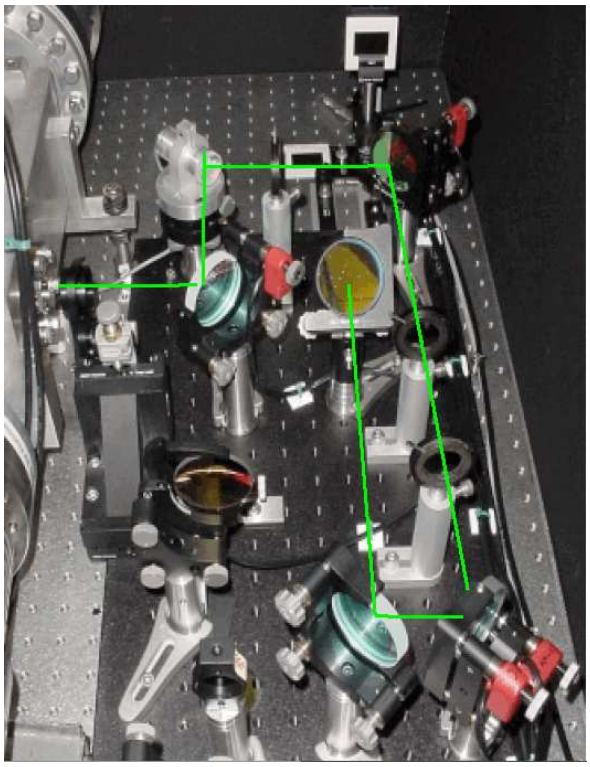

Figure 5.21: Close-up view of the laser path before the interaction chamber in the PETRA tunnel. The piezo actuator is the top left optical system.

different laser shots. The transverse size of the laser at the interaction point and

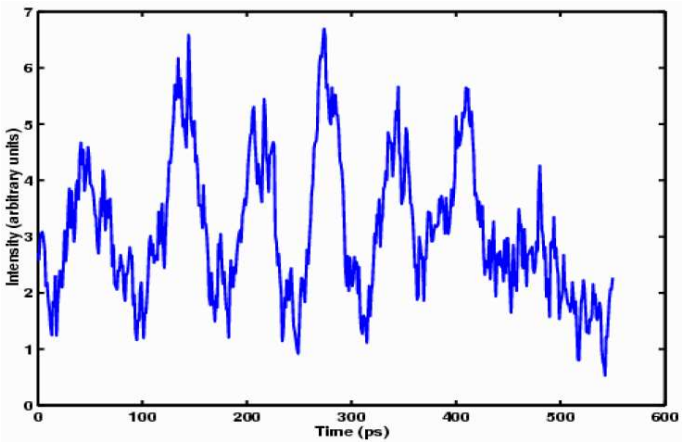

Figure 5.22: The laser longitudinal profile measured with a streak camera.

its position is needed as input in Eq. 4.4. A CCD camera located on a tracking rail is moved longitudinally through the waist of the laser and the beam size is measured at each point. A fit of the beam waist measurement as a function of the position z of the camera with respect to the distance to the final focus lens

can be performed with the following equation

$$\sigma = \sigma_0 \left[1 + \left(\frac{z}{z_R} \right)^2 \right]^{1/2} \tag{5.10}$$

where the Rayleigh range is $z_R = \frac{4\pi\sigma_0^2}{\lambda M^2}$, with λ the laser wave-length, M^2 the mode quality index which quantifies the difference between an actual beam and a Gaussian beam. The result of the fit gives a minimum waist of $\sigma_0 = 35 \pm 1$ μm with $M^2 = 7.6 \pm 0.4$ and a rayleigh range of 3807 μm.

To check the displacement of the laser spot at the interaction point, a beam splitter is interspaced between the piezo scanning mirror and the final focus lens and part of the laser beam is redirected through a lens, similar to the one at the final focus, and on to a CCD camera.

The laser spot position at the interaction point is modified for each step of the piezo-scanning mirror to which a specific voltage from 0 to 10 V is applied and amplified by a factor 10. The scanning step is 62.5 mm/V at the IP.

5.5.3 Signal Available

Various signals are available in the laser hut, which give a measurement of the crossing time of the laser and positron beam and their respective position; they also provide a trigger for both the laser and the data acquisition system as indicated in the signal path diagram of Fig. 5.23. The reference time is taken from the PIT (PETRA Integrated Time) signal and corresponds to the revolution clock of a bunch circulating within PETRA ($\sim$ 131 kHz). This reference time provides the trigger for a Versa Module Europa (VME) system which in turn sends the required signals to the laser for the beginning of its charge, the laser pumping action and the Q-switching which starts the release of the laser beam. The laser operates at a maximum frequency of 30 Hz, which is fixed by the VME system to occur between the PIT signal from a selected bunch (PITY) and the following PIT signal (PITE), delayed by 96 ns. A beam position monitor (BPM) stationed downstream and very close to the IP provides the positron beam position.

In addition, a photodiode with rise time of 1 ns is located close to the interaction point and serves as a trigger signal for the PCI-ADC card. The positive signal from the photodiode is thus amplified to 150 mV and then converted to a TTL signal usable by the PCI-ADC trigger.

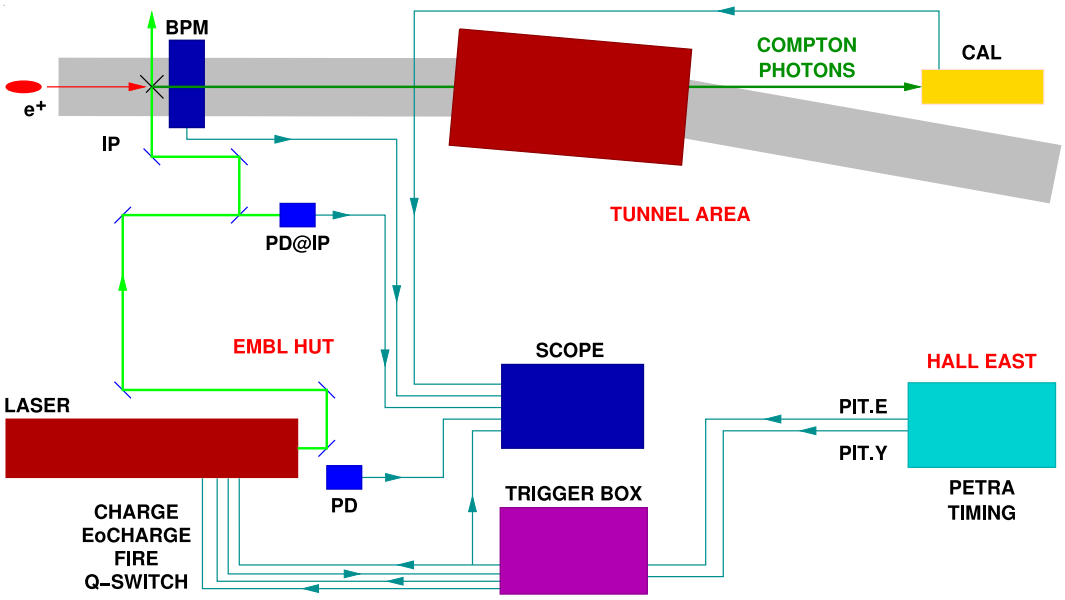

Figure 5.23: Path diagram for the various signals collected at the laser hut. The DAQ system replaces the oscilloscope.

5.5.4 Detector Installation Position

The Compton scattered photons travel in a straight line while the positrons are bent by a dipole. Thus the detector has to be positioned after the magnet, in the direction of the photons. The calorimeter is installed on a stand at the height of the centre of the beampipe, approximately 14.83 m away of the IP. The horizontal alignment of the calorimeter was performed using the position of the centre of the viewport and two quadrupoles surrounding the IP. The positron beam is not bent away by a quadrupole but only focused and goes through its center. Thus the quadrupoles can be used to geometrically define the position of the beam and the direction of the scattered Compton photons.

5.5.5 The PETRA Environment

- Temperature in PETRA

  Temperature measurements were performed over 10 days of PETRA running. The range of temperature at the detector location was measured to increase from 24 to 26^oC over 8 hours of running when only leptons are circulating. As seen earlier, this range of temperature, is expected to modify the detector response by less than 1%.

- Radiation

  Radiation measurements in the PETRA tunnel and at the location of the detector were performed. They show an unusually high radiation level at the detector location, of the order of 76 Gy, compared to other positions in the PETRA tunnel, of approximately 10 Gy. This radiation level is not foresseen to be problematic for the crystals of the calorimeter although it degrades the resolution of the detector mainly because the photocathode window of the PMT becomes brown, as described in Sec. 5.4.4.

- Beam Intensity

  The intensity of the beam is proportional to the number of positrons in a bunch. It decreases with time because of beam loses due to SR and bremsstrahlung as discussed in the previous chapter. It can be well fitted with a simple exponential evolving with time

$$I = \exp\left(A + Bt\right) \tag{5.11}$$

  where I is the intensity in mA and t is the time in hours and A and B, are the normalising parameters. The measured intensities during the measurements at PETRA are shown in Fig. 5.24 and the fitted values of A and B are given in Tab. 5.6.

	A	B
Low current	2.96 $\pm$0.01	-5.23 10^{-2} $\pm$0.01 10^{-2}
High current	4.87 $\pm$0.01	-6.02 10^{-2} $\pm$0.01 10^{-2}

Table 5.6: Fit parameters for the low and high current in PETRA positron beams.

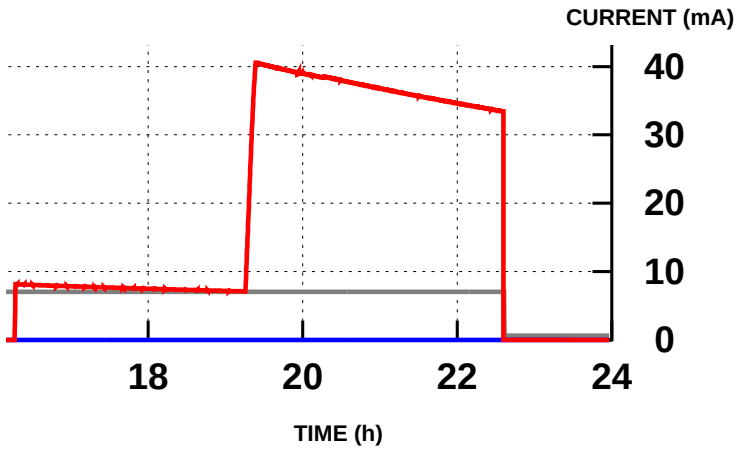

Figure 5.24: Positron current during the measurements at PETRA. Low current data taking started with current of 7.5 mA and the high current data taking started with 40.5 mA.

5.6 Finding the Signal

Due to differing beam orbits, the positron bunch can move by a few mm at the IP whereas the scanning range for the laser is limited to approximately 600 μm. The positron bunch must thus be steered with an orbit bump in order to intersect the laser beam and, once the signal is obtained on the detector, the PETRA orbit bump parameters are stored and the setting is fixed. Fig. 5.26 shows the oscilloscope display when the interaction occurs and when the laser is off (Fig. 5.25).

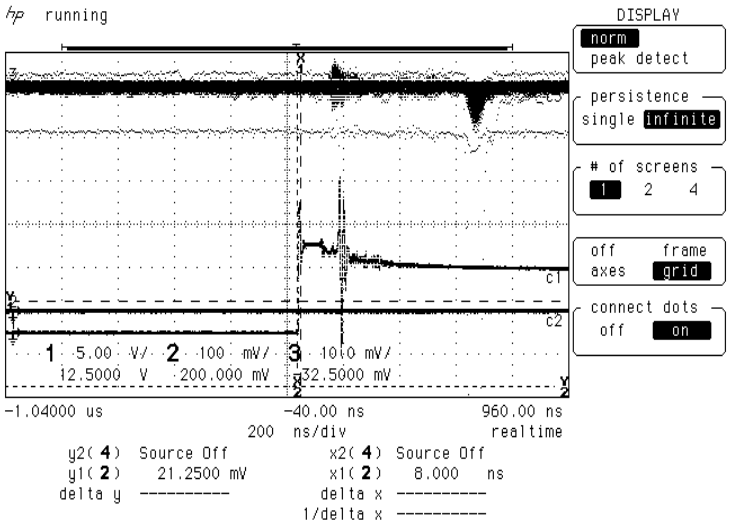

Figure 5.25: Display of the oscilloscope with the laser off with channel 1 (C1) the Q-switch, C2 the signal from the photodiode at the IP and C3 the calorimeter signal.

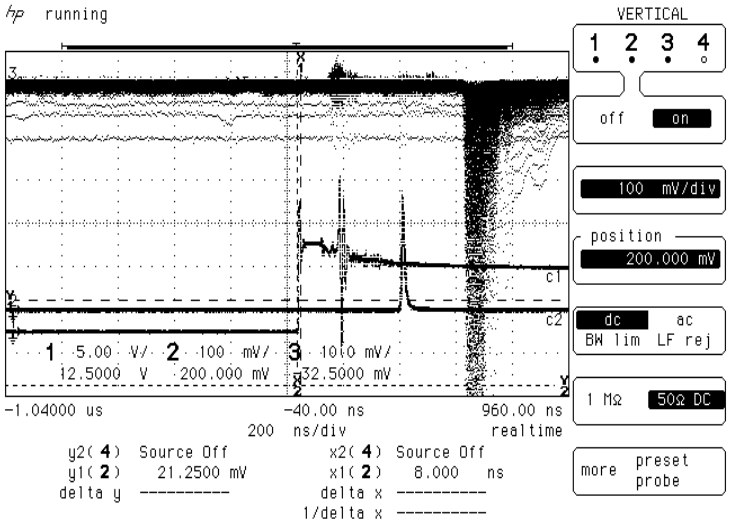

Figure 5.26: Display of the oscilloscope with the laser on with C1 the Q-switch, C2 the signal from the photodiode at the IP and C3 the calorimeter signal.

5.7 Scanning with the Laser - Results at PETRA

The positron orbit bump being fixed, the laser is then steered in 31.5 μm vertical steps at the IP by tilting the mirror attached to the piezo actuator. 20 scan points are taken, each at a different position and each with at least 5000 bunch crossings.

One scan point corresponds approximately to 3 minutes of measurements. The spectrum of the measurements is then recorded.

Full scan measurements were performed at PETRA for a 7 GeV positron beam, with two different currents as discussed in Sec. 5.5.5. Fig. 5.27 displays the raw ADC spectrum at each scan point for low current and Fig. 5.28 the spectrum for high current. They illustrate how the spectrum is modified with the scan position of the laser. A peak is observed in each plot corresponding to the pedestal, which is present even if no Compton photons reach the detector. As the laser is stepped across the positron bunch, the number of events with ADC count higher than the pedestal increases to a maximum and then decreases.

5.7.1 Preliminary Analysis

Preliminary studies on the scan results taken at each position of the piezo-driven laser scanner are detailed below. The study is first focused on the pedestal.

The pedestal occurs when the bunch crossing at the IP triggers the ADC reading and no energy is deposited in the crystals. Only the electronic noise is then recorded and appears as a gaussian distributed spectrum due to statistical fluctuations.

Fig. 5.29 displays the ADC count of the pedestal for a typical scan point versus the event number. By dividing each scan point into samples of 500 events, the mean value of the pedestal of the considered sample can be obtained from a gaussian fit to the peak. The pedestal was then substracted for each sample.

5.7.2 Energy Spectrum and Event Selection - Scan

The conversion of the spectrum from ADC counts to energy spectrum is performed using the second test beam calibration as discussed in Sec. 5.4.4 and corresponds to

$$E[\text{GeV}] = \frac{\text{ADC count} - b_c}{a_c} \tag{5.12}$$

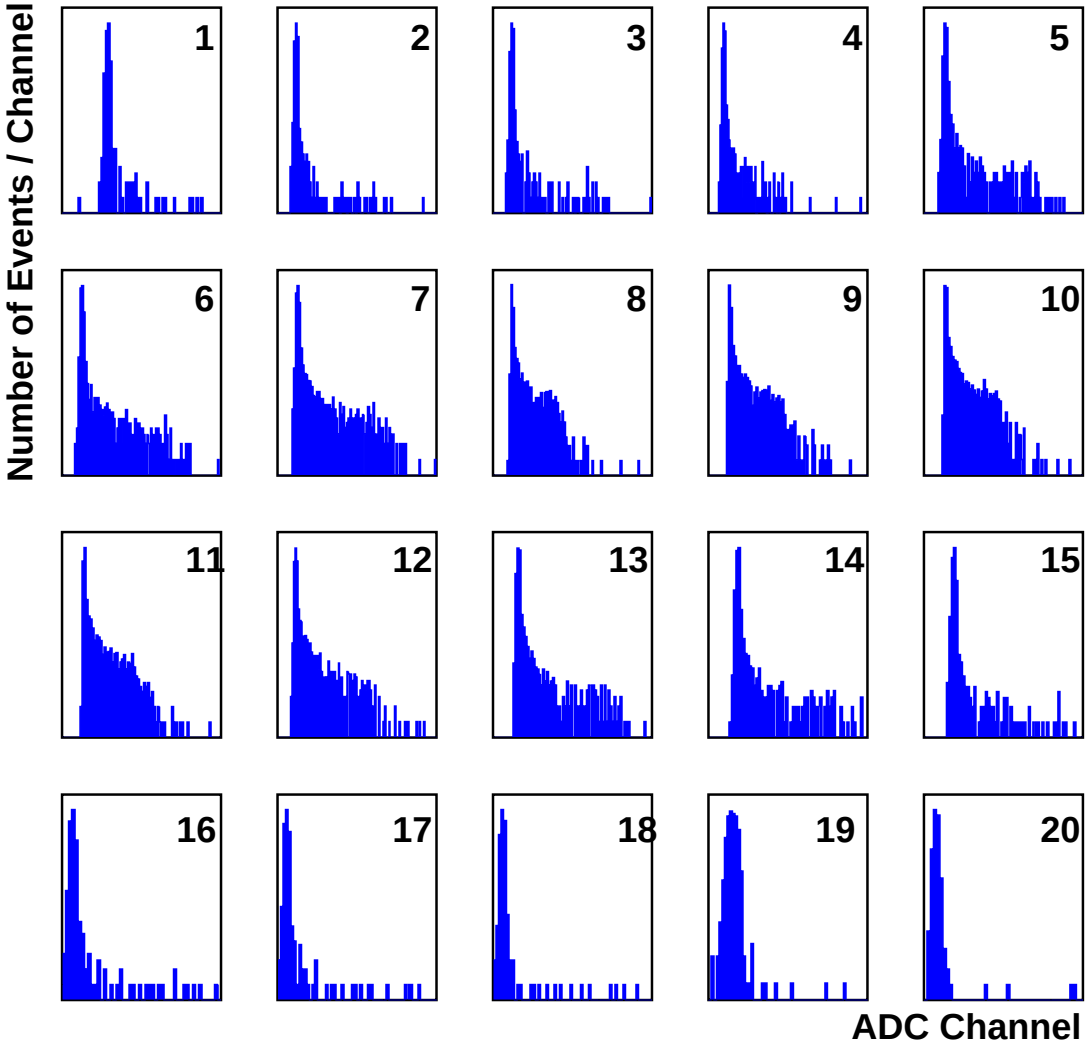

Figure 5.27: Raw spectrum for each scan point for low current positron beam.

with $b_c = b_v/R_c$, $a_c = a_v/R_c$ and the slope of the digital response function $R_c = 1.39\ 10^{-3}$ ADC count/V. Fig. 5.30 illustrates the result of the calibration applied to two typical spectrums for high and low current. A cut on the pedestal is applied at three sigma of the mean of its gaussian fit corresponding to 20 MeV approximately. All events with energies higher than the cut are accepted and added to form the signal amplitude.

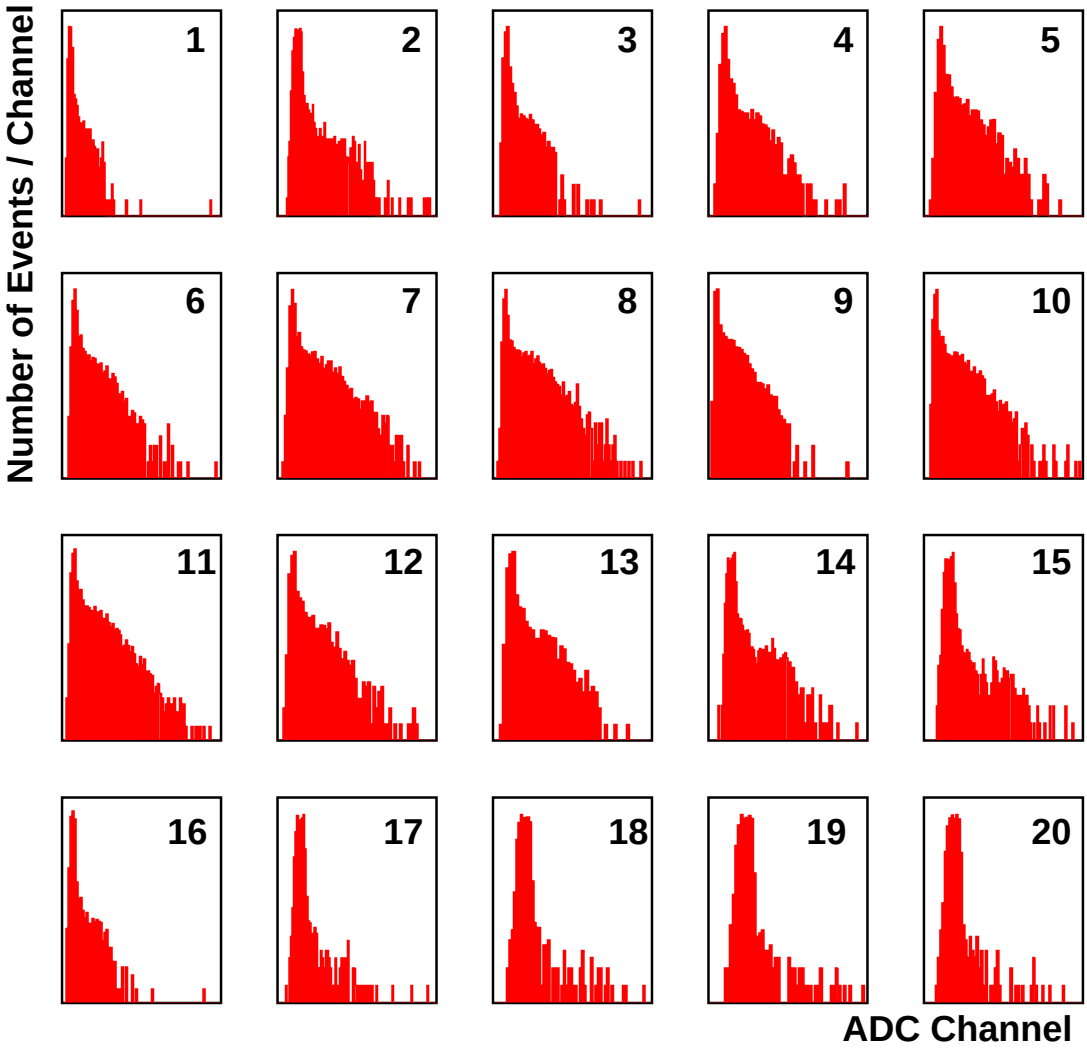

Figure 5.28: Raw spectrum for each scan point for high current positron beam.

5.8 Analysis

As discussed in Sec. 4.4, the amplitude of the signal versus the relative position of both beam forms a gaussian. The fit has to take into account the decrease of the number of electrons in the bunch due to beam lifetime, which follows an exponential slope as discussed in Sec. 5.5.5. The fit using a gaussian function added to an exponential is given in Tab. 5.7. The positron bunch vertical size can hence be calculated using $\sigma_{e_y} = \sqrt{\sigma_{fit}^2 - \sigma_{laser}^2}$ with $\sigma_{laser} = 35$ μm.

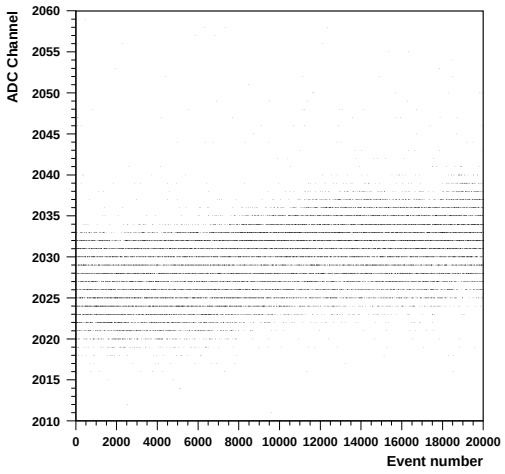

Figure 5.29: Example of ADC counts pedestal shift.

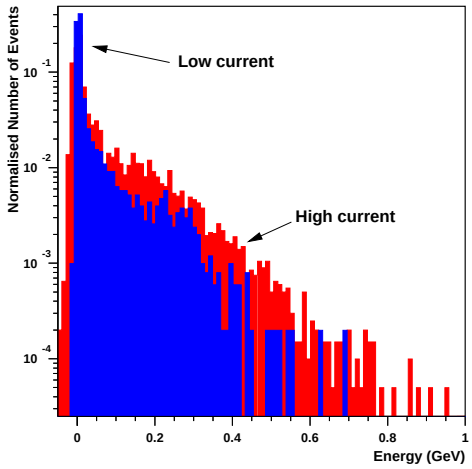

Figure 5.30: Signal spectrum at PETRA for high and low current.

Thus, the overall measurements are for high current

$$\sigma_{e_y} = 88.4 \ \pm 3.3 \ \pm 16. \ \mu m \tag{5.13}$$

And for low current

$$\sigma_{e_y} = 65.3 \ \pm 1.9 \ \pm 16. \ \mu m \tag{5.14}$$

where the first error is derived from the propagation of the errors on the laser beam size and the second is systematic error arising from the piezo attenuator position errors. Fig. 5.31 for the low current and Fig. 5.32 for the high current display the results of the fit. Each dot corresponds to the mean of ten samples

Current	χ^2	$\sigma_{fit}[\mu\text{m}]$	$\Delta\sigma_{fit}$	σ_{e_y}	$\Delta\sigma_{e_y}$
high	0.51	95.1	2.3	88.4	3.3
low	0.72	74.1	1.6	65.3	1.9.

Table 5.7: Fit result for low and high current.

and the mean errors ΔN_m calculated with

$$\Delta N_m = \frac{\sigma_{N_k}}{\sqrt{nb_s}} = \frac{1}{\sqrt{nb_s}} \sqrt{\sum_{k=1}^{nb_s} \frac{(N_k - N_m)^2}{nb_s - 1}} \tag{5.15}$$

with nb_s the total number of samples, the entry N_k for each sample and N_m the mean over the samples at a scan point.

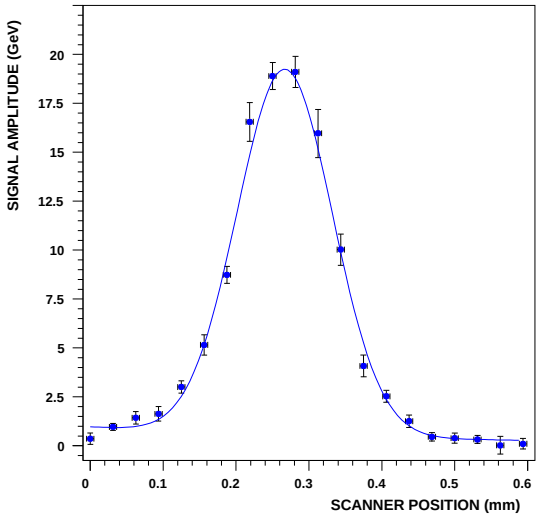

Figure 5.31: The pedestal subtracted signal as a function of scan position for the low current beam.

5.8.1 PETRA Optics

The beam size can be calculated from machine optics considerations using the known beam emittance and betatron function close to the location of the laser-wire IP as $\sigma_{e_y} = \sqrt{\epsilon_y \beta_y}$. The calculation gives a beam size of 96 μm with the emittance $\epsilon_y = 0.46$ nm rad and betatron function $\beta_y = 20$ m which is comparable to the measured beam size obtained with the laser-wire. A possible explanation

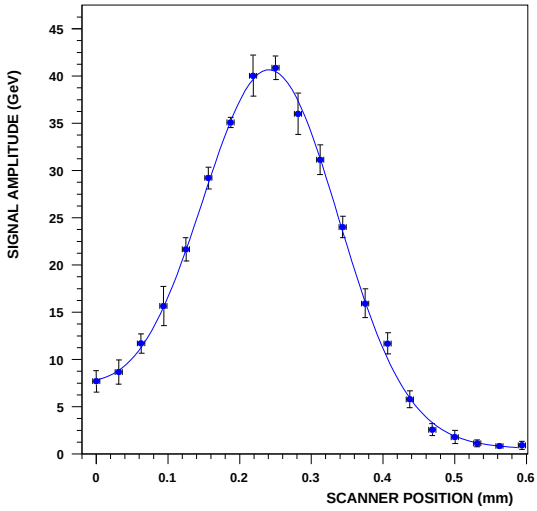

Figure 5.32: The pedestal subtracted signal as a function of scan position for the high current beam.

of the difference of the measurements between low and high current would be the fact that a dispersion effect, proportional to the momentum spread, would be greater when using the high current beam [10]. The momentum spread at higher current would be increased to $\frac{\Delta p}{p} = 10^{-3}$ and the transverse beam size would be

$$\sigma = \sqrt{\epsilon\beta_y + \left(\frac{D\Delta p}{p}\right)^2} \tag{5.16}$$

where D is the momentum dispersion function defined by the dipoles and quadrupoles and is equal to 50 mm. The beam size would then increase by 50 μm in quadrature, leading to a positron beam size of 108 μm.

5.9 Conclusion

A study of the PETRA laser-wire lead-tungstate crystal detector was performed, including a full beam test and measurements of its temperature dependance and geometrical response. In particular a calibration of its energy response was performed. The first scans of the positron beam at PETRA with a laser-wire, were carried out and measurements of the transverse size of the PETRA positron bunch taken for the first time by this technique.

Bibliography

[1] A. A. Annenkov, M. V. Korzhik and P. Lecoq, "Lead Tungstate Scintillation Material," Nucl. Instrum. Meth. A **490** (2002) 30.

[2] A. Annenkov, V. Ligun, E. Auffray, P. Lecoq, A. Borisevich and M. Korzhik, "Suppression Of The Radiation Damage In Lead Tungstate Scintillation Crystal," Nucl. Instrum. Meth. A **426** (1999) 486.

[3] X. D. Qu, L. Y. Zhang and R. Y. Zhu, "Radiation Induced Color Centers And Light Monitoring For Lead Tungstate Crystals," IEEE Trans. Nucl. Sci. **47** (2000) 1741.

[4] S. Agostinelli *et al.* [GEANT4 Collaboration], "GEANT4: A simulation toolkit," Nucl. Instrum. Meth. A **506** (2003) 250.

[5] S. O. Flyckt and C. Marmonier (Eds.). (2002) *"Photomultiplier Tubes - Principles and Applications,"* Brive, France.

[6] "CMS: The electromagnetic calorimeter. Technical design report," CERN-LHCC-97-33

[7] A. Muir, "Study of $PbWO_4$ crystals for use in the laser-wire electromagnetic calorimeter," MSc thesis, Royal Holloway University of London (2001).

[8] I. Dafinei *et al.*, "Lead Tungstate for High Energy Calorimetery," CMS TN/93-317, Ap. 1994

[9] `http://desyntwww.desy.de/~testbeam`

[10] K. Balewski, Private communication, February 5, 2005

Chapter 6

Fast Luminosity Spectrum Measurement at the ILC

For high energy physics, key accelerator parameters are the centre of mass energy and the luminosity. Reaching the highest centre of mass energy is important as it sets the mass scale at which particles can be created. This plays an important role when searching for new discoveries. But studying particles can only be possible if a large number of these are created, and for this a high luminosity is required. In view of the physics needs discussed in Chap. 1, it is crucial to obtain precise measurements of both the luminosity and the luminosity spectrum, the differential luminosity with respect to the effective centre-of-mass energy. The aim in the present chapter is to provide a fast measurement of the luminosity spectrum using data accumulated within a few hours for the purpose of machine tuning. This implies the need to use a large cross-section physics process such as Bhabha scattering and a method called unfolding.

6.1 Definition of Luminosity

Luminosity for collider experiments is defined by

$$\mathcal{L} = \frac{f_c N_b^2}{A} \tag{6.1}$$

where f_c is the mean bunch frequency, N_b is the number of particles per bunch, assumed here to be equal in both beams, and A is the effective overall area of collision at the interaction point. In other words, the higher the frequency, and the more particles there are for a given area, the higher is the luminosity.

The luminosity corresponds to the constant relating the event rate to the cross-section of a particular process as shown in the equation below

$$\frac{dN}{dt} = \mathcal{L} \times \sigma \tag{6.2}$$

By integrating over time, the luminosity gives the number of events created for a given process. Thus it is usually a very big value and is expressed in terms of barns or in cm^{-2}.[1] For TESLA, the designed instantaneous luminosity is $3.4\ 10^{34}\ \text{cm}^{-2}\text{s}^{-1}$. In practice, experimental cross-sections are calculated by using the inverse of the previous equation and integrating over time

$$\sigma = \frac{1}{L} \times N \tag{6.3}$$

The luminosity of a collider depends strongly on machine parameters as described in section 4.1. The corresponding uncertainties are unsatisfactory compared to the high experimental accuracy required. The luminosity is thus monitored by adopting a different strategy using the relation

$$L = \frac{1}{\sigma_{known}} \times N \tag{6.4}$$

where the cross-section σ_{known} can be computed to an extremely high theoretical accuracy at a given centre of mass energy. The luminosity is then used to obtain the experimental cross-section of other processes. The determination of the luminosity is thus an essential point. The process used to determine the luminosity at the ILC in the following section is Bhabha scattering $e^+e^- \rightarrow e^+e^-$ at small angle and is presented below in sec 6.3. However the cross-section is dependent on which centre of mass energy ($\sqrt{s}$) the process occurs and a careful study of the $\sqrt{s}$ distribution has to be performed. It is discussed in the next section.

[1] 1 barn=10^{-24} cm^{-2}

6.2 Centre of Mass Energy Distribution

The centre of mass energy *sqrts* is the addition of the energy of the two incoming particles (E_1 and E_2) which collide. A smearing of the centre of mass energy can occur via various processes outlined below:

1. Beam energy spread, which is machine dependent. It is usually very low as discussed in Sec. 6.2.1,

2. Beamstrahlung. When the beams collide, beam beam effects cause the production of beamstrahlung. This radiation degrades in a non negligible way the nominal centre of mass energy $\sqrt{s_0}$.

The various contributions to the electron energy distribution are displayed in Fig 6.1, including the contribution of QED processes only. It is similar for positrons but with a smaller beam energy spread.

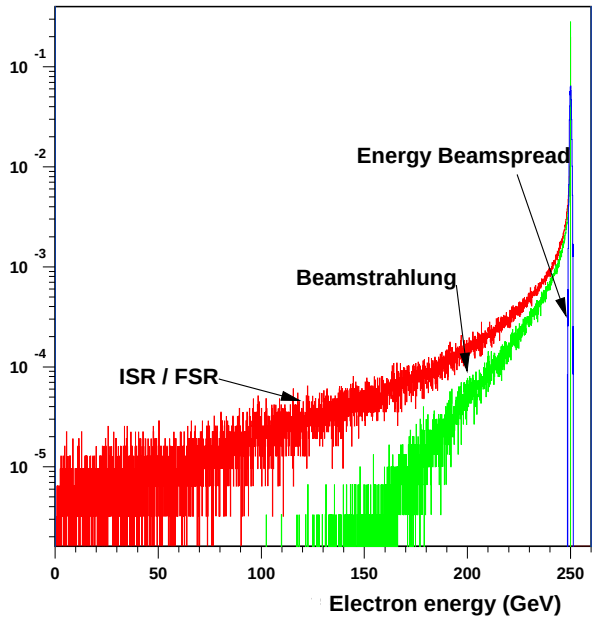

Figure 6.1: Contributions to the electron energy distribution: QED processes including ISR, beamstrahlung and beam energy spread.

6.2.1 Beam Energy Spread

The relative beam energy spread before collision is normally a small fraction of a percent and is much smaller than the effect of beamstrahlung. Nonetheless it has to be taken into account as it modifies the centre of mass energy before the interaction takes place. Beam dynamics simulations and analytical calculation can be used to estimate the beam energy spread.

The initial relative beam energy spread, of 0.03%, is mostly due to the bunch compressor at 4.6 GeV, before the main linac, and becomes 0.055% when accelerated to 250 GeV. Within the linac the main contribution inducing an energy spread is the wakefield effect: a bunch of particles, traveling through a structure with a transverse axis offset with respect to the structure axis induces electromagnetic fields that act back on the beam. In the so called short-range wakefield, the electromagnetic fields from the head of the bunch deflect the tail of the bunch whereas long-range wakefields are created by earlier bunches deflecting the later ones. The transverse wakefield is given by [3]:

$$W_T = \frac{2\sqrt{2}Z_0 c}{a^3 \pi}\sqrt{gs} \tag{6.5}$$

where a is the hole aperture in the structure which scales in practice as the inverse of the RF-frequency, s is the longitudinal position in the structure, g the length of the cavity gap and Z_0 is the transverse impedance. Thus the wakefields, being proportional to the (RF-frequency)^3 of the accelerator, can be kept low by choosing a low frequency.

For the electrons, a supplementary beam energy spread within a bunch comes mainly from the undulator located upstream of the interaction point. The undulator causes the electron beam energy to increase from 0.055% to 0.15%. For the positrons the main origin of beam energy dilution is from the Positron Pre-Accelerator (PPA) whose purpose is to provide a maximum capture efficiency of the emerging positron beam from the target behind the undulator [17].

The overall intra-bunch beam energy spread is outlined in Tab 6.1 for both centre of mass energies 500 GeV and 800 GeV. It is approximately two times

Centre of mass energy [GeV]	Energy spread $\frac{\sigma_E}{E}$ [%]	
	positron	electron
500	0.07	0.15
800	0.07	0.15

Table 6.1: TESLA energy spread for the electron and positron beams at 500 GeV and 800 GeV [6]. Electrons have a larger energy spread after passing through the positron source wiggler.

higher for electrons than for positrons. Fig. 6.2 displays the respective electron and positron pre-collision energy beam spread for TESLA - 500 GeV as obtained by Matliar fortran package [8] to simulate the beam transport from the gun to the interaction point. The spread can be fitted for the cold technology choice such as TESLA with a gaussian.

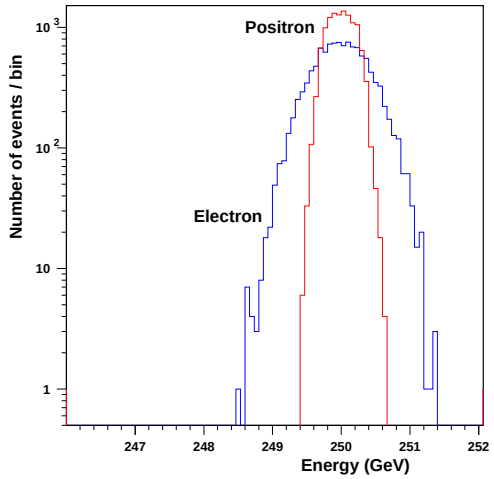

Figure 6.2: Beam energy spread of electron and positron as obtained with Matliar (File courtesy of Timothy Barklow - SLAC).

6.2.2 Beamstrahlung

For the required size of the beams, electrons and positrons within opposite beams may lose their energy via the beamstrahlung processes. Beamstrahlung is a type

of electromagnetic radiation emitted by a particle of the first beam deflected by the collective field of the particles of the second beam as displayed in Fig 6.3. The electron loses part of its energy before collision. As a consequence the centre of mass energy can not be assumed monochromatic. This leads to the energy spectrum shown in Fig 6.1 with a tail at low energy.

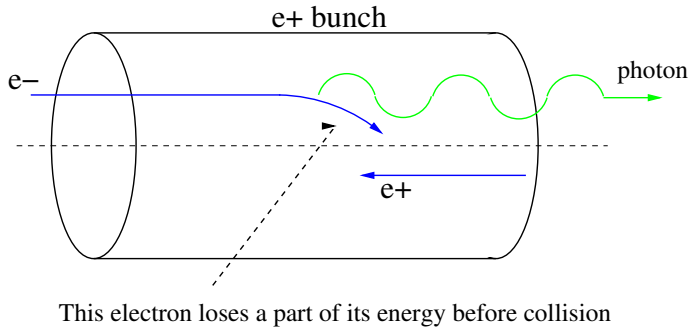

Figure 6.3: Schematic process of beamstrahlung.

The Lorentz invariant dimensionless parameter Υ is used to compute the beamstrahlung. It gives a measure of the field strength in the electron's rest frame.

$$\Upsilon = \frac{e\hbar}{m_e^2 c^4}(p_\mu F^{\mu\lambda} p^\nu F_{\lambda\nu})^{1/2} \tag{6.6}$$

where p_μ is the four momentum of the particle and $F_{\nu\mu}$ is the mean energy momentum stress tensor of the beam field. For a beam with a gaussian charge distribution the average value of the Υ parameter can be expressed using the following equation

$$< \Upsilon >= \frac{5}{6}\frac{N_e r_e^2 \gamma_e}{\alpha(\sigma_x^* + \sigma_y^*)\sigma_z^*} \tag{6.7}$$

with r_e the classical electron radius, γ_e the Lorentz factor E_{beam}/m_e, N_e the number of particles per bunch and σ_x^*, σ_y^*, σ_z^* respectively the horizontal, vertical and longitudinal beam size at the IP. They are given in Tab. 3.1 and lead to Υ=0.035 for a TESLA case at 500 GeV and Υ=0.084 at 800 GeV.

The maximum beam field corresponds to a maximum Υ_{max}, which is related to the mean value by

$$\Upsilon_{max} = \frac{12}{5} < \Upsilon > \tag{6.8}$$

In principle, all beamstrahlung effects should be calculated locally, and integrated

over the beam cross-section. However, the global beamstrahlung parameter as given in Equ. 6.6 is often adequate [13].

An important physical parameter is the average fractional beam energy loss from beamstrahlung and is given approximately [14] by

$$\delta_{BS} \approx 0.86 \frac{r_e^3 N_e^2 \gamma_e}{\sigma_z (\sigma_x^* + \sigma_y^*)^2} \tag{6.9}$$

Thus the energy loss δ_{BS} is fixed by the geometry of the beams and choosing a $\sigma_x^* \gg \sigma_y^*$ gives a δ_{BS} which is independent of the vertical beam size. δ_{BS} is 3.2% for the 500 GeV machine. Simultaneously, the luminosity can be increased by making σ_y^* as small as possible.

6.2.3 Beamstrahlung Generation

The simulation code Guinea-Pig [9] computes the beam fields according to accelerator specifications and simulates various processes such as beamstrahlung and pair creation, but it requires too much computer time and memory for direct use in physics generators. CIRCE-1.0 [11] is the basic package used to generate beamstrahlung for physics analyses. It provides a parameterisation of Guinea-Pig results and it is thus much faster. CIRCE parameterises the $e^{\pm}$ energy probability distribution $D_{e^{\pm}}$ according to the following equation

$$D_{e^{\pm}} = a_0 \delta(1-x) + a_1 x^{a_2} (1-x)^{a_3} \tag{6.10}$$

where a_1 is a normalising parameter and the three other a_k parameters define the distribution. The distribution is normalised such that the integral is equal to 1. CIRCE provides the set of parameters a_k, given as input the accelerator type and revision date. In the following, the version 7 of TESLA with the revision number $2000-04-26$ is used and corresponds to the machine parameter given in Tab 3.1. CIRCE computes, for the electron and positron, a fraction $x_{e^{\pm}}$ of their nominal energy which is 250 GeV for TESLA-500 GeV case. The energy distribution obtained for three nominal centre of mass energies of the TESLA design is shown in Fig. 6.4. For the statistics used here, it shows that the beamstrahlung tail ceases at a different level for each centre of mass energy and, for $\sqrt{s_0}$=500 GeV,

a_0	0.51288
a_2	9.9716
a_3	-0.62850

Table 6.2: Initial a_k beamstrahlung parameters for TESLA at a centre of mass of 500 GeV.

it ends at approximately 59% of $\sqrt{s_0}$. A modification of the initial parameters

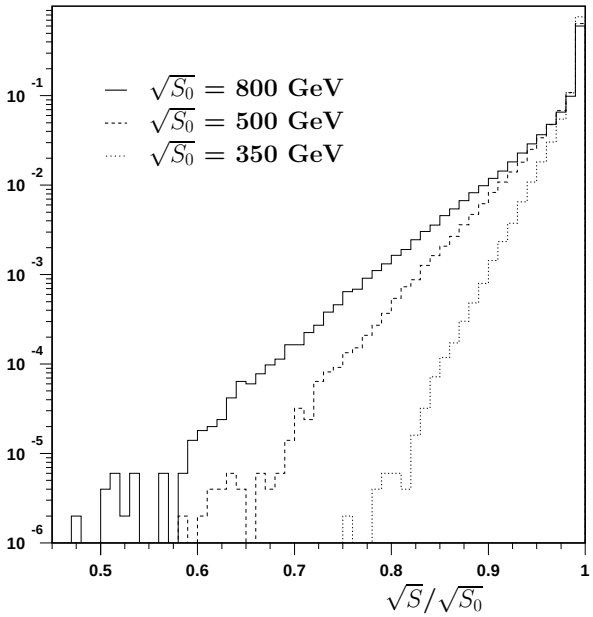

Figure 6.4: Probability density function of $\sqrt{s}/\sqrt{s_0}$ with beamstrahlung only for various nominal centre of mass energies, as provided by beamstrahlung generator (CIRCE).

for a selected accelerator, as given in Tab. 6.2 for TESLA with a centre of mass of 500 GeV, leads to the energy distribution displayed in Fig. 6.5. It displays the variation of the spectrum for a shift of 20% from the initial parameters a_0, a_2, a_3 and illustrates that the major spectrum modifications occur at high energy. Each parameters are modified separately.

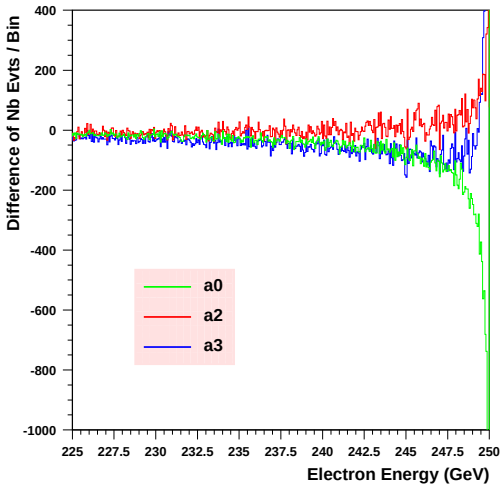

Figure 6.5: Difference in the energy distribution for parameters shifted separately by 20% from the initial TESLA 500 GeV CIRCE parameters a_0, a_2 and a_3.

6.3 Bhabha Scattering

The main reasons why Bhabha scattering at small angle is used to determine the luminosity are as follows:

1. The Bhabha scattering is a QED process which can easily be calculated to high precision including several order loops. It is foreseen that a theoretical precision on the Bhabha cross-section of 2 10^{-4} will be reached for the ILC.

2. The cross-section is large and its differential cross-section increases at small scattering angles (Fig. 6.6). Thus the statistical error on the number of events detected is low.

3. The detection of the final state can be performed via relatively simple systems such as calorimetry, described in Chap. 3.

6.3.1 Theory

Bhabha scattering is the name of the process leading to an electron-positron pair via the interaction of another such pair. Its cross-section was first calculated in

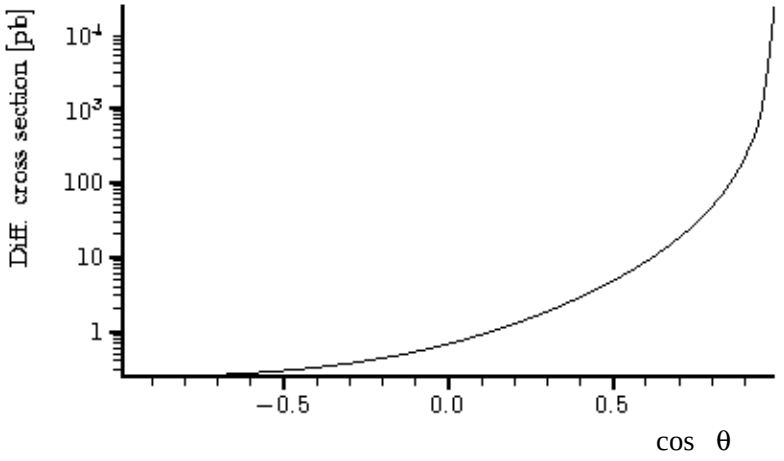

Figure 6.6: Differential tree level Bhabha cross-section at 500 GeV as a function of the angle as calculated with the CompHep-33 package [4].

1935 by H.J.Bhabha [1], and the tree-level scattering can be described by the Feynman diagrams of Fig. 6.7

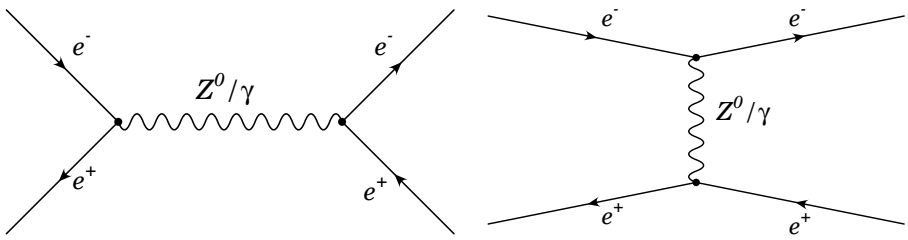

(a) s-channel (b) t-channel

Figure 6.7: Tree-level Bhabha Feynman diagram.

The diagram of Fig.6.7(a) with the annihilation of the electron-positron pair and creation of a new one via photon or Z-boson are called the s-channel and the diagram of Fig.6.7(b) with the exchange of a photon or a Z-boson are called the t-channel. At low angle the Bhabha scattering is dominated by the t-channel exchange process.

The differential cross-section with one photon exchange (t-channel) for unpo-

larised beams in the centre of mass energy is:

$$\frac{d\sigma}{d\Omega}(e^+e^- \to e^+e^-) = \frac{\alpha^2}{4s}\frac{2}{(1-\cos\theta)^2}[4+(1+\cos\theta)^2] \tag{6.11}$$

with $\sqrt{s} = \sqrt{(p_1+p_2)^2}$ the total centre of mass energy and here $s = 4E^2$, E the energy of the incoming colliding particles [2] θ the electron scattering angle and α the QED coupling constant.

The calculation of the cross-section would be incomplete if we were to take only the tree-level diagram; the calculation of the cross-section used below takes into account higher order diagrams.

6.3.2 Total Cross-section

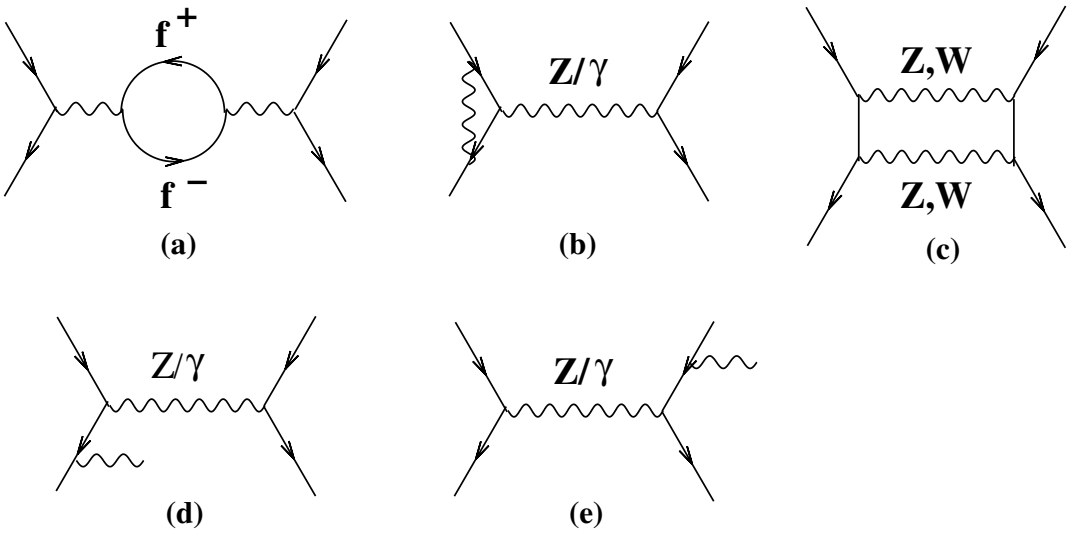

Figure 6.8: Radiative corrections to the Bhabha process: (a) one-loop fermionic correction, (b) one-loop vertex correction and (c) one-loop box correction whereas (d) and (e) are respectively ISR and FSR.

In the calculation of the cross-section used in Eq.6.4 one has to take into account the radiative corrections (Fig.6.8) and initial state radiation (ISR), in order to minimise the theoretical error. Various study groups are implementing tools to provide such calculations to a given order. A Monte Carlo event generator for Bhabha scattering (Bhwide [5]) has been used for this purpose .

[2] E is assumed equal for both particles here

It includes multi-photon radiation in the framework of Yennie-Frautschi-Suura (YFS) exponentiation, a technique for summing up all the infra-red singularities caused by soft photon radiations accompanying any given process [7]. Its matrix element describing the cross-section includes the complete result at $\mathcal{O}(\alpha)$ and leading logarithmic $\mathcal{O}(\alpha^n L^n)$ corrections in the series as well as some non-leading $\mathcal{O}(\alpha^n L^{n-1})$ corrections.

Bhwide 1.04 was used to calculate the cross-section at various energies including the effect of the corrections for the final state particle angle between 23 and 85 mrad, as shown in Fig.6.9. In order to interpolate the cross-section for any particular $\sqrt{s}$ value, a fit of the cross-section as a function of the centre of mass energy is performed with the functional form $\frac{a}{\sqrt{s}^b}$ where a is a normalisation parameter and b corresponds to how well the curve follows the proportionality to $1/s$. The theory uncertainties on the cross-section are 0.11% approximately for $\sqrt{s}$ ranging from 300 to 500 GeV. The parameter b is found to be $1.98500(\pm 3.3\ 10^{-5})$. In addition to ISR which degrades the effective centre of mass energy, the other processes described in sec. 6.2 can occur and also results in a reduction of $\sqrt{s}$. The cross-section fit function will be used to reweight the events to take account of these additional processes.

6.4 Backgrounds

Possible backgrounds that could lead to similar energy deposits into the calorimeter are now reviewed. These backgrounds were not included in the following section but their contribution to the signal in the acceptance of the luminosity detector is expected to be small. A dedicated selection could be used to further suppress these backgrounds, which can be distinguished as coming from beamstrahlung or physics processes.

From the beamstrahlung: photons, electrons and positrons can be created via several processes.

- Real photons emanating directly from the beamstrahlung have a very small

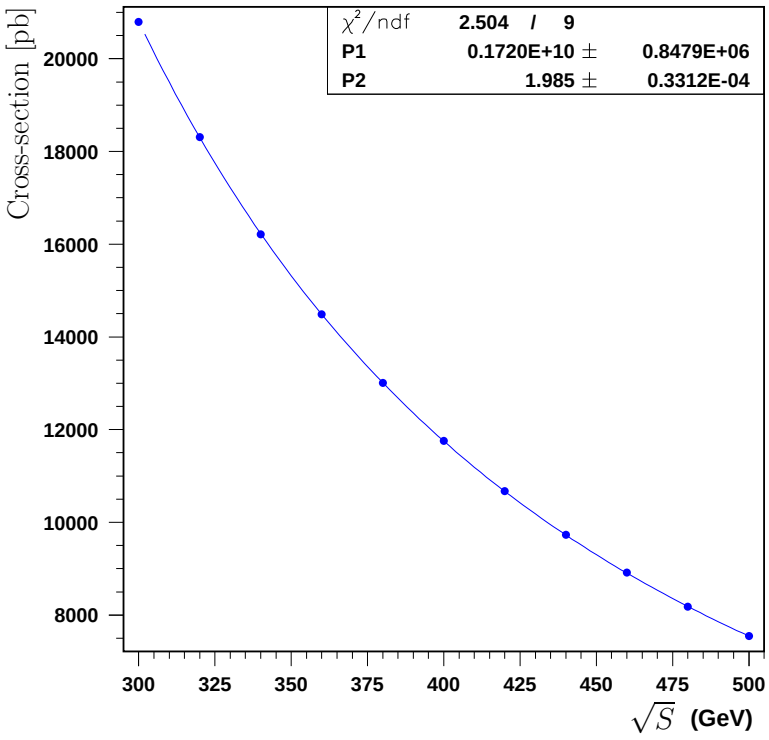

Figure 6.9: Differential Bhabha cross-section as a function of the centre of mass energy for angle between 23 and 85 mrad, the region relevant for the study, taking into account electroweak tree-level processes, interferences and radiative corrections as computed with the Bhabha generator (Bhwide 1.04).

angular distribution, below 4 mrad, and should not reach the detector.

- Positron-electron pairs created in the beam-beam interactions can produce significant background. These pairs are produced via two different types of scenario:

  - Incoherent pair creation where two colliding photons from beamstrahlung produce real electron-positron pairs. Three incoherent processes can be distinguished depending on the virtuality of the photons. The first one is the Breit-Wheeler process $\gamma\gamma \rightarrow e^+e^-$ where both photons are real, the second one is Bethe-Heitler process $e\gamma \rightarrow ee^+e^-$ with one real and one virtual photon, and finally the Landau-Lifshitz process $ee \rightarrow eee^+e^-$. The corresponding Feynman diagrams are displayed in Fig. 6.10

  - Coherent pair creation, where the photon converts into an electron-positron

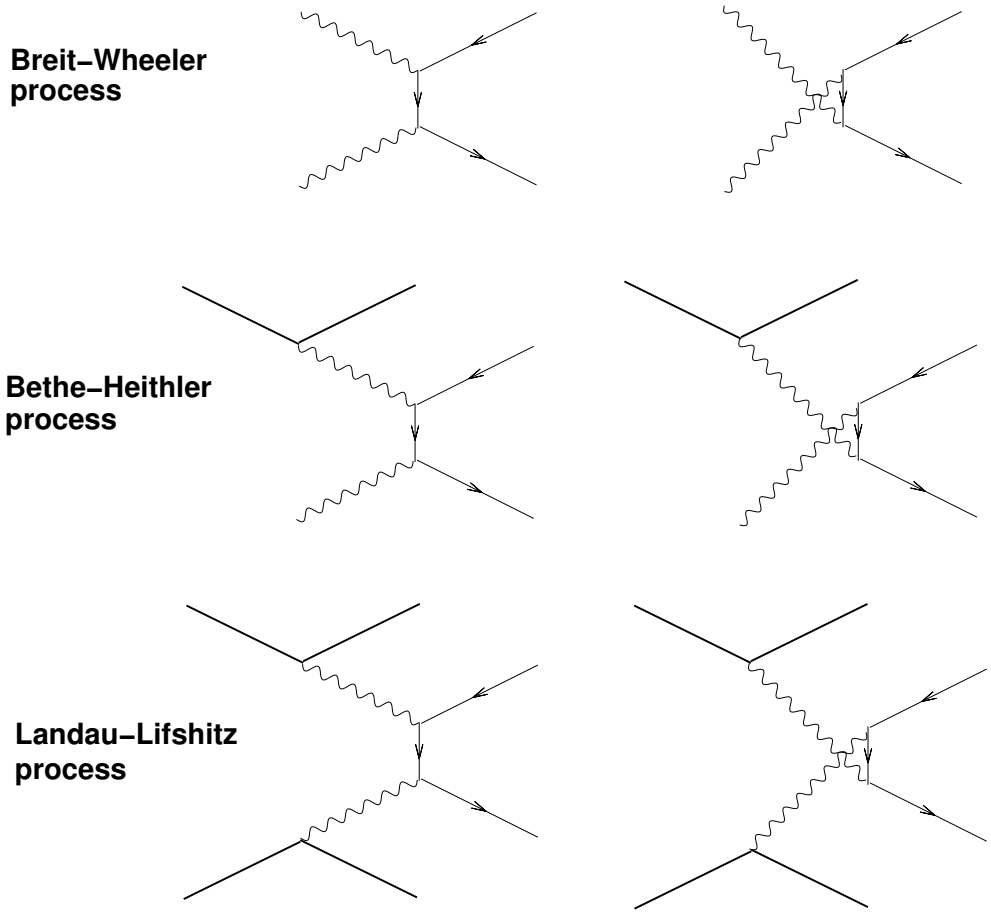

Figure 6.10: The incoherent pair production processes leading to possible background to Bhabha events.

pair. In a strong field, such as the one present within the LC detector, the pair spirals. It has been shown that the effect of the coherent pair creation is negligible [10] in the luminosity calorimeter.

For the physics processes mainly two are foreseen:

- $\gamma\ \gamma$ processes: Both the electron and positron beams can radiate photons with a low transverse momentum. The interaction of the two photons can create fermion pairs, as shown in the Feynman diagram 6.11, similar to the Bhabha process if the fermions are an electron and a positron. As the photons are emitted with a small angle with respect to the beam line and with a probability proportional to the inverse of its energy [21], the electrons and positrons are weakly deviated from their initial direction.

Thus the initial electrons and positrons escape into the beam line while the fermions deposit energy in the detectors.

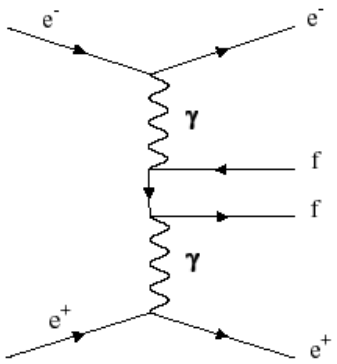

Figure 6.11: Feynman diagram associated with the $\gamma\gamma$ process.

- WW processes: WW processes can lead to a similar signal as Bhabha processes, where one W can decay into an electron and an anti-neutrino and the other W to a positron and an associated neutrino. Although the energy of the electron and positron can range from 0 to 250 GeV, the cross-section of the process is of the order a few tens of pb for $|\cos\theta| < 0.8$ [22] much smaller than the 7 nb for the Bhabha processes in the angular region from 23 to 85 mrad.

6.5 Interfacing the Beamstrahlung and Bhabha Generator

According to the respective fraction x_e^+, x_e^- of the nominal energy of each lepton, as given by the Beamstrahlung generator (CIRCE), the centre of mass can be calculated according to $\sqrt{x_{e^+}x_{e^-}} \times \sqrt{s_0}$. A Von Neumann's acceptance-rejection technique [12] can then be applied by considering, a probability density function (pdf) of the differential Bhabha cross-section distribution as shown in Fig. 6.9, and a uniformly distributed random number. The cross-section of each event with beamstrahlung is computed according to the pdf such that the minimum centre of mass energy, obtained including beamstrahlung only, corresponds to an

event with weight 1, i.e. an event which is accepted, and all other events with higher centre of mass are reweighted according to the distribution as in Fig. 6.9. For $\sqrt{s_0} = 500$ GeV, the lower limit of the centre of mass energy at which all events are accepted is $0.59 \times 500 = 295$ GeV for the considered statistics. Within Bhwide, the final state of the scattered particles, electrons, positrons and photons, is scaled with respect to $\sqrt{x_{e^+} x_{e^-}}$ and then boosted by Lorentz transformation. Finally, each created event undergoes a simple gaussian smearing in accordance with the addition in quadrature of the beam energy spread of the electron and positron as discussed in Sec.6.2.1. Fig.6.12 shows the final energy distribution with all the contributions included.

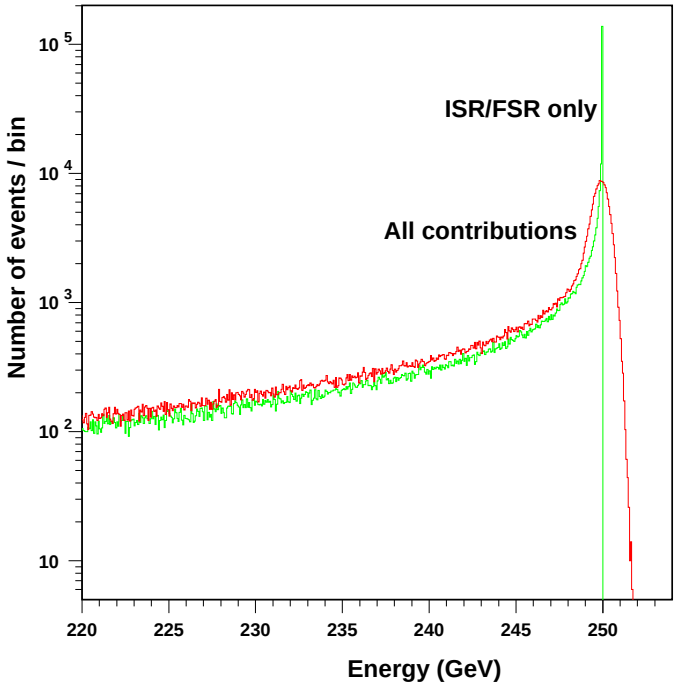

Figure 6.12: True energy distribution of one of the leptons including ISR and radiative corrections from Bhwide, beamstrahlung and a beam energy spread of 0.18%. For comparison the energy distribution with the Bhwide events only is displayed as well.

6.6 Determination of Luminosity Spectrum Parameters

A method was derived to estimate the beamstrahlung and relative energy spread from the measurements of the energy distribution of the electron[3]. In practice this meant recovering the parameters that were used to generate the beamstrahlung in CIRCE.

Assuming that the changes in the luminosity spectrum are linear for small changes of the beamstrahlung parameters around their initial values, the derivatives for a specific parameter can be calculated according to a lattice of values using the symmetrised form of the derivative calculation,

$$\frac{\partial f_{a_k}(j)}{\partial a_k} = \frac{f_{a_k+\delta a_k}(j) - f_{a_k-\delta a_k}(j)}{2\delta a_k} \tag{6.12}$$

where $f(j)$ is number of events in the bin j, a_k is the parameter which is considered and δa_k the shift applied to the parameter. Thus a lattice of seven simulated distributions is obtained, one with initial parameters and six with a_0, a_2 and a_3 varied by δa_k . A δa_k of 10% was chosen for each parameter and, before their use, a smoothing of the distributions based on the CERN library quadratic fit package HQUAD [15] was performed to reduce statistical fluctuations in the derivative calculation.

The simulated data were then fit by minimising the χ^2 function

$$\chi^2(a_0, a_2, a_3) = \sum_{j=1}^{N} \left(\frac{N^{(j)}_{\text{data}} - N^{(j)}_{\text{est}}(a_0, a_2, a_3)}{\sqrt{N^{(j)}_{\text{data}}}} \right)^2 \tag{6.13}$$

with

$$N^{(j)}_{\text{est}}(a_0, a_2, a_3) = N^{(j)}_{MC_{\text{ini}}} + \sum_i \left((a^{\text{est}}_k - a^{\text{ini}}_k) \times \frac{\partial f_{a_k}(j)}{\partial a_k} \right) \tag{6.14}$$

where $N^{(j)}_{MC_{ini}}$ refers to the number of events in the bin j for the initial parameter values, $N^{(j)}_{est}(a_0, a_2, a_3)$ are the estimated number of events for the same bin and $N^{(j)}_{\text{data}}$ correspond to the data spectrum. This minimisation leads to the estimation

[3]The energy of the positron could also be measured either to improve the statistical power of the present analysis, or to explore electron/positron energy correlations.

σ_{500} $[nb]$	Luminosity $[cm^{-2}s^{-1}]$	Nb of events / sec	Nb of MC events	MC luminosity $[nb]^{-1}$	Run time at 500 GeV [hours]
7.44±0.01	3.4 10^{34}	252.9	2 10^6	268.8 10^3	2.2

Table 6.3: Cross-section as computed from Bhwide for a Monte-Carlo (MC) generation between the angles of 23 and 85 mrad. 2 10^6 events correspond gives a MC luminosity ($L_M C$) of roughly 0.27 fb^{-1}.

of the beamstrahlung parameters as defined in CIRCE. With the same method a fourth parameter, the beam energy spread $\frac{\delta_E}{E}$, can be estimated. This method is now applied to five samples, each with 2×10^6 Bhabha events, corresponding to a integrated Monte-Carlo luminosity L_{MC} of 0.27 fb^{-1}, as detailed in Tab. 6.3. The five samples are used to investigate possible bias when applying the parameter estimation on the true, measured and unfolded spectra. They differ only by the seed of the random generator; the beamstrahlung parameters are the initial values as given in Tab. 6.2 and the relative beam energy spread $\frac{\delta_E}{E}$ is fixed at 0.18%. Thus only statistical fluctuations differentiate these samples. In addition, the number of bins for each spectrum is fixed at 300, ranging from 0 to 270 GeV, giving an equidistant bin width of 0.9 GeV. A study of the effects of the bin width on the result applied to the simulated measured data should be carried on. This would allow to verify if the technique is sensitive to the fitted parameter and not too dependent on random smearing over several bins of the energy collected in the detector. This could be performed with non-equidistant bin width, the size of the detector resolution (e.g. 4 GeV at E_{beam}=250 GeV).

6.6.1 Results for the True Spectrum

The parameter fit is performed for the true spectrum between 200 GeV and 254 GeV to take into account events which are smeared due to the beam energy spread and which can therefore can gain energies higher than 250 GeV. The low limit is fixed at 200 GeV because only the highest part of the spectrum is

significantly affected by the variation of the beamstrahlung. The fit method given by Equ.6.13 is applied to each sample. $N^{(j)}_{\rm data}$ is here the number of events for the true spectrum in the bin j. It will be referred as $N^{(j)}_{\rm true}$ in Sec. 6.7. A typical value for the reduced χ^2_r is 0.95, defined by χ^2/n_{dof}. Here, n_{dof} is the number of degrees of freedom and corresponds to the number of bins used for the fit (120 bins) minus the number of free parameters which is four, thus $n_{dof} = 116$. Being close to unity, the reduced χ^2_r indicates the fitting function is appropriate. For each sample, the errors in the estimated parameters are first calculated from the values for which the χ^2 increases by 1 (MINUIT [16]) and are thus the one standard deviation error.

Furthermore the standard deviation $\bar{\sigma}_{k,\rm std}$ of the mean of the samples is performed with

$$\bar{\sigma}^2_{k,\rm std} = \frac{1}{N_s - 1} \sum_{l=1}^{N_s} (a^{\rm est}_{k,l} - \bar{a}^{\rm est}_k)^2 \tag{6.15}$$

where $N_s = 5$ is the number of samples, k is the parameter number as given in Tab. 6.4, $a^{\rm est}_{k,l}$ the estimated parameter for the sample $l = [1, 5]$ and $\bar{a}^{\rm est}_k$ is the mean of the estimated parameter for the five samples. The individual MINUIT fit errors were found to be within 1 standard deviation of $\bar{\sigma}_{k,\rm std}$ and thus only the mean and $\bar{\sigma}_{k,\rm std}$ are given in Tab 6.4. In addition the mean pull $\bar{P}_i$ is given for each parameter. It is defined as

$$\bar{P}_k = \frac{1}{N_s} \sum_{l=1}^{N_s} P_{k,l} = \frac{1}{N_s} \sum_{l=1}^{N_s} \frac{a^{\rm est}_{k,l} - a^{\rm ini}_k}{\sigma_{k,l}} \tag{6.16}$$

where $P_{k,l}$ is the pull calculated with the error $\sigma_{k,l}$ on the fit for the considered parameter for each sample and $a^{\rm ini}_k$ is the initial value. Hence, the pull corresponds to a gaussian centred on zero with a width consistent with unity. The pull values obtained for the beamstrahlung and beam energy spread parameters are found to be $\leq \mathcal{O}(1)$. Thus, applied to the true spectrum, the fit method leads to a good estimation of the parameters. Nonetheless, in the "real world", direct access to the true spectrum is impossible. It is necessary instead to apply the method to the measured spectrum as discussed in the following section.

Par. k	initial $a_k^{\rm ini}$	estimated mean $\bar{a}_k^{\rm est}$	estimated mean error $\bar{\sigma}_{k,\rm std}$	pull $\bar{P}_k$	pull width $\sigma_{\bar{P}_k}$
a_0	0.51288	0.5133	0.0012	0.27	0.35
a_2	9.9716	10.000	0.033	0.51	0.28
a_3	-0.6285	-0.626	0.0015	-0.81	0.33
$\frac{\delta_E}{E}$	1.8 10^{-3}	1.801 10^{-3}	9.96 10^{-7}	0.44	0.16

Table 6.4: Mean beamstrahlung parameters and mean relative beam energy spread estimation using the fit method, with four free parameters, on true spectra at $\sqrt{s}$ = 500 GeV. Five independent samples with L_{MC}=0.27 fb^{-1} were used to obtain the mean $\sigma_{\bar{k},\rm std}$. The pull is defined in Eq. 6.16.

6.6.2 Energy Measurements

Measurements of the energy of the final state - containing electrons, positrons and photons - is performed at low angles with the forward calorimeters. In the following, only the LumiCal is used, although the study could be extended to include the detectors at upper angles.

The geometrical acceptance of LumiCal is limited to between 26 and 82 mrad as discussed in Sec. 3.2.3.3. The events from Bhwide are generated between 23 and 85 mrad in order to encompass most of the events, which are then boosted within the detector region, because a particle with angular momentum originally at 23 mrad can, with the boost, reach the detector at 26 mrad. As shown in Fig. 6.13, the final angle of the lepton can be, with the boost, larger than the specified angle in Bhwide. Computation with the Bhabha generator Bhwide gave a cross-section of 186777 pb for events originally generated between 15 and 85 mrad and 140.16 pb for events between 85 and 100 mrad. Respectively 1.05% and 0.125% of the events are counted inside the detector range. Applying an angle cut at the generator level of 23$< \theta <$85 mrad leads to approximately 1.3% of the total number of events being missed but this reduced greatly the time spent on the generation of each distribution.

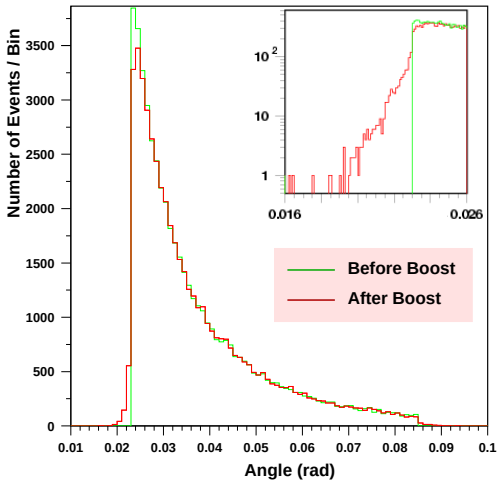

Figure 6.13: Angular distribution of the electron before and after the boost when the nominal generator angular cut is fixed between 23 and 85 mrad. A close-up view of the distribution using a log-scale for the angular region below 26 mrad is also displayed.

6.6.3 Effect of the Luminosity Detector Resolution and Reconstruction

A luminosity calorimeter, such as the one described in Chap. 3, will smear the energy deposit as displayed in Fig. 6.14. The response matrix of the detector for the considered observable, i.e. the true electron energy, versus the measured energy is given is Fig. 6.15 for a luminosity calorimeter type detector with energy resolution $25\%/\sqrt{E}$. Photons and electrons are not differentiated by the calorimeter because no charge tracker is available in the forward calorimetry; both have to be taken into account. Due to the finite resolution of the LumiCal, photons and electrons very close together can appear as being only one particle. To account for this effect a simple cluster finding code was written. The highest energetic particle which contributes to a cluster defines a central axis around which any particle within a distance of one Molière radius is merged. As seen in chapter 3, the luminosity calorimeter is foreseen to be made of silicon tungsten thus the distance is set to 9 mm, i.e. one Molière radius. It was checked that a modification of the minimum distance for the cluster by 1 mm does not change the result by more than a few events out of 500 000 events (0.01%). The spectra

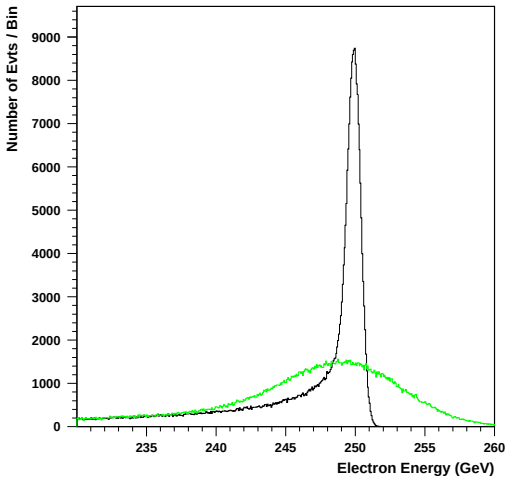

Figure 6.14: True and measured electron energy distribution by a typical calorimeter with energy resolution $25\%/\sqrt{E}$.

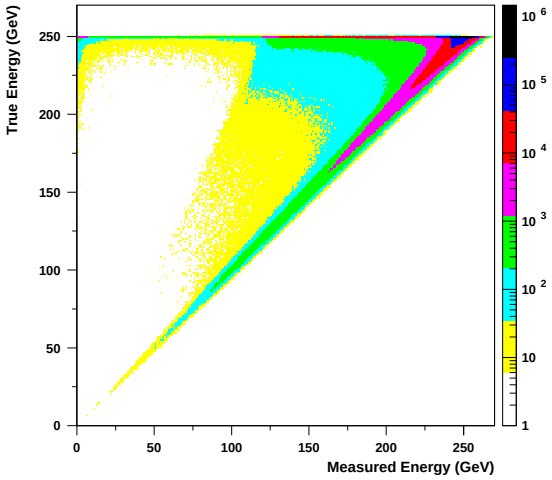

Figure 6.15: Response matrix for a LumiCal type calorimeter with energy resolution $25\%/\sqrt{E}$ performed with 48 10^6 events.

of Fig. 6.16 show the result of the clustering as well as the electron and photon energy distribution. The result of the event selection is shown in Fig. 6.17.

6.6.4 Results for Measured Distribution

In the following the measured spectrum is defined as the distribution after both the detector smearing and the clustering algorithm have been applied. To ac-

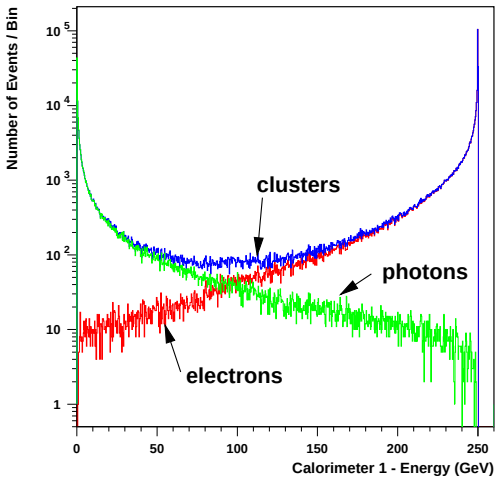

Figure 6.16: Simulated electron and photon energy distribution before and after the cluster finding.

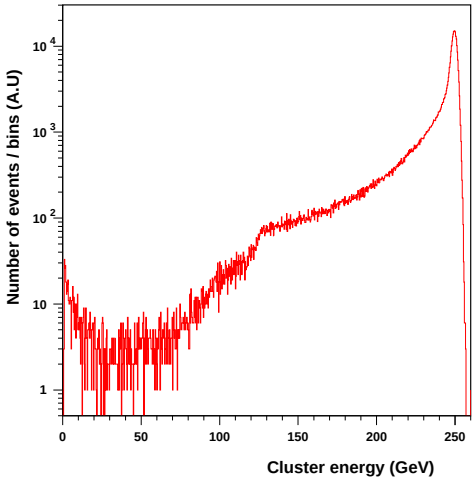

Figure 6.17: The spectrum in one calorimeter after including the detector angular acceptance and simple clustering algorithm.

cept the event at least one cluster has to be measured in both forward and rear detectors. A similar method to the one presented above is used to estimate the considered parameters on the measured distribution. $N^{(j)}_{\rm data}$ is here the number of events for the measured spectrum in the bin j. It will be referred as $N^{(j)}_{\rm meas}$ in Sec. 6.7. The typical reduced χ^2_r, as calculated in Sec. 6.6.1, is approximately 1.02 on each sample. For several parameters the pull is higher than unity and bigger than the pull obtained for the estimations on the true spectrum. A differ-

Par. k	initial a_k^{ini}	estimated mean $\bar{a}_k^{\text{est}}$	estimated mean error $\bar{\sigma}_{k,\text{std}}$	pull $\bar{P}_k$	pull width $\sigma_{\bar{P}_k}$
a_0	0.51288	0.5092	0.0015	0.86	0.30
a_2	9.9716	9.967	0.048	-0.05	0.52
a_3	-0.6285	-0.631	0.0018	0.52	0.38
$\frac{\delta_E}{E}$	$1.8\ 10^{-3}$	$1.84\ 10^{-3}$	$2.7\ 10^{-5}$	1.84	1.18

Table 6.5: Beamstrahlung parameters and relative beam energy spread estimation using a fit method with four free parameters on measured spectra at $\sqrt{s} = 500$ GeV and L_{MC}=0.27 fb^{-1} as given in Tab. 6.3.

ent method has to be investigated. In the following section an advanced method based on unfolding is used to estimate the beamstrahlung and beam energy spread parameters.

6.7 Unfolding Technique

6.7.1 General Strategy

In order to estimate the true luminosity distribution, an unfolding technique is used based on the Tikhonov method which employs a regularisation function. This technique is presented briefly here and in more detail in [20],[18] and [19].

Assume that the expectation values of the measured number of entries $\nu_i = E[N^{(i)}_{\text{meas}}]$ in the bin i can be described with the relation

$$\nu_i = \sum_{j=1}^{nx} R_{ij}\mu_j \tag{6.17}$$

where R_{ij} is the response matrix of a detector as given in Fig. 6.15, $\mu = E[N^{(j)}_{\text{true}}]$ is the expectation values in bin j of the true distribution of a signal and nx is the number of bins. Inverting Eq. 6.17 as $\vec{\nu} = R^{-1}\vec{\mu}$ in vector notation, to get the unknown true distribution does not always work because $\vec{\nu}$ is not accessible and only the data $N^{(i)}_{\text{meas}}$ are measured which contain statistical fluctuations. This

inversion leads to an estimation of the original distribution, $\vec{\hat{\mu}}$, with large variance and oscillations.

The general strategy used to avoid these oscillations is to introduce a parameter which smooths the $\vec{\hat{\mu}}$ distribution. $\vec{\hat{\mu}}$ is characterised by the least-square function $L(\vec{\hat{\mu}})$ while the smoothness of the distribution can be represented by $S(\vec{\hat{\mu}})$, called the regularisation function. In the Tikhonov method that is presently used, $S(\vec{\hat{\mu}})$ is a derivative of the unknown true distribution to the second order.

Thus, a combination of the least-square function and the regularisation function with a weight τ smooths the distribution and hence leads to a less oscillating solution. The combination can be written as

$$\phi(\vec{\hat{\mu}}) = L(\vec{\hat{\mu}}) + \tau S(\vec{\hat{\mu}}) \tag{6.18}$$

where τ is the regularisation parameter. In practice, if τ is small, the solution is highly oscillating and if τ is large the solution for the estimated unfolded distribution is smooth.

6.7.2 Unfolding in More Detail

The unfolding program (GURU [19]) used here is based on the Tikhonov method with a regularisation function. In the following, the expectation value of the unknown vector $\vec{\hat{\mu}}$ is called $N^{(j)}_{\text{unk}}$ and refers to the expectation value of the number of entries in the bin j. Instead of using Eq. 6.18, which is applied directly to the spectra, a transformation of this equation is performed within the unfolding program such that it includes a weight $w^{(j)}_{\text{unk}}$ defined as

$$w^{(j)}_{\text{unk}} = \frac{N^{(j)}_{\text{unk}}}{N^{(j)}_{\text{ref}}} \tag{6.19}$$

where $N^{(j)}_{\text{ref}}$ is a reference Monte Carlo distribution and $N^{(j)}_{\text{unk}}$ is the unknown spectrum that has been unfolded. $w^{(j)}_{\text{unk}}$ is a measure of the deviation of $N^{(j)}_{\text{unk}}$ from an initial Monte Carlo input vector $N^{(j)}_{\text{ref}}$. Thus Eq. 6.18 becomes

$$\sum_{j=1}^{nx} \tilde{R}_{ij} w^{(j)}_{\text{unk}} = \tilde{N}^{(j)}_{\text{meas}} \tag{6.20}$$

where $\tilde{R}$ and $\tilde{N}_{\text{meas}}$ are respectively the rescaled matrix and measured data as given by GURU. Introducing a weight has the advantage that if the MC spectrum $N_{\text{ref}}^{(j)}$ is close to the unknown spectrum $N_{\text{unk}}^{(j)}$ then the unknown weight $w_{\text{unk}}^{(j)}$ will be smooth and have a small bin-to-bin variations. The accuracy of the unfolding is thereby increased as fewer unknowns are required to decompose the orthogonal functions of the singular value decomposition (SVD) approach used in the unfolding code.

A solution to Eq. 6.20 with low oscillation can be obtained by adding a regularisation term. The expression can thus be written as the addition of a general form of the least-square function and the regularisation function

$$\phi(\vec{w}, \tau) = (\tilde{R}\vec{w} - \tilde{N}_{\text{meas}})^T(\tilde{R}\vec{w} - \tilde{N}_{\text{meas}}) + \tau(C\vec{w})^T C\vec{w} \tag{6.21}$$

where $\tilde{R}$ is the response matrix of the detector, $\tilde{N}_{\text{meas}}$ the measured data, w the unknown initial vector (same as $w_{\text{unk}}^{(j)}$) and C is a matrix which defines the *a priori* condition on the solution. Here, C is a "second derivative matrix". It includes a small term $\epsilon = 10^{-4}$ added to the diagonal elements of the matrix such that its inversion[4] within the SVD approach is possible and does not modify the condition of minimum curvature implied by the derivative.

6.7.3 Finding a Suitable Smoothing Parameter

The solution w, the unknown vector, of Eq. 6.21 is dependent on the choice of τ and a careful study has to be performed which is described in the following section. Here, $N_{\text{unk}}^{(j)}$, the expectation value of the number of events in bin j, is used instead of w as it is a direct representation of the energy spectrum.

The strategy that is employed here is to fix the smoothing parameter for each of the 5 samples of measured spectra on which the unfolding is applied. To find the best τ to reconstruct the data attention is first concentrated on one of the

[4]The SVD-GURU approach uses the inversion $\tilde{R}C^{-1}$ to solve Eq. 6.21.

sample and a minimisation of the χ^2_u is performed

$$\chi^2_u = \sum_{j=1,nx} \left(\frac{N^{(j)}_{\text{true}} - N^{(j)}_{\text{unk}}}{\sqrt{N^{(j)}_{\text{true}}}} \right)^2 \tag{6.22}$$

where $N^{(j)}_{true}$ is the number of events in bin j for the true spectrum, $N^{(j)}_{unk}$ is the expectation value of the number of events in bin j for the unfolded spectrum. The χ^2_u as a function of τ is displayed in Fig. 6.18 with τ values ranging from 10^5 to 10^8. The shape of the curve of χ^2_u, can be explained by the fact that at high τ the unfolding spectrum is very flat and the unfolded spectrum is far from the true distribution thus increasing χ^2_u while at low τ the unfolding spectrum contains oscillations. The minimisation of χ^2_u applied to one reference sample leads to

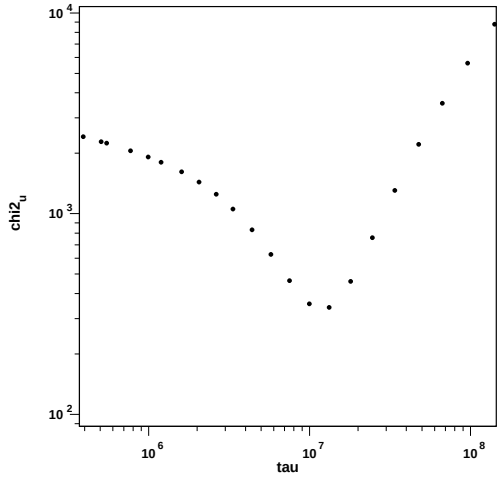

Figure 6.18: χ^2_u versus the smoothing parameter τ. A minimum value of $\chi^2_u = 340.$ is obtained for $\tau = 1.3\ 10^7$.

the choice of the smoothing parameter to be $\tau = 1.3\ 10^7$. The corresponding unfolded electron energy spectrum is given in Fig. 6.19 for the highest part of the spectrum. The energy spectrum from unfolding matches the true spectrum within the statistical fluctuations. These fluctuations do not appear anymore in the unfolded spectrum as the method naturally smooths the entire spectrum.

Instead of using the χ^2_u based on $\sqrt{N_{true}}$ one can think of using the covariance matrix X^{-1} as calculated by error propagation in GURU with

$$X^{-1}_{jk} = \frac{1}{N^{(j)}_{\text{ref}} N^{(i)}_{\text{ref}}} \sum_i \tilde{R}_{ij} \tilde{R}_{ik} \tag{6.23}$$

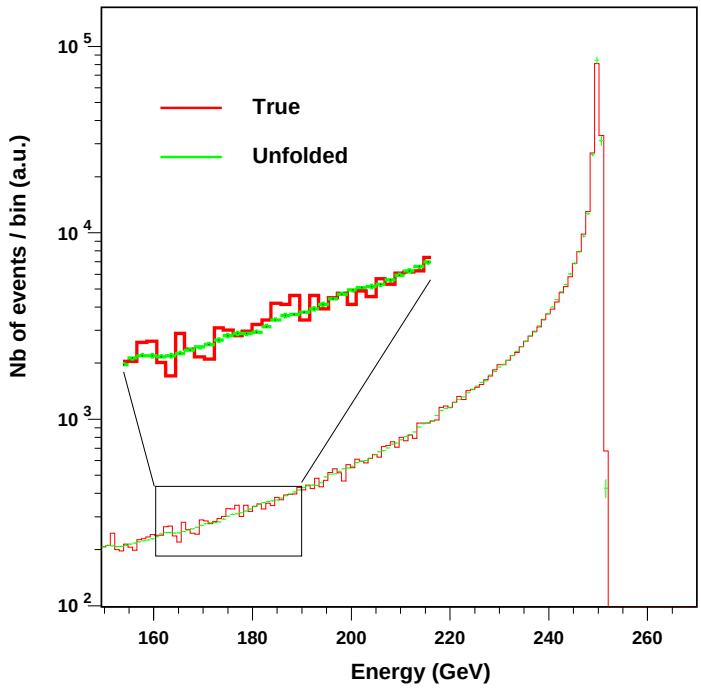

Figure 6.19: True and unfolded electron energy spectrum. The close-up view shows the fluctuations of the true spectrum and smoothness of the unfolded one.

thus the choice of τ depends on the minimization of

$$\chi^2_u = \sum_{j=1,nx} \left(\frac{N^{(j)}_{\text{true}} - N^{(j)}_{\text{unk}}}{\sigma^{(j)}_{\text{unk}}} \right)^2 \tag{6.24}$$

where $\sigma^{(j)}_{\text{unk}}$ is the error on the unfolded result for each bin and is equal to the diagonal element of the covariance matrix. This method gives, for the same sample as above, a suitable $\tau = 0.334 \times 10^7$; much smaller than the previous value.

To help decide which τ to choose, a study of the results of the fitting with respect to the smoothing parameter is now performed. The unfolding technique is applied to a set of five samples of the "measured" spectrum. Fig.6.20 shows each of the estimated parameters a_k and δ_{BS} as a function of τ. The dots of the plots correspond to the fit results for each sample with errors given by MINUIT. The contour lines show the standard deviation on the mean over the samples as calculated in Sec. 6.6.1. For the range of τ parameters used, from 2.6×10^6 to 1.4×10^8, the fit parameters are all consistent with the initial ones. In addition

the standard deviation on the mean decreases as τ increases. However the fit parameters calculated from each sample differ by more than a standard deviation when τ is small (around 3×10^6) and the discrepances diminish as τ is increased. It indicates that the unfolding is stable over a wide range of τ. It shows as well that the errors are getting smaller as the smoothing parameter increases. For the

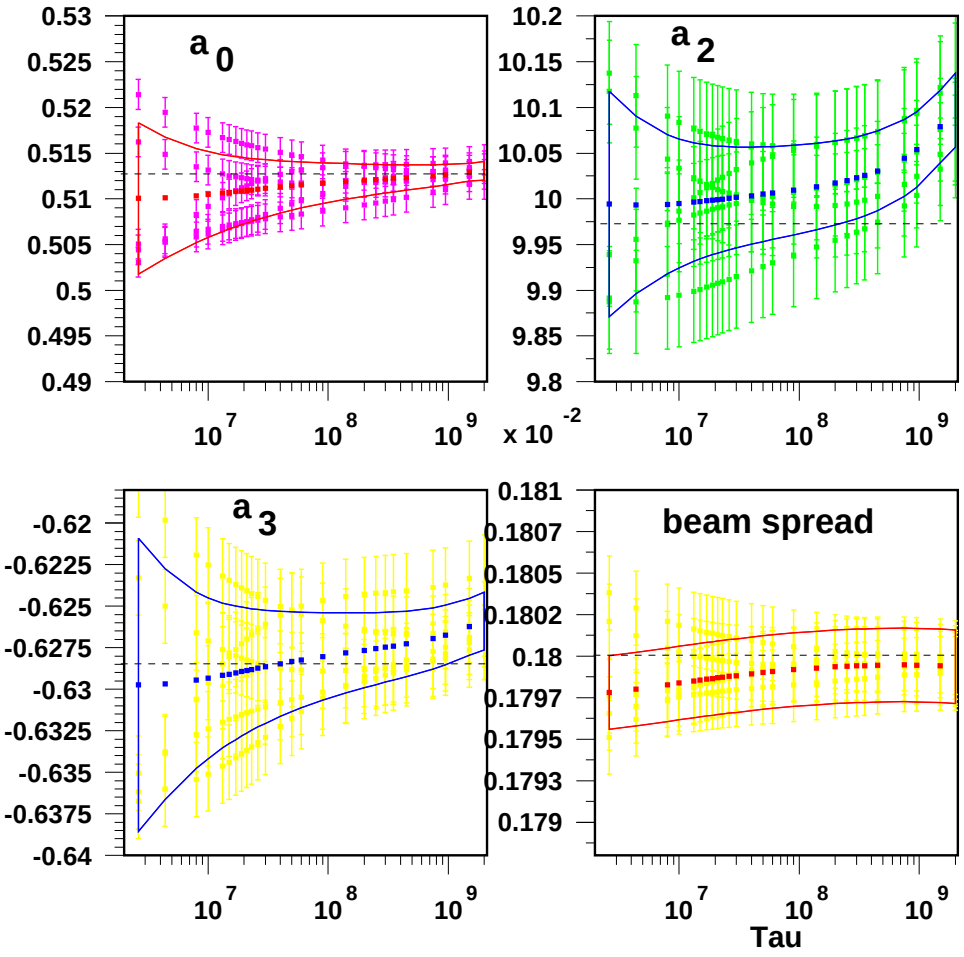

Figure 6.20: Result of the parameters estimation method on the unfolded spectrum as a function of the smoothing parameter τ. Dots correspond to the estimated value for each sample. The solid lines are the standard deviation boundary of the means and the dashed lines are the initial parameters

following unfolding study $\tau = 6 \times 10^7$ is chosen as this value leads to estimated parameters which are in a stable region. Furthermore the initial parameters are within one standard deviation of the mean of the estimated parameters.

Par. k	initial a_k^{ini}	estimated mean $\bar{a}_k^{\mathrm{est}}$	estimated mean error $\bar{\sigma}_{k,\mathrm{std}}$	pull $\bar{P}_k$	pull width $\sigma_{\bar{P}_k}$
a_0	0.51288	0.51152	0.00252	-0.83	0.64
a_2	9.9716	10.0064	0.0508	0.61	0.58
a_3	-0.6285	-0.62823	0.00288	0.11	0.61
$\frac{\delta_E}{E}$	$1.8\ 10^{-3}$	$1.7994\ 10^{-3}$	$9.14\ 10^{-7}$	-0.27	0.41

Table 6.6: Mean beamstrahlung parameters and mean relative energy beam spread estimation using the fit method on unfolded spectra.

6.7.4 Parameters Estimation for Unfolding

The averages and standard deviations resulting from the fit of the five samples are given in Tab. 6.6 with the chosen τ. The pull is $\lesssim \mathcal{O}(1)$ for each estimated parameter. Thus the method, including the unfolding and parameter estimation as explained earlier, gives consistent results.

6.8 Summary

The parameter estimation is summarised in Fig. 6.21. Each graph corresponds to a defined parameter respectively a_0, a_2, a_3 and the relative beam energy spread. The estimates for each sample are given, as well as the averages and standard deviations resulting from these samples as given in the previous sections for the true, "measured" and unfolded spectra. As discussed earlier, the initial parameters are found to be within the errors of the estimated parameters for the true spectrum. This was not the case for the "measured" spectrum. To overcome this problem, unfolding was applied and the estimated values and errors are now consistent with the true ones.

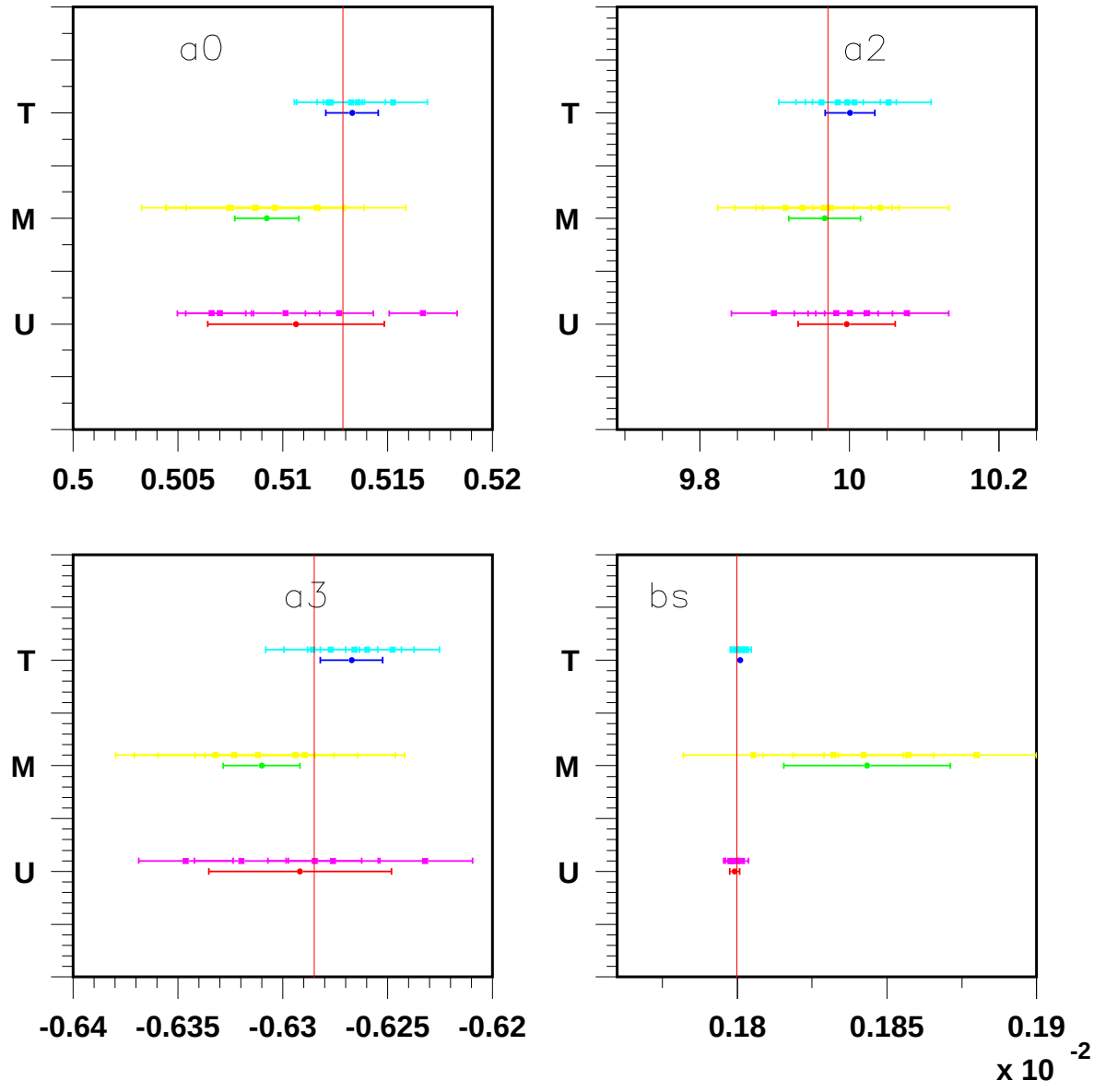

Figure 6.21: Parameter estimation for the true (T), the "measured" (M) and the unfolded spectrum (U) respectively for a_0, a_2, a_3 and relative beam energy spread. Five independent samples are shown together with the average and standard deviation resulting from these samples.

6.9 Conclusion

In this chapter, the luminosity measurement using a large cross-section physics process was presented. A method to estimate beamstrahlung parameters was devised and implemented. It was shown that this method can be used to deter-

Par.	True	Meas.	Unf
a_0	0.24%	0.3%	0.49%
a_2	0.34%	0.48%	0.51%
a_3	0.29%	0.24%	0.46%
$\frac{\delta_E}{E}$	0.055%	1.5%	0.051%

Table 6.7: Relative errors on the luminosity and energy beam spread parameters using the determination method applied to the true, measured and unfolded spectrum, each with 300 bins, and $L_{MC} = 0.27 fb^{-1}$.

mined the true parameters. The same strategy was applied to the "measured" spectrum, performed with a typical luminosity calorimeter. In order to improve the results, an unfolding technique employing a regularisation function and applied to the measured spectrum was carried out. Applying this new method to the unfolded spectrum, an estimate of the beamstrahlung and gaussian relative beam energy spread parameters was achieved. The relative error of the beam energy spread from the unfolded spectrum is consistent with the one obtained for the true spectrum.

The results presented in this chapter reveal that this method could be used to determine the luminosity spectrum on an hourly basis to a precision of less than a percent.

Bibliography

[1] H. J. Bhabha, "The Creation Of Electron Pairs By Fast Charged Particles," Proc. Roy. Soc. Lond. A **152** (1935) 559.

[2] G. Montagna, O. Nicrosini and F. Piccinini, "Precision physics at LEP," Riv. Nuovo Cim. **21N9** (1998) 1 [arXiv:hep-ph/9802302].

[3] K. L. Bane and M. Sands, "Wake Fields Of Very Short Bunches In An Accelerating Cavity," Part. Accel. **25** (1990) 73.

[4] A. Pukhov *et al.*, "CompHEP: A package for evaluation of Feynman diagrams and integration over multi-particle phase space. User's manual for version 33," arXiv:hep-ph/9908288. `http://www.ifh.de/~pukhov/comphep.html`

[5] S. Jadach, W. Placzek and B. F. L. Ward, "BHWIDE 1.00: O(alpha) YFS exponentiated Monte Carlo for Bhabha scattering at wide angles for LEP1/SLC and LEP2," Phys. Lett. B **390** (1997) 298 [arXiv:hep-ph/9608412].

[6] "International Linear Collider Technical Review Committee. Second report, 2003," SLAC-R-606

[7] D. R. Yennie, S. C. Frautschi and H. Suura, "The Infrared Divergence Phenomena And High-Energy Processes," Annals Phys. **13** (1961) 379.

[8] T. Barklow, "Energy Spread and Energy Precision: Comparison of NLC and TESLA" LCWS 2004, Paris

[9] D. Schulte, "Beam-Beam Simulations With Guinea-Pig," CERN-PS-99-014-LP

[10] D. Schulte, "Study of electromagnetic and hadronic background in the interaction region of the TESLA Collider," DESY-TESLA-97-08

[11] T. Ohl, "CIRCE version 1.0: Beam spectra for simulating linear collider physics," Comput. Phys. Commun. **101** (1997) 269 [arXiv:hep-ph/9607454].

[12] J. von Neumann, "Various techniques used in connection with random digits," J. Res. NBS Appl. Math. Ser **12** (1951) 36

[13] A. W. Chao and M. Tigner, "Handbook Of Accelerator Physics And Engineering", Singapore, Singapore, World Scientific (2002) 654 p.

[14] K. Yokoya and P. Chen, "Beam-beam phenomena in linear colliders," KEK-PREPRINT-91-2

[15] J. Allison. "Multiquadratic Radial Basis Functions for Representing Multidimensional High Energy," Physics Data. Comp. Phys. Comm., 77:377-395, 1993.

[16] F. James and M. Roos, "'Minuit' A System For Function Minimization And Analysis Of The Parameter Errors And Correlations," Comput. Phys. Commun. **10** (1975) 343.

[17] R. Brinkmann, K. Flottmann, J. Rossbach, P. Schmuser, N. Walker and H. Weise, "TESLA: The superconducting electron positron linear collider with an integrated X-ray laser laboratory. Technical design report. Pt. 2: The accelerator," DESY-01-011

[18] V. Blobel, "An unfolding method for high energy physics experiments," arXiv:hep-ex/0208022.

[19] A. Hocker and V. Kartvelishvili, "SVD Approach to Data Unfolding," Nucl. Instrum. Meth. A **372** (1996) 469

[20] G. Cowan, "Statistical Data Analysis," Oxford, UK, Clarendon (1998) 197 p `http://www.slac.stanford.edu/spires/find/hep/www?irn=3988171`

[21] F. A. Berends, R. Kleiss and W. Hollik, "Radiative Corrections To Bhabha Scattering At High-Energies. 2: Hard Photon Corrections And Monte Carlo Treatment," Nucl. Phys. B **304** (1988) 712.

[22] J. A. Aguilar-Saavedra *et al.* [ECFA/DESY LC Physics Working Group Collaboration], "TESLA Technical Design Report Part III: Physics at an e+e- Linear Collider," arXiv:hep-ph/0106315.

List of Figures

List of Tables